

INSTITUTE OF BIOORGANIC CHEMISTRY
POLISH ACADEMY OF SCIENCES IN POZNAN, POLAND

Aleksandra Jarmołowicz

Small molecules interacting with Influenza virus RNA and SARS-CoV-2 RNA as potential inhibitors of replication

The doctoral thesis has been completed
in the Department of RNA Structural Genomics

Promotor:

Prof. dr hab. Elżbieta Kierzek

POZNAŃ, 2022



The doctoral dissertation was conducted as part of participation in the project Interdisciplinary Doctoral Studies "NanoBioTech", carried out jointly by three units:

- Poznan University of Technology,
- Poznan University of Medical Sciences,
- Institute of Bioorganic Chemistry, Polish Academy of Sciences,

Under the POWR.03.02.00-00-I011/16 grant agreement.

The project Interdisciplinary Doctoral Studies "NanoBioTech" is co-financed by the European Union from the European Social Fund under the Operational Program Knowledge Education Development 2014 – 2020.



*I would like to thank
Professor Elżbieta Kierzek
for the supervisor's care, understanding,
valuable advice and help.*

*To all collaborators from
the RNA Structural Genomics Group,
I would like to express my sincere thanks
to all the people who contributed to this work.*

Contents

1. MAIN AIM	7
2.1. ABSTRACT	9
2.2. STRESZCZENIE	11
3. INTRODUCTION	14
3.1 Influenza A Virus (IAV)	14
3.1.1. Structure and replication of IAV	14
3.1. SARS-CoV-2	18
3.1.1. Structure and replication of SARS-CoV-2	18
3.2. Inhibitory strategies	22
3.2.1. Antisense Oligonucleotides	22
3.2.2. siRNA	26
3.2.3. PNA	29
3.2.4. Small molecules	31
4. RESULTS AND DISCUSSION	36
4.1. Selected RNA structural motifs	37
4.1.1. IAV RNA motifs	38
4.1.2. SARS-CoV-2 RNA motifs	40
4.2. Selection of SMs from Lopac and Enamine library	43
4.2.1. High Throughput Screening Assay Preparation	47
4.2.2. Lopac Library	50
4.2.3. Enamine Library	58
4.3. Characterization of the tertiary structure of selected RNA structural motifs generated in Molecular Dynamic Simulations.	67
4.4. The binding affinity of selected SMs	74

4.4.1.	Characterization of the binding with the selected Lopac SMs	74
4.4.2.	Characterization of the binding with the selected Enamine SM	83
4.5.	Small molecules as inhibitors of IAV replication	95
4.5.1.	Inhibitory potential of selected Lopac library compounds	95
4.5.2.	Inhibitory potential of selected Enamine library compounds	102
5.	SUMMARY	109
6.	MATERIALS AND METHODS	118
6.1.	MATERIALS	118
6.1.1.	Oligonucleotides	118
6.1.2.	Commercially available sets:	119
-	LOPAC® ¹²⁸⁰ library – purchased 12.16.2020 (LO1280, Sigma),	119
-	Enamine library – purchased 10.22.2020 (Enamine RNA-8960-Y-10 library).	119
6.1.3.	Commercially available sets:	119
6.1.4.	Antibodies:.....	119
6.1.5.	Fluorescent dyes:	119
6.1.6.	Buffers:	120
6.1.7.	Cell line:.....	120
6.1.8.	Influenza strain:	120
6.1.9.	Cell medium:	120
6.2.	Methods	122
6.2.1.	Oligonucleotides synthesis	122
6.2.2.	RNA deprotection	122
6.2.3.	RNA elution from polyacrylamide gels.....	122
6.2.4.	RNA precipitation.....	123

6.2.5.	RNA concentration measurement.....	123
6.2.6.	MDCK cell culture.....	123
6.2.7.	IAV infection	123
6.2.8.	Incubation with small molecules	124
6.2.9.	Immunofluorescence Focus Formation Assay (IFA).....	124
6.2.10.	Total RNA isolation	125
6.2.11.	DNA enzymatic degradation.....	125
6.2.12.	Reverse transcription	125
6.2.13.	Real-time qPCR with the reference gene	126
6.2.14.	Luminescent Cell Viability Assay.....	126
6.2.15.	Determination of EC ₅₀	126
6.2.16.	Determination of IC ₅₀	127
6.2.17.	High throughput screening (HTS).....	128
6.2.18.	Molecular dynamics	129
6.2.19.	Simulated RNA structure clustering	130
6.2.20.	Molecular docking	130
7.	LIST OF FIGURES AND TABLES	132
7.1.	Figures	132
7.2.	Tables	134
8.	BIBLIOGRAPHY	136

1. MAIN AIM

Influenza A virus (IAV) is responsible for a highly contagious respiratory illness called flu. It is dangerous due to high genetic variability, easy transmission, and serious epidemiological threats. According to the World Health Organization (WHO), seasonal flu is responsible for 290,000-650,000 deaths annually. The most dangerous are pandemics, which occur sporadically as new flu strains gain the ability to infect humans and spread globally. The latest known IAV pandemic was in 2009: the influenza A (H1N1) pandemic. The 2009 H1N1 virus possesses a unique combination of segments from human, swine, and avian influenza A viruses. The last pandemic caused by an RNA virus that is widely known and shook the world is Coronavirus disease 2019 (COVID-19), caused by the Severe Acute Respiratory Syndrome Coronavirus 2 (SARS-CoV-2) virus. This is another threatening respiratory virus that has appeared since 2020. COVID-19 is a global pandemic that was responsible for infections and deaths all over the world and has had a negative impact on people's physical and mental health. Until 23 December 2022, there have been 651 918 402 confirmed cases of COVID-19, including 6 656 601 deaths, reported to WHO.

Both IAV and SARS-CoV-2 are RNA viruses, and RNA is crucial in their replication cycle. The SARS-CoV-2 and the IAV replication cycles are fully dependent on RNA. The IAV genome consists of eight negative-stranded RNA (vRNA) segments, where the SARS-CoV-2 is the largest known RNA virus, consisting of a single-stranded, positive sense RNA genome. Previous studies show that the secondary structure of individual types of viral RNA is important for its function, ensuring the correct course of the replication cycle and efficient proliferation of the virus. RNA and its secondary structure is an excellent target for designing inhibitory strategies against both mentioned viruses. Particularly interesting are the structurally conserved secondary motifs that are preserved despite sequence variability. The secondary structure within the RNA of SARS-CoV-2 and the IAV has been intensively investigated, giving a strong basis for the development of RNA targeting therapeutic strategies.

The main aim of this work was to find small molecules (SMs) that could serve as inhibitors of the IAV and SARS-CoV-2 targeting viral RNA. The objects of the study were viral RNA (vRNA) structural motifs of the IAV and the SARS-CoV-2. The idea of research is that small molecules that could recognize certain binding packet within RNA structure by tight binding could disturb the function of RNA and, in the case of viral RNA, lead to inhibition of virus replication. Specifically, strong SM binding would work by blocking and preventing the RNA motif from important inter- and intramolecular interactions.

The particularized aims of the research were as follows:

- I. Finding small molecules that strongly bind to selected conserved structural motifs of the IAV RNA and SARS-CoV-2 RNA using high throughput screening (HTS).
- II. Application of molecular dynamics simulations (MDS) to predict and characterize 3D structures of selected vRNA motifs.
- III. Determination of the binding affinity and binding site in conserved vRNA structural motifs of the best small molecules using molecular docking (MD).
- IV. Evaluation of the antiviral potential of the selected small molecules against a strain of influenza A virus, A/California/04/2009 (H1N1), in the MDCK (Mandin-Darby Canine Kidney) cell line.

2.1. ABSTRACT

Both Influenza A virus (IAV) and Severe Acute Respiratory Syndrome Coronavirus 2 (SARS-CoV-2) belong to the group of RNA viruses. One, as well as the other viruses, are the trigger of pandemic and epidemic outbreaks in the world. Every year, the World Health Organization (WHO) records 3-5 million cases of severe flu and 290,000-650,000 deaths, and in the last 2 years of the pandemic, almost 652 million cases and over 6.5 million deaths have been reported to the WHO as caused by the Coronavirus disease 19 (COVID-19) pandemic. Both SARS-CoV-2 and IAVs attack the respiratory tract and cause similar symptoms. Due to the serious threat to public health posed by mentioned viruses, there is a need to look for new strategies to cure illnesses they cause and limit their spread.

The IAV genome consists of eight single-stranded, negative sense RNA segments. Each segment is a separate replication and transcription unit and encodes certain viral proteins. So far, it has been found that segments form complex secondary structures that contain conserved among virus strains motifs. It was also demonstrated that specific motifs play important roles in the viral replication cycle. Whereas SARS-CoV-2 has about 30 kb, 5' capped positive sense, single-stranded RNA genome. The role of some structural motifs of the viral RNA has been confirmed experimentally. Because of its functional importance and due to the fact that both viruses' replication cycles are RNA-dependent with no DNA intermediate, RNA makes a good target for potential new antiviral strategies.

In this work, the search for small molecules was carried out as potential inhibitors of IAV and SARS-CoV-2. 1280 compounds Lopac library and 8960 compounds Enamine library were searched using high throughput screening analysis with fluorescent indicator displacement assay. Conserved RNA structural motifs of IAV and SARS-CoV-2 were used as targets in the assay. Fourteen compounds from the Lopac library and twenty-one compounds from the Enamine library that bind to the RNA motifs were selected. Their inhibitory characteristics against the IAV A/California/04/2009 (H1N1) were next checked in MDCK cells.

The results indicate that most of the tested compounds from both libraries have the potential to inhibit influenza virus propagation by targeting viral RNA. The most crucial reduction of the relative vRNA copy number from the Lopac SMs was achieved by the influence of SML1545, B6311, and M4008 compounds. The mentioned SMs decreased the number of vRNA copies in the analyzed experiment by over 60%. Additionally, a significant reduction of viral titer was caused by SML2238. In the case of the Enamine library, three of the seven selected nontoxic compounds showed crucial inhibitory properties. Z154467994 showed the most significant inhibitory properties of all selected SMs. At 10 μ M, it reduced the relative vRNA copy number by over 36 % compared to the untreated control. While Z134817028 reduced viral RNA copy number by over 27% in the highest concentration. Z215664726 at the highest concentration lowered the relative vRNA copy number compared to the control by 35% and greatly decreased the viral titer.

What is more, in order to check the binding affinity of promising ligands to selected vRNA motifs and their binding site, molecular docking was performed. For this purpose, the molecular dynamics simulation of RNA motifs was conducted first. In accordance with trajectory analysis, clustering was performed. On the basis of which tertiary structures of selected RNA motifs were chosen and used for molecular docking with compounds found in previous experiments.

The described studies showed that the conserved structural motifs of the viral RNA are natural and good targets for antiviral strategies. However, the appropriate selection of the sequence and structural context of the RNA target site is of great importance for the activity of the inhibitor. Different antiviral approaches have different advantages and limitations that must be considered for their effective application. Moreover, the obtained results can contribute to the creation of an experimental basis for the design of effective and specific therapeutic strategies involving small molecules.

2.2. STRESZCZENIE

Zarówno wirus grypy typu A (IAV), jak i Drugi koronawirus ciężkiego ostrego zespołu oddechowego (SARS-CoV-2) należą do grupy wirusów RNA. Oba wirusy są przyczyną wybuchów pandemii i epidemii na świecie. Każdego roku Światowa Organizacja Zdrowia (WHO) odnotowuje 3-5 milionów przypadków ciężkiej grypy i 290 000-650 000 zgonów, a w ciągu ostatnich 2 lat pandemii COVID-19 do WHO zgłoszono prawie 652 miliony przypadków i ponad 6,5 miliona zgonów spowodowanych przez COVID-19. Zarówno SARS-CoV-2, jak i wirus grypy typu A atakują drogi oddechowe i wywołują podobne objawy. Ze względu na poważne zagrożenie dla zdrowia publicznego, jakie stwarzają wspomniane wirusy, istnieje potrzeba poszukiwania nowych strategii leczenia wywoływanych przez nie chorób i ograniczania ich rozprzestrzeniania się.

Genom IAV składa się z ośmiu jednoniciowych segmentów RNA o ujemnej polarności. Każdy segment jest oddzielną jednostką replikacyjną i transkrypcyjną, kodując określone białka wirusowe. Jak dotąd stwierdzono, że segmenty tworzą złożone struktury drugorzędowe, które są konserwatywne wśród szczepów wirusów. Wykazano również, że określone motywy odgrywają ważną rolę w cyklu replikacyjnym wirusa. Natomiast wirus SARS-CoV-2 posiada genom w postaci jednoniciowego RNA o dodatniej polarności o długości 30 kb, zakończony na końcu 5' czapeczką. Rola niektórych motywów strukturalnych tego wirusowego RNA została potwierdzona eksperymentalnie. Ze względu na swoje znaczenie funkcjonalne i fakt, że cykle replikacji obu wirusów są zależne od RNA bez pośrednictwa DNA, RNA stanowi dobry cel dla potencjalnych nowych strategii przeciwwirusowych.

W tej pracy prowadzono poszukiwania niskocząsteczkowych ligandów jako potencjalnych inhibitorów IAV i SARS-CoV-2. Przeanalizowano bibliotekę 1280 związków Lopac i bibliotekę 8960 związków Enamine za pomocą wysokowydajnej analizy przesiewowej z użyciem testu wyparcia wskaźnika fluorescencji (FID). Jako cele w analizie zastosowano konserwatywne motywy strukturalne IAV i SARS-CoV-2. Wyselekcjonowano czternaście związków z biblioteki Lopac i dwadzieścia jeden

związków z biblioteki Enamine, które wiążą się z danymi motywami RNA. Ich właściwości inhibitorowe wobec wirusa grypy A A/California/04/2009 (H1N1) zostały następnie sprawdzone w komórkach MDCK.

Przedstawione wyniki wskazują, że większość testowanych związków z obu bibliotek ma potencjał hamowania namnażania wirusa grypy poprzez działanie na wirusowe RNA. Najbardziej istotne zmniejszenie względnej liczby kopii wirusowego RNA wyselekcjonowanych ligandów biblioteki Lopac zostało osiągnięte przez wpływ związków SML1545, B6311 i M4008. Wymienione związki powodują spadek liczby kopii vRNA w analizowanym eksperymencie o ponad 60%. Ponadto SML2238 spowodował znaczną redukcję miana wirusa. W przypadku biblioteki Enamine trzy z siedmiu wybranych nietoksycznych związków posiadały kluczowe właściwości hamujące. Z154467994 wykazał najbardziej znaczące właściwości hamujące ze wszystkich wybranych SM. Przy stężeniu 10 μ M zmniejszył względną liczbę kopii vRNA o ponad 36% w porównaniu z nietraktowaną kontrolą. Z kolei Z134817028 zmniejszyło liczbę kopii wirusowego RNA o ponad 27% w najwyższym stężeniu. Z215664726 w najwyższym stężeniu obniżyło względną liczbę kopii vRNA w porównaniu z kontrolą o 35% i znacząco zredukowało ilość wirusa.

Co więcej, w celu sprawdzenia powinowactwa wiązania obiecujących ligandów z wybranymi motywami vRNA i ich miejsca wiązania przeprowadzono dokowanie molekularne. W tym celu najpierw przeprowadzono symulację dynamiki molekularnej motywów RNA. Zgodnie z analizą trajektorii przeprowadzono klasterowanie zasymulowanych motywów RNA. Podczas klasterowania wybrano struktury trzeciorzędowe wybranych motywów i wykorzystano je do dokowania molekularnego ze związkami wybranymi w poprzednich eksperymentach.

Opisane badania pokazują, że konserwatywne motywy strukturalne wirusowego RNA są naturalnymi i dobrymi celami dla strategii antywirusowych. Jednak odpowiedni dobór sekwencji i kontekstu strukturalnego miejsca docelowego ma ogromne znaczenie dla działania inhibitora. Różne podejścia antywirusowe mają różne zalety i ograniczenia, które należy wziąć pod uwagę w celu ich skutecznego zastosowania. Uzyskane wyniki mogą przyczynić się również do stworzenia

podstaw eksperymentalnych do projektowania skutecznych i specyficznych strategii terapeutycznych z udziałem niskocząsteczkowych ligandów.

3. INTRODUCTION

3.1 Influenza A Virus (IAV)

Influenza viruses cause highly contagious respiratory disease with possibly fatal outcomes. This disease has many symptoms, e.g., fever, headache, sore throat, sneezing, body ache, and cough. Influenza viruses belong to the *Orthomyxoviridae* family. Orthomyxoviruses are enveloped (-) strand RNA viruses. Influenza viruses are classified into four types: A, B, C, and D [1], [2]. The first three infections occur in humans. Human influenza A and B viruses cause seasonal epidemics of flu. Influenza A viruses are the only influenza viruses known to cause flu pandemics. A pandemic can occur when a new and different influenza A virus emerges, infects people, and can spread efficiently among people. Influenza C virus infections generally cause mild illness and are not thought to cause human epidemics. Influenza D viruses affect cattle and are not known to cause disease in people [1]–[4].

3.1.1. Structure and replication of IAV

The viral genome consists of eight negative single-stranded RNA (vRNA) segments that code viral proteins. All vRNA segments have conserved UTR (untranslated region) sequences at the 3' and 5' ends that flank the open reading frame¹. The vRNA segments are numbered according to their length - the longest is marked as segment 1, and the shortest as segment 8. It was believed that influenza virus genome encodes 11 essential viral proteins. The segments are also named after the main protein they code for. Segments 1–8 are called PB2 (Polymerase Basic 2), PB1 (Polymerase Basic 1), PA (Polymerase Acid), HA (Hemagglutinin), NP (Nucleoprotein), NA (Neuraminidase), M (Matrix), NS (Non-Structural), respectively [2], [3], [5].

The segments PB1, PB2, and PA code subunits of a viral polymerase attached to the partially mating 5' and 3' ends of each segment. Polymerase and multiple copies of the NP and vRNA form a ribonucleoprotein complex (vRNP). Each of them is separate and an independent replication-transcription unit. The structural protein M1 surrounds the complexes in the virion. The outer covering layer of the protein coat

is a lipid envelope. The virus is equipped with surface antigens – HA and NA - built into the lipid envelope. The M2 ionic channel resulting from the alternative splicing of segment 7 transcripts should also be distinguished. Like the M2 ion channel, the two non-structural proteins NS1 and NS2 / NEP arise from the alternative splicing of transcriptomes. Their primary function is to inhibit the interferon response of the host immune system and signal nuclear exports, respectively [2], [6]–[8].

IAVs can be classified into antigenic subtypes based on the antigenicity of their surface glycoproteins: HA proteins fall into classes H1 to H18, and NA proteins fall into classes N1 to N11. Only a limited number of these HAs and NAs have been isolated from viruses known to infect humans [9]–[11].

The epidemiology of human influenza viruses is defined by their constant antigenic variation to escape the host immune response. Influenza viruses possess two mechanisms for reinfecting humans and causing disease – antigenic drift and antigenic shift. Antigenic drift describes antigenic changes in the surface glycoprotein of virion as a result of point mutations in the antigenic epitopes. Antigenic drift variants cause epidemics and require the update of the vaccine strains. 1 to 5 years is the typical prevailing time before being replaced by other variants. The antigenic shift involves significant antigenic changes in HA /or NA, resulting in new HA and/or new HA and NA proteins in influenza viruses that infect humans. An antigenic shift can result in a new virus subtype. The antigenic shift can happen if influenza virus from an animal population gains the ability to infect humans. This kind of individual can contain HA/NA combinations that are significantly different from human viruses, so most people do not have immunity to the novel virus. In 2009 this kind of antigenic shift took place, where an H1N1 virus with genes from North American Swine, Eurasian Swine, humans, and birds emerged to infect people by spreading quickly and causing a pandemic [12]–[14].

Viral infection is a series of processes that enable the multiplication of a pathogen and its further transmission (Figure 1). Influenza virus, after depositing on the surface of potential host cells, binds to sialic acid to initiate infection and replication. Most sialic acids bind to galactose (Gal) or N-acetylgalactosamine (GalNAc) by α 2,3- or

α 2,6-linkages or to N-acetylgalactosamine by α 2,6-linkages. The specificity of the HA for the different sialyloligosaccharides is responsible for the host-range restriction of influenza virus. Human and H1N1 swine influenza viruses bind preferentially to Sia α 2,6Gal, but most avian and equine viruses have higher efficiency for Sia α 2,3Gal [15], [16].

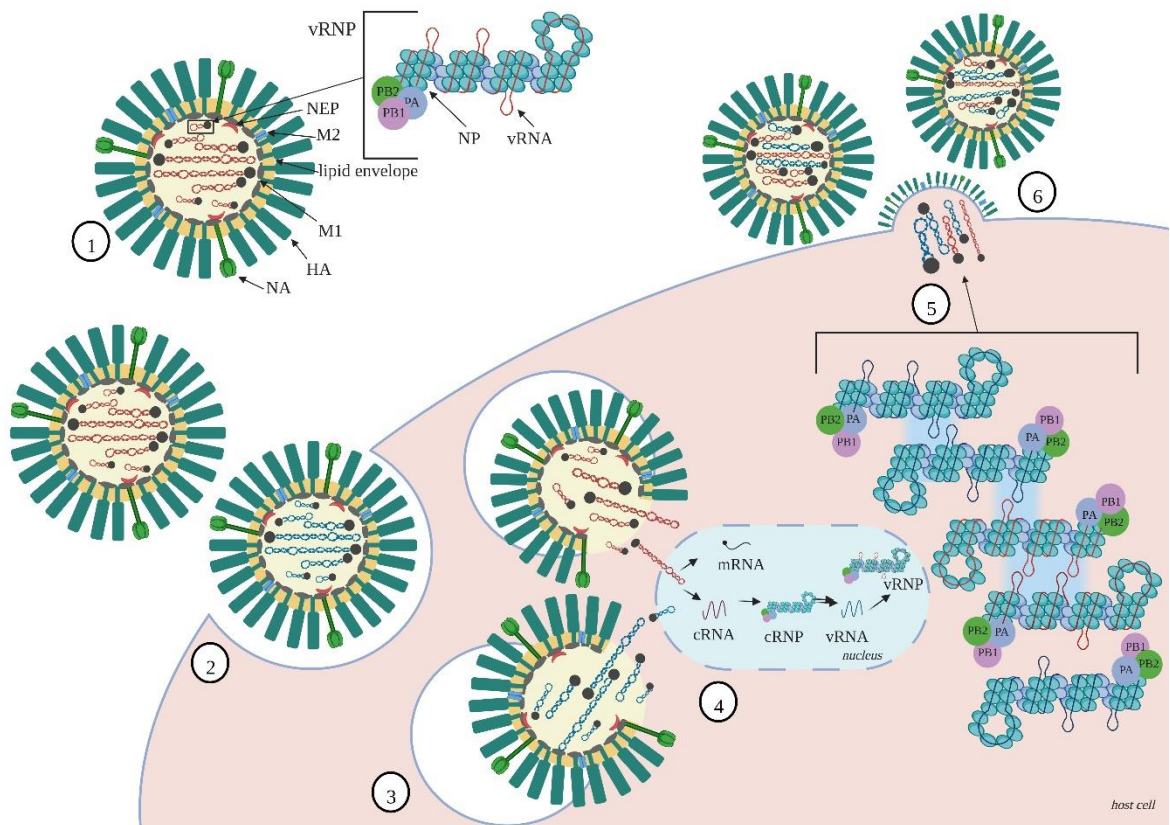


Figure 1. Influenza virus replication cycle and genetic reassortment: (1) schematic structure of complete influenza virion and vRNP; (2) the binding of virions to the host cell; (3) fusion between the viral envelope and the endosomal membrane. Red and blue vRNPs symbolize two distinct IAV strains during co-infection; (4) the viral genome entry to the nucleus, where replication and transcription take place; (5) genome assembly through vRNA–vRNA interactions of exposed structural motifs present in vRNPs. Compatibility of RNA packaging signals allows for co-segregation and genetic reassortment of specific segments between IAV strains. Red and blue vRNA/vRNP belong to distinct IAV strains, which undergo reassortment; and (6) accumulation of viral subunits at the budding site and the release of the new, reassortant viral progeny.

Influenza viruses require a low pH (around 5 to 6) to initiate fusion with endosomal membranes. This fusion activity is induced by an irreversible structural change in HA. Effective uncoating also depends on the presence of M2 protein and its ion channel activity. M2 protein allows the influx of the protons from the endosome into the virion, which disturbs protein-protein interactions and results in the free vRNP complex and M1 protein in the cytoplasm [12], [17], [18].

3.1. SARS-CoV-2

Coronaviridae family (CoV) is characterized by large, enveloped, single-stranded RNA. These viruses are the largest known RNA viruses, their genomes ranging from 25 to even 32 kb and virions diameter of 118 to 140 nm. Human coronaviruses, in most cases, cause relatively mild diseases of the upper and lower respiratory tract. They are estimated to account for almost a third of all common colds in humans. CoVs are found in humans and many other animal species. They are classified into four groups: α -CoV, β -CoV, γ -CoV and δ -CoV. β -CoV can infect mammals, while γ - and δ -CoV infect birds primarily [19]–[21]. In 2002-2003, when SARS-CoV appeared in China, approximately 8,000 people were affected, and the fatality rate was about 9.5% [22], [23]. In January 2020, a novel β -CoV was identified as the cause of the increasing occurrence of pneumonia in Wuhan, China. The virus is given the official name of Severe Acute Respiratory Syndrome Coronavirus 2 (SARS-CoV-2), and the disease caused by the virus is Coronavirus disease 19 (COVID-19). Due to the fact that 96,2 % of the SARS-CoV-2 is identical to a bat CoV RaTG13, it can be assumed that the virus originally came from bats and has been ultimately transmitted over time to humans. COVID-19 primarily spreads throughout the respiratory tract by direct contact, droplets, and respiratory secretions. Patients typically present a group of symptoms, such as: fever (88.7%), cough (67.8%), fatigue (38.1%), sputum production (33.4%), shortness of breath (18.6%), and headache (13.6%) [19], [24], [25].

3.1.1. Structure and replication of SARS-CoV-2

The viral RNA encodes four essential structural proteins: nucleocapsid (N) that surrounds the RNA genome and three membrane proteins: the S-glycoprotein (S), the matrix protein (M), and the envelope protein (E). There are as well non-structural proteins, including RNA-dependent RNA polymerase (RdRp). The S-glycoprotein is responsible for attaching to the cellular receptor angiotensin-converting enzyme 2 (ACE 2) on the surface of the human cells. ACE2 is abundantly located in the respiratory tract of humans, and it regulates cross-species and human-to-human transmission. Coronaviruses have a very high mutation rate due to the error-prone

RdRp, which is responsible for the duplication of genetic information. What is more, homologous recombinations often occur in coronaviruses. The effect of these components is a great diversity of coronaviruses in nature [24]–[27].

5` end of the genomic RNA features two large open reading frames – ORF1a and ORF1b, that encode 15-16 non-structural proteins. Fifteen of them compose the viral replication and transcription complex [19], [26], [28].

There are two different strategies for entering the host cell for SARS-CoV-2 virion, either plasma or endosomal membrane fusion (Figure 2). The S-glycoprotein mediates the attachment of the virion to the membrane of the host cell and through its interaction with ACE2 and cellular heparan sulfate as the entry receptors. In the case of plasma membrane fusion, the S-glycoprotein protein is activated by transmembrane protease serine 2 (TMPRSS2) in proximity to the ACE2. This process initiates fusion between the viral membrane and the plasma membrane. In case of the absence of TMPRSS2, the virus is able to be internalized by endocytosis. After entering the host cell, a lysosome-mediated drop in pH occurs in the endosome. The low pH environments activate the S-glycoprotein and prepare the virus for subsequent steps of fusion.

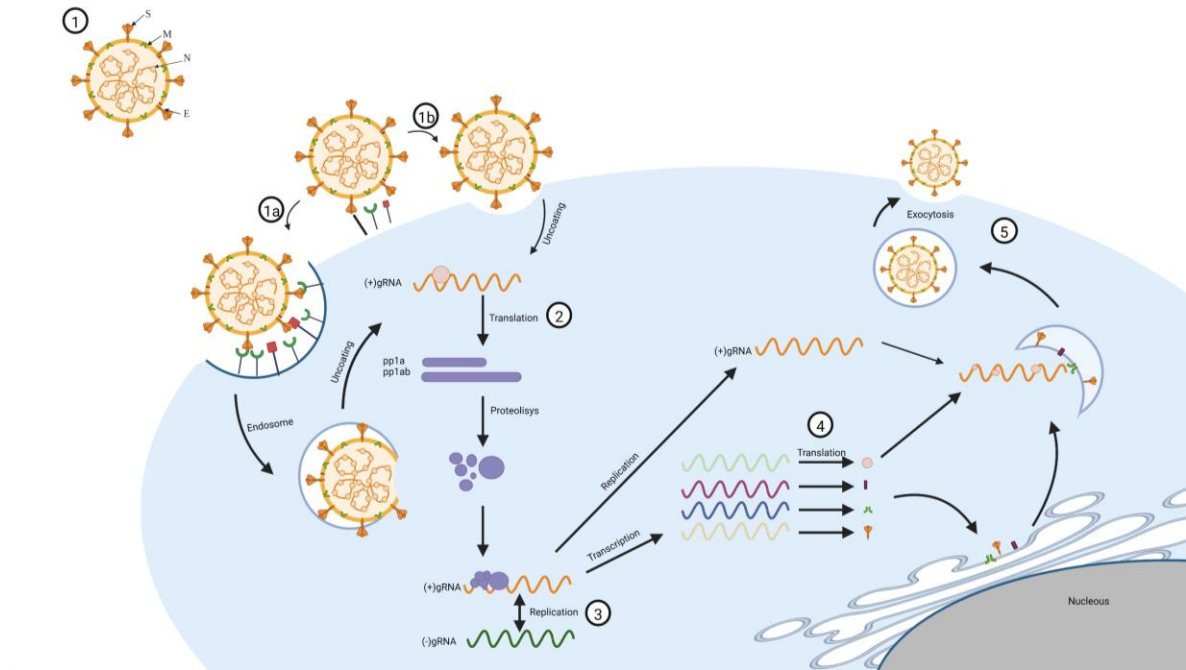


Figure 2. SARS-CoV-2 virus replication cycle: (1) schematic structure of complete SARS-CoV-2 virion; (1a) the binding of virions to the host cell by plasma; (1b) or endosomal membrane fusion; (2) release of the viral genome, uncoating and translating into viral polyproteins pp1a and pp1ab; (3) assemble into the replicate-transcription complex which replicates the (+)-sense genomic RNA ((+)gRNA). (-)-sense genomic RNA ((-)gRNA) is synthesized and used as a template to form (+)gRNA and subgenomic RNAs; (4) structural proteins are translated from sgRNAs and inserted into the endoplasmic reticulum from where they are transported to interact with the (+) gRNA-encapsidated N proteins and assemble into viral parts; (5) release of the new viral particle [29].

Nextly, the viral (+)-sense genomic RNA ((+)gRNA) is released into the cytoplasm. It allows the translation of the two polyproteins to produce over a dozen non-structural proteins (nsps) and the use of (+)gRNA as a template to form a replicase-transcriptase complex. After generating (-)-sense genomic RNA, it can serve as the template for the synthesis of (+)gRNA, which becomes the genome of the new virus particle. Transmembrane structural proteins pass through a pathway in the endoplasmic reticulum, including being synthesized, inserted, and finally folded. The N proteins, after translation in the cytoplasm, encapsulate (+)gRNA in the form of

nucleocapsids. After the assembling process, virions are transported to the cell surface through small vesicles [24], [26], [28], [30].

3.2. Inhibitory strategies

The vast majority of the approach for inhibitory strategies applied for the influenza virus and SARS-CoV-2 virus are focused on blocking the interaction between the viral protein and host cell. For the purpose of this dissertation, the focus was on the viral RNA targeting strategies of IAV and SARS-CoV-2 and selected groups of inhibitors.

3.2.1. Antisense Oligonucleotides

Antisense oligonucleotides (ASO) have become widely used research tools for specific inhibition of gene expression. Such oligomers are single-stranded DNA or RNA fragments with the limitation of length - sequences with usually 12–30 natural or modified nucleotides (shorter ones were also published). They bind specifically via Watson-Crick base-pairing. ASOs are able to modify the function of mRNA or other RNA, as well as degrade RNA or block gene expressions by complementary hybridization to the target. Thus, determine the ASO nucleotide sequence of the nucleotide. The mechanism of RNA degradation by ASO, which is DNA or gapmer, occurs through the activity of the endonuclease RNase H, which induces RNA cleavage [31], [32].

ASO targets RNA and modulates RNA splicing or gene expression, or other functions of RNA. Oligonucleotides generally act through two mechanisms in human cells. The first one is the cleaving of the target RNA via ASO-induced ribonuclease (RNase) H1 activity, and the second one is masking the target RNA from interaction with the RNA-binding proteins or the ribosome. ASO may be designed to complement a region of a particular gene or messenger RNA. Therefore, they can serve as prospective blockers of transcription or translation through sequence-specific hybridization with genetic segments. ASO are potentially of great importance in many treatment pathways (also with clinical examples) of cancer, neurodegenerative diseases, AIDS, herpes simplex virus, flu, and COVID-19[33].

Research on influenza virus inhibition using this strategy began in the 1980s. The first outline of the concept that it was possible to design an ASO that would provide

protection against infection by multiple strains of the virus appeared at that time. The first published work of this trend concerned DNA oligonucleotides selectively inhibiting the cytopathic effect caused by the influenza virus in the MDCK (Mandarin-Darby Canine Kidney) cell line [34]. The experiments were carried out for A/PR/8/34 (H1N1), A/Victoria/3/75 (H3N2), and A/Philippines/2/82 (H3N2) strains. The satisfactory inhibition effect was not achieved. A similar idea was realized in other studies using A/PR/8/34 (H1N1), A/Udorn/307/72 (H3N2), and A/New Caledonia/20/99 (H1N1) strains, and it was successful [35]. Conservative terminal region was also the target of high activity ASO in studies conducted on the highly pathogenic A/Tiger/Harbin/01/2002 (H5N1) strain [36]. What is more, the published papers also presented the results of modified ASOs. Oligomers targeting the PB1 and PA RNA segments proved to be able to inhibit the proliferation of A/PR8/34 (H1N1) and A/WSN/33 (H1N1) viruses in the plaque test [37], [38]. The inhibitory effect of modified ASOs acting on the NP protein binding site with RNA saved the infected mice from a lethal dose of the virus. Subsequent experiments aimed to target the conserved regions of the NS1 gene of the highly pathogenic A/Chicken/Henan /1/04 (H5N1) strain lowering the viral load under the influence of modified ASO [39]. It has been proposed that in the future, ASOs can be used as a form of prevention and therapy for influenza virus infections in humans. The published works also used synthetic nucleic acid analogs in the form of conjugates of morpholine oligomers and cell-penetrating peptides. The ASOs targeted the translation start site of PB1 and NP mRNAs, as well as the 3'-terminal region of NP vRNA of strain SC35M H7N7.67 [40].

Internal regions of genomic viral RNA segment 8 (vRNA8) of influenza A/California/04/2009 (H1N1) were a target for inhibition of viral proliferation using ASO, which was chosen by Lenartowicz et al. Designed ASOs targeted single-stranded, accessible regions of the internal regions of vRNA8. The researchers used mostly 2'-O-methyl RNA (2'OMeRNA), as well as ASOs, which contained modified locked nucleic acid (LNA) nucleotides for binding stabilization. The application of 7 from 10 tested antisense oligonucleotides resulted in the inhibition of virus growth at

least 3-fold in MDCK cells. ASOs 68-11L, 187-14L, and 404-14L are characterized by the highest inhibitory potential[41]–[43].

In Michalak et al. study, regions of the genomic viral RNA segment 5 (vRNA5) of influenza A/Vietnam/1203/2004 were a target for binding with ASO. Designed oligonucleotides were mainly 2'OMeRNA and 2'OMeRNA-LNA modified RNA. Five ASOs inhibited viral replication in MDCK cells, where the most potent ASO is characterized by a reduction of the viral titer of over 90%. The most potent inhibitory ASOs in this study are 883-11L, 474-21M, and 1253-13M [44].

In Soszynska-Jozwiak et al. research, the secondary structure of the segment 5 of (+) RNA of the IAV was determined, which is essential for well-designed sites available for ASO. The researchers used chemical mapping and thermodynamic energy minimization for structure determination. For the purpose of identification of the target site for ASOs, the microarray mapping and RNase H cutting were used. What is more, sequence analysis showed conservation between influenza A type strains of that the secondary structure of RNA segment 5 (+). Twenty-one nucleotides were tested, and nine of them presented inhibition of the IAV replication, where the most crucial inhibitory properties, over 7-fold inhibition of influenza A virus propagation, is represented for ASO 727A. Mentioned ASO targeted the long inner loop [45].

Another interesting approach is presented by Soszynska-Jozwiak et al. M121 structural motif of segment 5 (+)RNA secondary structure was investigated by chemical mapping and energy minimization. It is proven to be conserved between influenza A type strains. Six designed ASOs were tested in an inhibition assay with a single-cycle infectious influenza A virus (A/California/04_NYICE_E3/2009 (H1N1)) in the MDCK cell line expressing influenza hemagglutinin (MDCK-HA). 2A and 3A ASOs targeted the long hairpin, and the internal loop of M121 was able to inhibit virus proliferation (0.93 log₁₀ FFU/ml difference). The results of the experiments with ASO in the cell line support the biological importance of the conserved secondary structure of mentioned structural motif and suggest that it might be a candidate for future antiviral therapy [46].

One of the interesting approaches was used by Hagey et al. After the chemical mapping of the loop-stalk structure of PSL2 RNA they designed ASO with modified LNA. The PSL2 motif mediates viral packaging *in vitro*. It was found that the stem-loop structure of PSL2 was necessary for viral packaging in the cellular environment. Designed ASOs significantly inhibited the replication of IAV of various strains and subtypes. ASO9 had the most powerful antiviral properties [47].

As well as ASO can be used in the case of the influenza virus, and it is started to be served in the case of SARS-CoV-2. A popular ASO form in clinical use is based on a phosphorodiamidate morpholino oligomer (PMO) skeleton. PMOs have morpholine subunits instead of ribose/deoxyribose and are linked by the phosphorodiamidate group. PMOs have multiple advantages, such as reduced nonspecific binding imparted by the neutral charge and complete nuclease resistance [31], [48].

The highly conserved structured s2m element from the 3'UTR of SARS-CoV-2 was used as a target for LNA ASOs designed by Lulla et al. Three of six designed oligonucleotides are characterized by high-affinity for the target. Likewise, two other gapmers are different in polymer backbones only. The first gapmer, the entire length of the backbone is modified for improvement of the nuclease resistance. The second one is characterized by mixed backbone - a phosphodiester backbone of the DNA part phosphorothioate backbone of LNA-PS. The authors have shown that mentioned ASOs recruit RNase H and lead to RNA degradation. To test the antiviral effects of the designed LNA, ASOs authors used replicon-bearing SARS-CoV-2 s2m sequence, transfected to Huh7.5.1 and HEK293T cells. Measured luciferase activity revealed inhibitions of replicon replication by three of six gapmers. Moreover, it can be indicated that oligonucleotides designed against the s2m element have the prospective to decrease gene expression from mRNAs containing s2m in their 3' UTR sequences [49].

3.2.2. siRNA

The RNA interference (RNAi) as a term was coined after the groundbreaking discovery that injection of double-stranded RNA (dsRNA) into the nematode *Caenorhabditis elegans* leads to specific silencing of genes highly homologous in sequence to the delivered dsRNA [50].

Small interfering RNAs (siRNAs) consist of two antiparallel strands of RNA forming a duplex. Nowadays, during siRNAs design, it is usually placed at the 3' end of the so-called protruding ends composed of two mismatched thymidine nucleotides. siRNAs' role is to ensure the thermodynamic and enzymatic stability of the duplex under intracellular conditions unfavorable to nucleic acids. The length of RNA chains is usually within 21 nucleotides. Each strand plays a separate role in siRNA-initiated cellular processes. One of the strands, called the antisense or leader, carries a sequence complementary to the target region in the mRNA. The second one, called sense or passenger, corresponds to the sequence of the destination [51], [52].

Three siRNAs targeted the PA gene of the avian influenza virus (A/Tiger/HarBin/01/2002 H5N1) were investigated by Zhang et al. These studies were considered in terms of the ability of selected siRNAs to inhibit the replication of this virus. Due to the discovery that the N-terminal domain of PA contains an endonuclease active site, it became a crucial target for new anti-influenza drugs [53], [54]. Based on crystal structure analysis and mutagenesis studies of the N-terminal region of the PA gene, conserved in different subtypes and strains of avian influenza virus, explicit oligonucleotides were designed. Based on the presented results, it can be concluded that such PA gene-specific oligonucleotides inhibit the formation of vRNA, mRNA, and cRNA in MDCK cells. A considerable reduction of protein expression and vRNA level was shown by ps-PA496, resulting in almost 80-fold lower viral replication compared to the control, also confirmed by the significant reduction in fluorescence using the immunofluorescence assay [55].

Another novel approach was presented by Piasecka et al., who created siRNAs targeting structural motifs of segment 5 mRNA (mRNA5) of A/California/04/2009 (H1N1). This study, based on the secondary structure of the (+) RNA 5 segment, led

to significant inhibition of the virus proliferation. Twelve different regions of mRNA5 were targeted by researchers using different chemically modified siRNAs. Two of the tested siRNAs can be distinguished as molecules with the highest antiviral potential. The siRNAs 613 and 683 target highly conserved regions (613-631 nt. and 682-700 nt.) of the secondary structure of influenza virus mRNA5. According to these results, it can be understood that targeted motifs may play a crucial role in the viral life cycle. What is more, selected siRNAs were tested with a diverse number of modifications to improve siRNA inhibition. 2'-fluoro and triphosphate modifications showed the highest antiviral activity [56].

Jiang et al. used a swarm of DsiRNA molecule (chemically synthesized siRNAs, 25-27 nt length, substrates for Dicer enzyme) as an innovative way of inhibiting viral gene expression and, finally, production of new virions. The efficacy of DsiRNA swarming in preventing IAV infection in human primary monocyte-derived macrophages and dendritic cells was tested [57]–[59]. The work describes almost a hundred oligonucleotides targeting conserved regions of the IAV genome. Conservative sequences were classified by matching sequences of avian and swine viruses: A/chicken/Jiangsu/cz1/2002, A/goose/Jilin/hb/2003, A/swine/Henan/wy/2004, A/wild duck/Hunan/211/2005, and A/avian/Hong Kong/0828/2007, as well as human A/Hong Kong/482/97, A/VietNam/1194/2004, A/Anhui/1/2005. Selected conserved sequences were analyzed with siVirus software, which function is to search for potentially functional regions in the viral genome. The inhibition of various IAV strains replication was achieved through the RNA interference pathway with efficiency as high as 7-fold [57].

An interesting approach for anti-SARS-CoV-2 strategies using siRNA was shown by Niktab et al. Researchers designed six siRNAs that targeted M, S, E, and ORF3a, ORF1ab genes. They tested the influence of the siRNAs on the viability of the uninfected green monkey's cells (Vero E6) and showed no cytotoxicity. The effect of the siRNA was analyzed with Reverse-transcription quantitative real-time PCR (RT-qPCR). Infected cells have shown a lower copy number of the virus mRNA. All of

the selected siRNA inhibitors used in this research inhibit the activity of SARS-CoV-2 [60].

Eighteen various siRNAs were designed to target 5'UTR, RNA - dependent RNA polymerase (RdRp), and Helicase (Hel) genes of SARS-CoV-2 by Idris et al. Three of them were selected as the most potent for the inhibition of SARS-CoV-2 virus replication, and exhibiting dose-dependent effect. What is more, siRNAs were tested not only alone but also in combinations. However, both the single siRNA and the mixture of appropriate siRNAs were characterized by the same inhibitory effect. 2' O-methyl modified selected siRNA, siUTR3, had increased thermal stability in serum and provoke extended inhibition of SARS-CoV-2 replication, though unmodified siUTR3 is characterized by higher efficiency. *In vivo* testing was performed using the K18-hACE2 mouse model of COVID-19 disease, infected with SARS-CoV-2 (Australian VIC1 strain). The treatment resulted in less weight loss and a lower clinical score than control mice. Unfortunately, after six days of the experiment, the positive effect of siRNA was lost, suggesting that the repressive effect is transient. The research showed that tested siRNAs have a crucial impact on SARS-CoV-2 replication *in vitro* and *in vivo* [61].

3.2.3. PNA

A peptide nucleic acid (PNA) is an artificial nucleic acid analog with nucleobases linked to a neutral pseudopeptide backbone via a methylene carbonyl bond. PNA oligomers have found a great deal of use in molecular biology and as potential therapeutic molecules. PNAs are chemically stable and exhibit exceptional resistance to nucleases and proteases [62]–[64]. This is a particularly advantageous feature in the context of *in vitro* and *in vivo* activity of the molecule. PNAs are able to form duplexes by classic Watson-Crick base pairing with complementary strands in parallel or antiparallel orientation. PNA is also able to form triplexes with nucleic acids. Due to the fact that the PNA backbone is uncharged, there is no electrostatic strand repulsion characteristic of the sugar-phosphate backbone of DNA and RNA.

The binding affinity, specificity, and thermodynamic stability of PNA oligomers are significantly enhanced compared to natural DNA or RNA. The occurrence of even a single mismatch significantly reduces the melting point and durability of the duplex [65]–[68]. PNAs can also form Hoogsteen interactions, which lead to the formation of a triple helix. They show no particular binding selectivity to single-stranded or double-stranded nucleic acids. PNA can bind to the target region in a variety of ways, either by attaching to or disrupting existing structures. In the latter case, the homopyrimidine oligomers can form triplexes by unraveling double-stranded DNA or RNA regions and forming PNA•DNA-PNA or PNA•RNA-PNA structures. The two PNA strands in triplex form Watson-Crick and Hoogsteen pairs with the DNA or RNA strand, respectively [65], [68], [69].

The first known approach for inhibition of IAV replication using PNA was taken by Keszy et al. The researchers used a panhandle structure of the IAV virus as a target for a chemically modified short dbPNA oligomer (dsRNA-Binding PNA). Designed oligonucleotides were tested in MDCK cells in two different analyses: RT-qPCR and the Immunofluorescence Focus Formation Assay (IFA). The group has shown that the panhandle structure targeting dbPNA-neamine conjugate IR-1b is a potent antiviral agent against various subtypes (H1, H5, H7) of influenza A viruses.

Moreover, the researchers presented the modified dsPNA to bind selectively to the dsRNA region of the panhandle motif [70].

Rosenke et al. published an article about the inhibition of SARS-CoV2 in Vero-E6 cells by five, designed to target the 5'UTR and first translation start site region of SARS-CoV-2 positive-sense genomic RNA, peptide-conjugated morpholino oligomers (PPMOs). PPMOs are antisense compounds composed of a phosphorodiamidate morpholino oligomer covalently conjugated to a cell-penetrating peptide. Virus growth was evaluated by RT-qPCR and TCID₅₀ infectivity assay. Finally, four of the five PPMOs were highly effective, suppressing viral titers even up to 6 log₁₀. The RT-qPCR analysis showed that in cells treated with any of the four PPMOs, virus growth was markedly suppressed at 12–48 h post-infection [71].

An interesting idea of PNA inhibiting SARS-CoV-2 replication was made by Li et al. The researchers have chosen 5'UTR, 5'UTR TRS, and the polyprotein 1a/b translation start codon (AUG) of the SARS-CoV-2 genome as a target for eight designed long peptide nucleic acids covalently attached with cell-penetrating peptides (PPNAs). The effect was checked in the Vero-E6 cells. Cells were infected by the SARS-CoV-2 virus in the presence of the PPNAs. Based on the RT-qPCR studies, it was concluded that as the concentration of PPNAs in the experiment increased, the amount of the vRNA decreased. A PPNA targeting the 5'UTR of SARS-CoV-2, 5'UTR-PPNA1, was found to reduce the viral titer by >95% [72].

3.2.4. Small molecules

Small molecules (SMs) are chemical compounds with a molecular weight in the range of 0.1–1 kDa. Their undeniable advantage over biologics is targeting not only the extracellular components, like cell surface receptors, but also the intracellular proteins because they can easily cross the outer plasma membrane of the cell. SMs are relatively easy to synthesize by chemical reactions, and what is more, they are cheaper than biological drugs. SMs are mostly taken orally by the patients. They are usually designed to be metabolized from an inactive prodrug to an active compound. The small-molecule drugs are developed to follow Lipinski's rule of five. Lipinski's rule of five defines the characteristics of the chemical compound as SM: a molecule with a molecular mass less than 500 Da, no more than 5 hydrogen bond donors, no more than 10 hydrogen bond acceptors, and an octanol-water partition coefficient log P not greater than 5 [73]–[75].

During drug development, the pharmacokinetic issues of ADME (absorption, distribution, metabolism, and excretion) also need to be fulfilled for potential SM therapeutic. ADME governs that small-molecule drug has properties to be:

- 1) adsorbed by the human body,
- 2) easily distributed inside the human body,
- 3) metabolized to an active drug,
- 4) excreted out form the system.

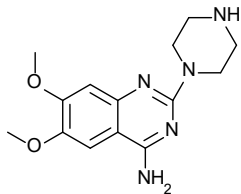
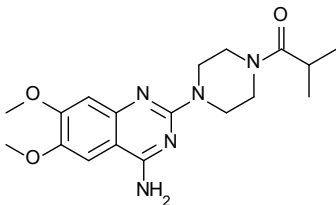
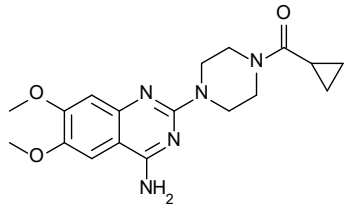
The vast majority of the therapeutic drugs generated by pharma industries are still small molecules and cannot wholly be replaced by biologics in the future [76].

The design of nucleic acid ligands has been pursued for over 30 years. The Dervan group first pioneered the fields of optimizing DNA-binding molecules [77]. The Disney group identifies selective RNA-binding molecules. In the recent 15 years, researchers have established that “the right” synthetic small molecules can indeed bind to RNA structures, but not the primary sequences, with a high degree of selectivity [78]–[81].

One of the approaches is represented by Varani et al., where the panhandle structure of IAV is tested with 4,279 compounds during NMR-based screening. 6,7-Dimethoxy-2-(4-phenylpiperazin-1-yl)quinazolin-4-amine was identified in this study as a bounded to panhandle IAV structure with a K_d around 51 μM . Moreover, the NMR structure of the new-created complex shows binding tightness between described small molecule and the major groove of the internal loop. An FDA-based CPE assay was used to determine the inhibitory activities of the 6,7-dimethoxy-2-(1-piperazinyl)-4-quinazolinamine (Table 1). The presented results show that SM does not influence cell viability up to 500 μM . SM was tested for replication inhibition with two IAV strains and one IBV, and the inhibition degree was lower than in the case of amantadine, oseltamivir, and ribavirin.

Furthermore, plaque reduction assay results showed inhibition of virus growth in SM concentration between 56 to 500 μM . To sum up, the SM binding changes the panhandle structure and could interfere with the binding of RdRp and consequently disturb replication. Later, analogs of 6,7-dimethoxy-2-(1-piperazinyl)-4-quinazolinamine were designed and tested, discovering at least two (compounds 7 and 10; Table 1) with high inhibitory activity and low cytotoxicity [82], [83].

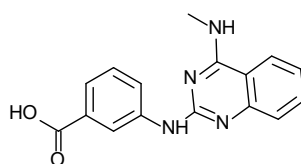
Table 1. Structures of SMs with the highest inhibitory activity and low cytotoxicity [82], [83].

6,7-dimethoxy-2-(1-piperazinyl)-4-quinazolinamine	Compound 7	Compound 10
		

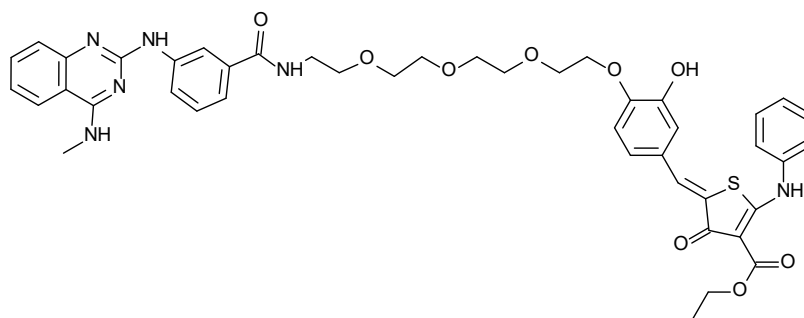
Another study is conducted by Haniff et al. SMs targeting an attenuator hairpin (AH) of SARS-CoV-2 frameshifting element (FSE). 3,271 SMs library was checked by Inforna software, and the microarrays approach was next used to select the most

promising compounds. Five SMs were selected as compounds that bind to the FSE model. C5 can be considered the most interesting SM of the selected ones (Figure 3). C5 is characterized by decreasing frameshifting efficiency by $25 \pm 1\%$ in the frameshifting model in the HEK293T cells by stabilizing the AH structure. Furthermore, the binding site of C5 in cells in the presence of vRNA was determined. Two of the C5 analogs were synthesized: C5-RIBOTAC and C5-Chem-CLIP, which showed the specificity of binding of C5 to the SARS-CoV-2 FSE element [84].

C5



C5-RIBOTAC



C5-Chem-CLIP

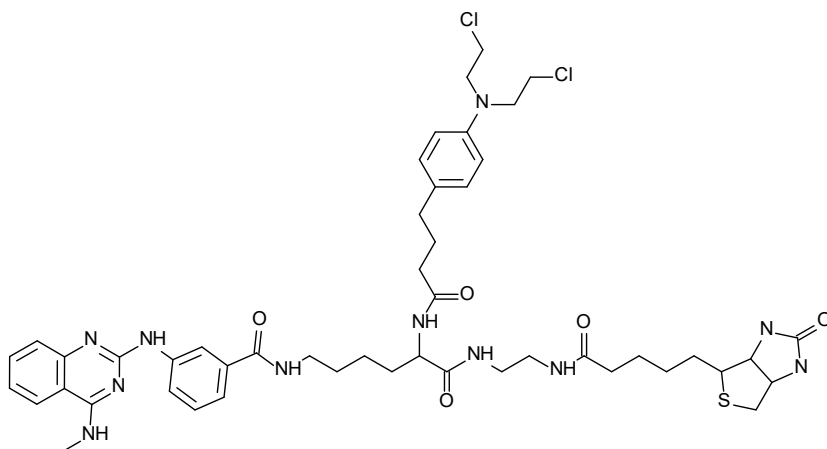


Figure 3. Structures of C5, C5-RIBOTAC and C5-Chem-CLIP compounds [84].

NMR-based screening of the DSI-poised library of 768 compounds was conducted by Sreeramulu et al. 15 structural motifs of SARS-COV-2 genomic RNA were selected. Motifs are characterized by thermodynamic stability *in vitro*, existence *in vivo* and *ex vivo*, and, what is more, conservation between SARS-CoV and SARS-CoV-2. Studies identified 40 SMs that bind to the 15 RNA motifs. To sum up, researchers identify RNA motifs with affinities to selected SMs between 60–400 μM . It allows them to identify known and commercially available binders containing similar structural motifs. One of the identified binders, D01 (Figure 4), binds with 6 μM affinity to two different RNA motifs, PK and S2m hairpin. This compound is promising for continuation in the development of a lead compound [85].

D01

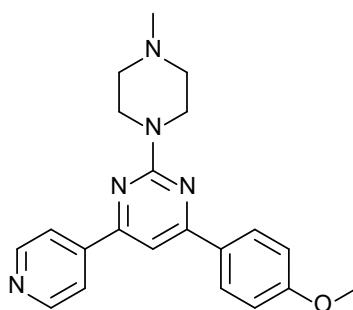
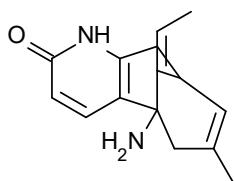


Figure 4. Structure of D01 compound [85].

Chen et al. presented the reporter system of the SARS-CoV-2-1 PRF based on FLuc. It was used in high throughput screening (HTS) of FDA-approved compounds. 52 SMs were selected and validated in a dual fluorescent protein reporter system. Huperzine A and ivacaftor (Figure 5) seem to be active in the destruction of frameshifting in the model system. Nonetheless, the effectiveness of selected SMs as inhibitors of SARS-CoV-2 propagation must be confirmed in further research [86].

Huperzine A



Ivacaftor

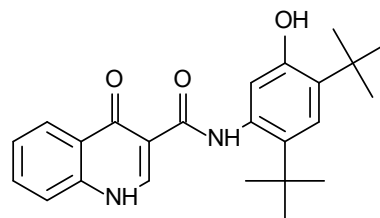


Figure 5. Structures of Huperzine A and ivacaftor [86].

Four thousand four hundred thirty-four compounds were screened with GFP/mCherry reporter system in HTS to find small molecules that impair programmed -1 ribosomal frameshift (-1 PRF) promoted by an RNA pseudoknot. Desired SM should be disturbing in the translation process of open reading frame 1b (ORF1b). This approach was presented by Sun et al. Next, eight selected SMs were tested in a luciferase-based PRF reporter assay, and one of them, merafloxacin (Figure 6), appeared to be an efficient inhibitor hampering SARS-CoV-2 replication in Vero E6 cells. For proving changes in frameshifting, the abundance of nsp8 and nsp12 was quantified by the authors, and indeed they observed that their relative amount was reduced [87].

Merafloxin

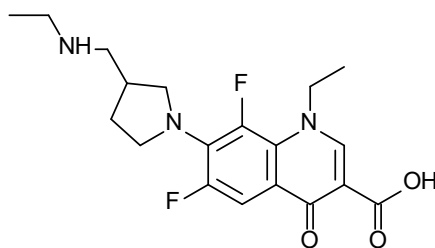


Figure 6. Structure of merafloxin [87].

4. RESULTS AND DISCUSSION

The application of small molecules targeting RNA as promising inhibitors of viral replication for IAV and SARS-CoV-2 is a relatively new approach in inhibitory strategies. The development of new strategies and new therapeutic objects are essential for new drug development. The presented research uses High Throughput Screening (HTS), Molecular Dynamic Simulations (MDS), and Molecular Docking (MD) of selected SM to find new inhibitors of viral replication of IAV and SARS-CoV-2 targeting viral RNA. The objects of the study were vRNA structural motifs of the IAV and SARS-CoV-2.

The particularized aims of the research were implemented in individual steps. The HTS analysis goal was to find small molecules that strongly bind to selected conserved structural motifs of IAV and SARS-CoV-2 RNA. The research's second step was applying MDS to determine and characterize 3D structures of selected vRNA motifs. During the molecular docking analysis, the binding site in conserved vRNA structural motifs of the best small molecules was specified. In the last of the presented stages, the evaluation of the antiviral potential of the selected small molecules against a strain of influenza A virus, A/California/04/2009 (H1N1), in the MDCK (Mandin-Darby Canine Kidney) cell line was carried out. The results of the conducted research are presented in the following subsections.

4.1. Selected RNA structural motifs

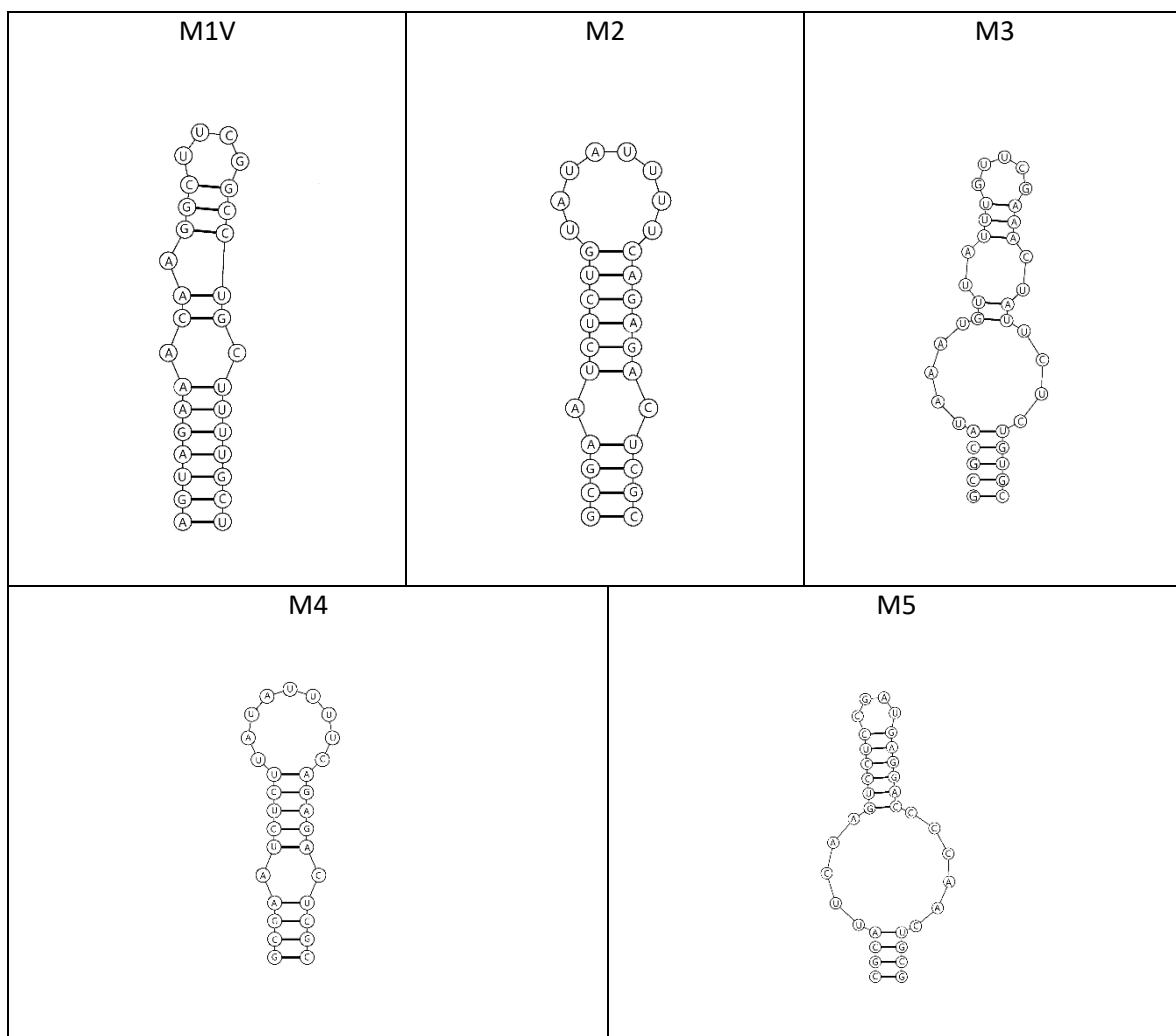
Based on bioinformatic and structural analyzes and using the experience of the research group in which the said doctoral thesis was created, five conserved RNA motifs of the IAV were selected for each research part. Selected RNA structural motifs are presented below (Table 2), as well as a brief description of their origin (4.1.1).

Using databases, structural experience, and publications available so far, seven RNA structural motifs from the SARS-CoV-2 virus were selected. The secondary structure of selected RNA motifs is presented (Table 3), and a brief literature description is provided below (4.1.2).

4.1.1. IAV RNA motifs

The selected vRNA structural motifs are conserved motifs of the influenza A virus. The motifs are present in segment 8 of the IAV vRNA and in the case of the M1V motif in each of the eight influenza segments. A description of the selected RNA motifs (Table 2) and the motifs' secondary structure are presented below.

Table 2. Secondary structures of the selected IAV RNA motifs used in High Throughput Screening and Molecular Docking.



M1V is a panhandle motif of vRNA, highly conserved (98%), and present in each segment of influenza A vRNA of each strain [88], [89]. M1V is necessary for virus polymerase to bind and is formed by base pairing of 3'- and 5'-ends of vRNA. The panhandle structure and its changes are essential for transcription and replication

[70]. It was shown that targeting panhandle motif with antisense oligonucleotides and SMs inhibits IAV replication [90].

M2 is a conserved hairpin of vRNA8 of a region 719-782 nt. The motif is located in the packaging regions of the virus and is necessary for infectious virus formation [89], [91]. Therefore it is an excellent target for SMs binding.

M3 is a conserved structural hairpin of vRNA8 of region 92-125 nt. The presence of the motif is confirmed *in vitro* and *in vivo* [89], [91]. Thermodynamic stability of the described motif is improved in the model used in a study by modification – adding 2 pairs: C-G and G-C.

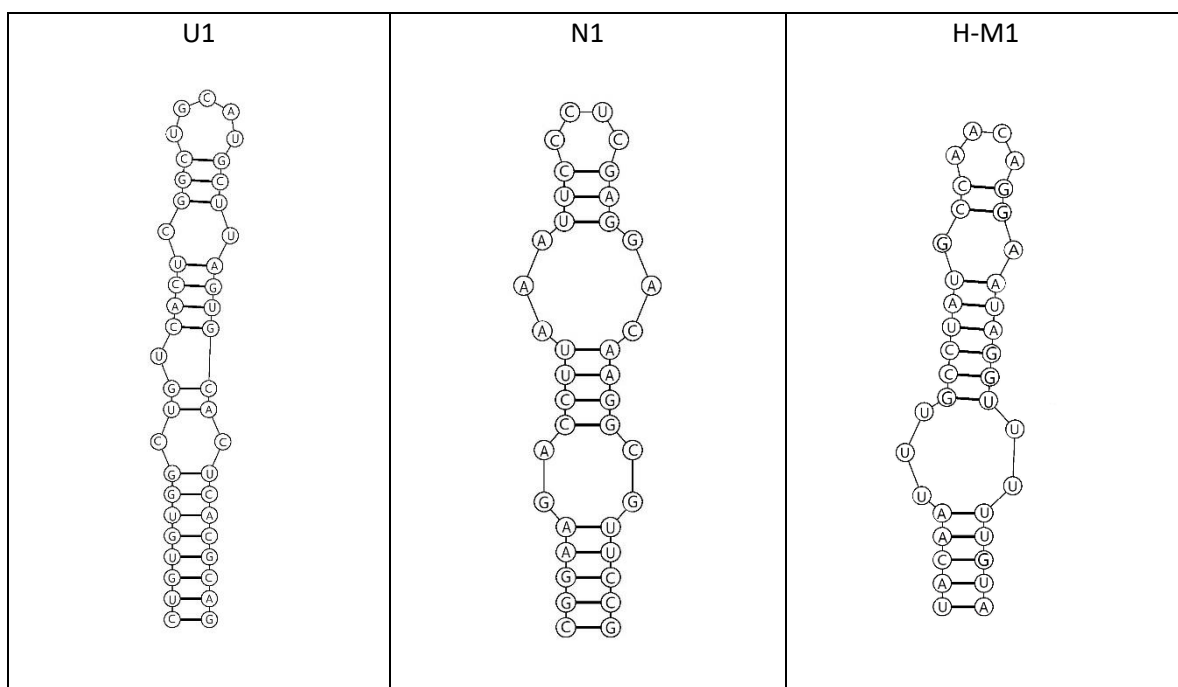
M4 is a conserved structural motif of vRNA8 of region 261-288 nt. The presence of the M4 motif is confirmed *in vitro* and *in virio* by two laboratories for different influenza strains using chemical mapping [89], [91].

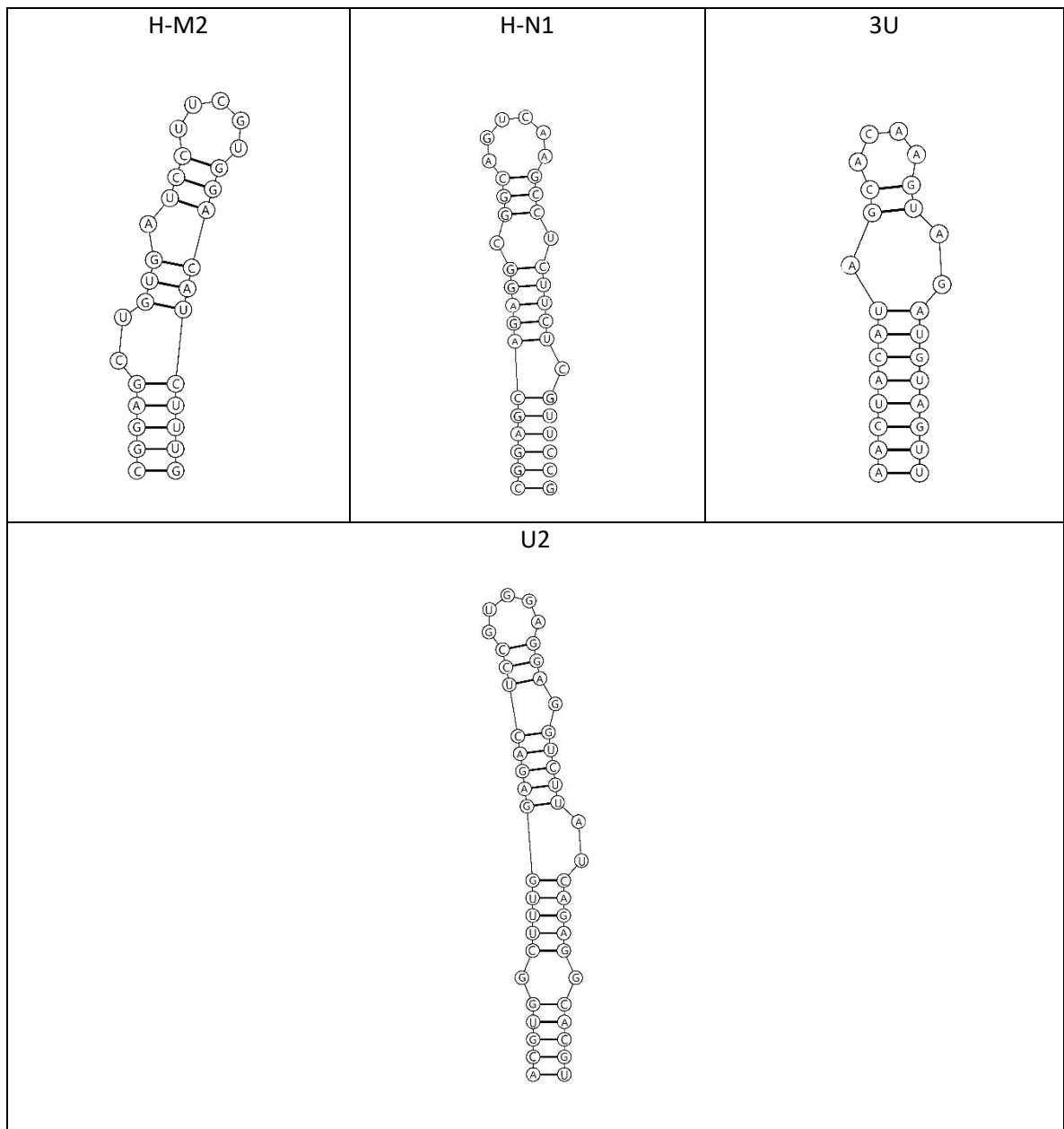
M5 is a conserved motif of vRNA8 of region 305-335 nt. The presence of conserved M4 and M5 motifs is confirmed *in vitro* and *in virio* (in influenza virion) by two laboratories for different influenza strains using chemical mapping [89], [91]. The hairpin is modified in the RNA model used in the study compared to the vRNA IAV sequence by adding two G-C and C-G pairs for better thermodynamic stability.

4.1.2. SARS-CoV-2 RNA motifs

Based on bioinformatics predictions, seven structural motifs of the SARS-CoV-2 were selected. They are characterized by high structural conservation. Over time, these motifs' presence has also been confirmed in *in virio* experiments. Some motifs have been modified to increase thermodynamic stability compared to the wild type. The following subsection presents both secondary structures (Table 3) and a description of selected RNA motifs.

Table 3. Secondary structures of the selected SARS-CoV-2 RNA motifs used in High Throughput Screening and Molecular Docking.





N1 is a hairpin in the N gene (28456-28491 nt.) predicted by bioinformatic analyses and proved to be present in virion [92]. The hairpin model for the study is modified compared to the vRNA SARS-CoV-2 sequence by changing the G-U pair to the G-C pair for better thermodynamic stability.

U1 is a motif in literature known as the **SL4 motif** (84-127 nt). The U1 is characterized by relatively high thermodynamic stability. Moreover, the U1 motif possesses the start codon of an upstream open reading frame [93], [94].

U2 is a motif in literature known as the **SL7 motif** (349-394 nt.) and is a hairpin within 5'UTR. SL7 is conserved across betacoronaviruses, and its viral functionality is confirmed in many studies [95]. *In virio* structural probing of SARS-CoV-2 RNA proved the presence of the SL7 motif [92]. Also, bioinformatic RNA analyses of SARS viruses predicted SL7. Probably, The SL7 is analogical to the motif also discovered in bovine coronavirus. The presence of SL7 was confirmed by structural probing of SARS-CoV-2 *in vivo* [92], [96].

H-M1 motif is a hairpin (26942-26971 nt.) from the M gene, predicted by bioinformatic analyses and proved in structural studies *in virio*. The motif is characterized by high thermodynamical stability [92].

H-M2 motif is present in the M gene (26901-26930 nt.). The presence of the hairpin was confirmed in structural studies *in virio*. Additionally, it is characterized by excellent thermodynamic stability [97].

H-N1 is a hairpin from the N gene (28796-28832 nt.) The motif is confirmed to be present in virion [92]. The H-N1 model for the study is modified compared to the vRNA SARS-CoV-2 sequence by adding a C-G pair for thermodynamic stability improvement.

3U motif is a hairpin (29663-29689 nt.) from the 3`UTR motif. The proximity to 3`UTR pseudoknot is defining feature of this hairpin. The 3U is conserved across coronaviruses, and its presence is proven by chemical mapping. The motif is involved in the replication of SARS-CoV-2 and the packaging of virus particles [98].

4.2. Selection of SMs from Lopac and Enamine library

High Throughput Screening (HTS) is a novel approach applied in biological and chemical science, especially in drug design. The method consists of an automated process with the use of various robotics, control software liquid handling devices, and sensitive detectors. Thanks to HTS, it is possible to conduct a large number of tests in a relatively short period of time. This automated testing of large numbers of chemical compounds is performed for a specific biological target.

The HTS experiments presented in this dissertation were conducted in collaboration with the Molecular Assays Laboratory (dr M. Otrocka) and High Throughput Screening Laboratory (dr R. Pilarski) of the Institute of Bioorganic Chemistry, PAS.

The method used in conducting HTS is a published one called fluorescent indicator displacement assay (FID). FID enables the identification of small molecules binding to nucleic acids [99], [100]

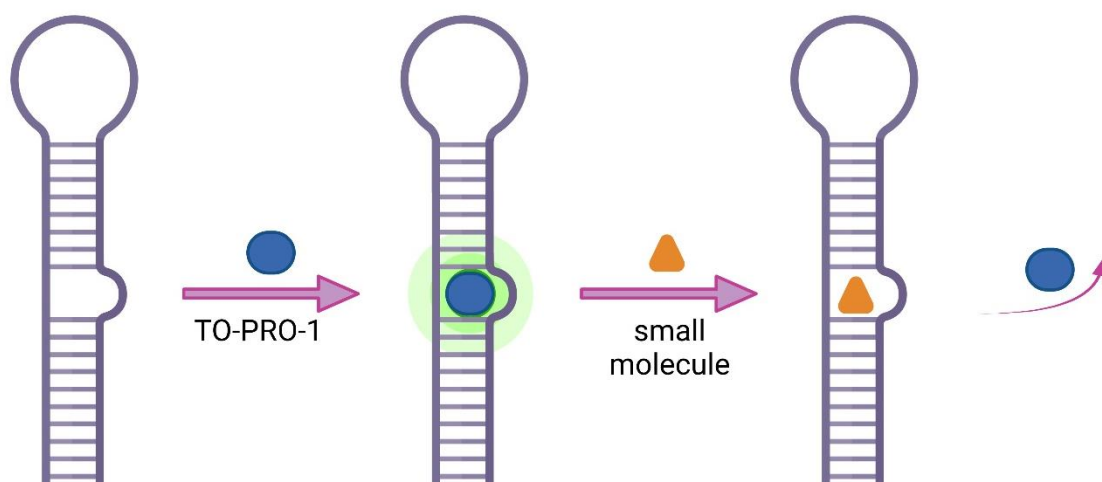


Figure 7. Scheme of acting of the TO-PRO-1 fluorescent dye (blue circle) in FID assay with an example of an RNA structural motif (purple hairpin motif) and a small molecule (orange triangle). The principle of operation presented in the diagram is as follows: during the binding of the fluorescent dye to the RNA structural motif, the fluorescent signal increases, and then,

after the addition of the ligand, if the compound binds to the nucleic acid, the signal decreases.

Small molecules that bind to RNA motifs have been identified using a TO-PRO-1 dye-displacement assay, which concise working principle is presented above (Figure 7). TO-PRO-1 is a popular dye for fluorescent assays with Excitation/Emission 515/531 nm (Figure 8).

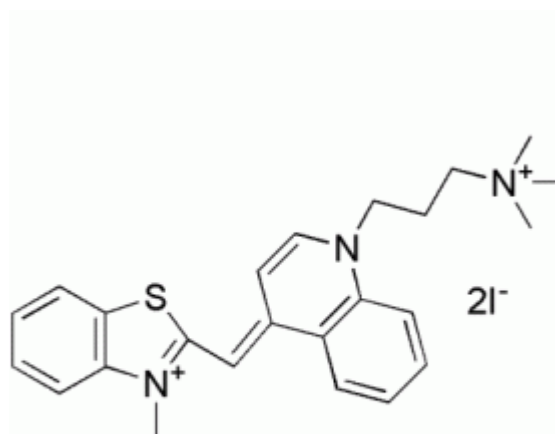


Figure 8. Structure of the fluorescent dye TO-PRO-1 Iodine.

The High Throughput Screening analysis consists of a series of steps (Figure 9). In the first step, called preparation of the assay, several sub-stages of optimization can be distinguished: determining the conditions (screening buffer, folding of RNA) to obtain a proper and stable secondary structure for each RNA; confirming adequate binding for a fluorescent indicator; selecting the optimal RNA concentration to measure the fluorescence intensity; determining the EC_{50} , for each RNA motif and the IC_{50} value for the reference small molecule. In this experiment, it was determined that SM_{ref} would be used in excess of 1000 nM due to the ease of conducting the investigation.

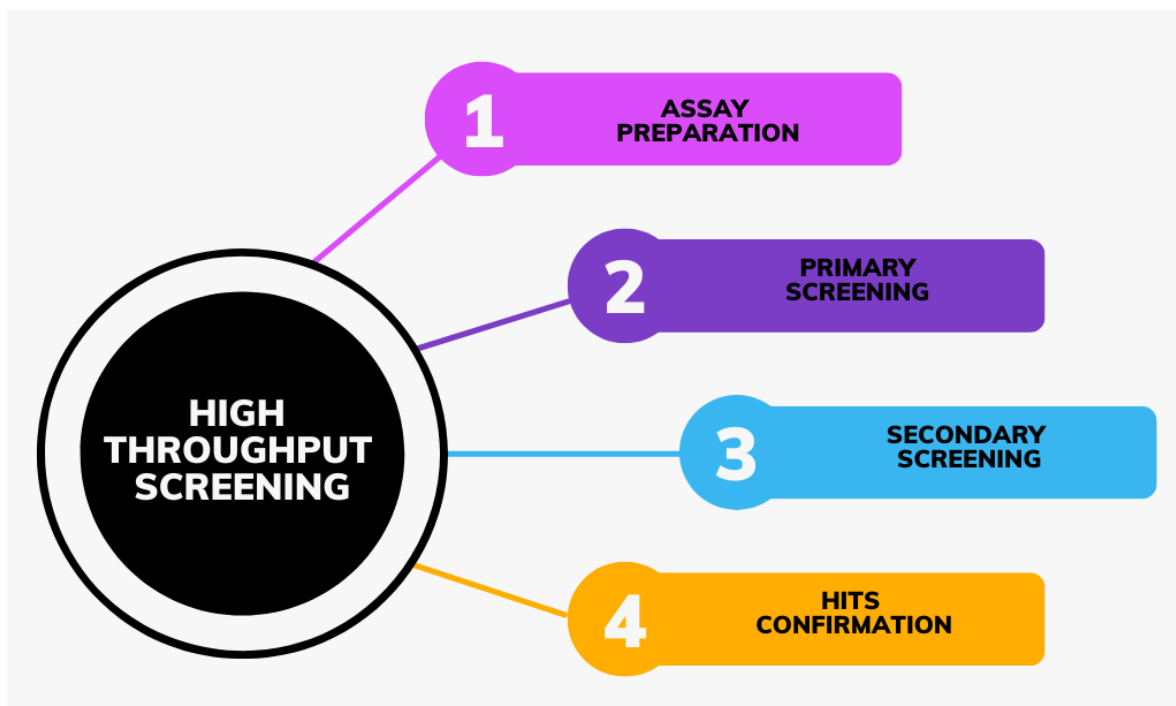


Figure 9. Scheme of steps conducted in HTS.

The term EC_{50} refers to half maximal effective concentration and is a highly relevant parameter for drug discovery and analysis. In the case of this experiment, it is the concentration of the selected RNA motif that is effective in half of the maximum value of the induced fluorescence signal when the indicator is present. The IC_{50} is the half maximal inhibitory concentration and is a convenient way of comparing drug potencies. In this experiment, the term IC_{50} is understood as the ligand concentration at which the fluorescence signal is halved.

During the primary screening in the described experiment, all compounds of the library were combined with each studied RNA motif in a single repetition based on the detection of a decrease in the fluorescence signal of the indicator. The secondary screening examines the compounds selected in the previous stage of the HTS analysis, which is carried out in 3 repetitions for all RNA structural motifs. The last step, called hits confirmation in this research, is understood as examining the selected SMs from the secondary screening in a range of concentrations (achieving selected SMs dose-response curves) in triplicate.

This chapter has been divided into three subsections, presenting the results of two high throughput analyses performed separately. The first one is an introduction to assay preparation. The second was for the Lopac library HTS, in which 11 RNA structural motifs were tested: 4 from the IAV and 7 from the SARS-CoV-2. The last section describes the results of the HTS with the Enamine library for 8 RNA structural motifs: 1 from the IAV and 7 from the SARS-CoV-2.

In each of the HTS experiments described below, M1V structural motif (panhandle model, Table 2) was chosen as a reference motif, as well as 6,7-dimethoxy-2-(1-piperazinyl)-4-quinazolinamine as reference SM (SM_{ref}) that was proved to bind to the panhandle model with $K_d 50.5 \pm 9\mu M$ [90].

4.2.1. High Throughput Screening Assay Preparation

Several preparations were made before the start of the experiments. Screening buffer was chosen based on publication, and detailed conditions of preparing RNA solutions are described in Materials and Method (6.1.5 Buffers; 6.2.17 High throughput screening (HTS)). The first step was checking the fluorescence signal's stability over time for RNA motifs. Based on this experiment and the reference publication, RNA with a fluorescent marker incubation time was set at 15 minutes. Next, EC_{50} was calculated. The EC_{50} values obtained for all selected RNA motifs during the research are presented below (Table 4). The EC_{50} value was determined for each vRNA motif as described in the Materials and Methods (6.2.15 Determination of EC_{50}).

Table 4. EC_{50} values for the RNA structural motifs tested in HTS.

RNA motif	EC_{50} [nM]
M1V	500
M2	600
M3	700
M4	1000
M5	1000
U1	600
N1	600
H-M1	600
H-M2	750
H-N1	300
3U	900
U2	650

For positive control, 6,7-dimethoxy-2-(1-piperazinyl)-4-quinazolinamine (reference small molecule; SM_{ref} ; Figure 10) was selected, which was found to bind strongly to the M1V (reference motif, Table 2) and should significantly decrease fluorescence [90]. Indeed, IC_{50} for SM_{Ref} binding to M1V was equal to 60.5 μ M. RNA/TO-PRO-1 treated with DMSO without SM served as a negative control when the fluorescent signal remained.

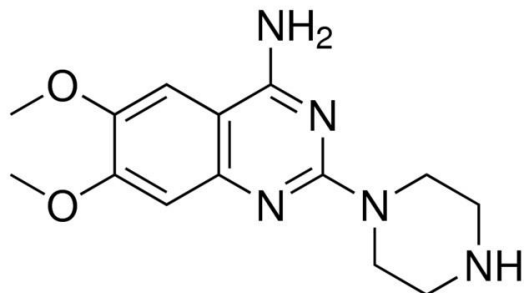


Figure 10. Structure of reference inhibitor (SM_{ref} ; 6,7-dimethoxy-2-(1-piperazinyl)-4-quinazolinamine).

The reference inhibitor concentration for all RNA motifs was set at 1000 nM and was checked to see if it binds to other RNA motifs besides M1V. Because a confirmed SM that binds to other selected RNA motifs was unknown, it was assumed that SM_{Ref} could eventually be a reference binder to other tested RNA. The high excess of the SM_{Ref} compared to tested RNA motifs guaranteed the detection of possible binding. Indeed, for most RNA motifs at this high concentration, SM_{Ref} appeared to be a good compound for positive control.

The fluorescent signal of TO-PRO-1 dye incorporated in RNA structure was monitored after incubation with small molecules. The results were compared to the intensity of the signal obtained for negative and positive control and normalized as described in Material and Methods.

Z' factor assessed the assay quality by the following formula:

$$Z' \text{ - factor} = 1 - \frac{3(\sigma_p + \sigma_n)}{|\mu_p - \mu_n|}$$

Where μ_n and σ_n represent the mean and standard deviation of the negative controls, and μ_p and σ_p represent the mean and standard deviation of the positive controls [101], [102]. The interpretation of the Z' -factor criteria is following:

- Z' -factor = 1 – ideal, never exceed,
- $1.0 \leq Z'$ -factor ≥ 0.5 – excellent quality of the assay,
- $0.5 \leq Z'$ -factor ≥ 0.0 – marginal quality assay [101].

All the data points were normalized to positive and negative control as 100% and 0% reduction of fluorescent signal, respectively, for each screening plate (Table 5).

Table 5. Z' factor of HTS for IAV and SARS-CoV-2 RNA motifs.

RNA motif	Z' factor
M1V	0.80 ± 0.16
M4	0.72 ± 0.11
U1	0.82 ± 0.07
N1	0.66 ± 0.19
H-M1	0.53 ± 0.27
H-M2	0.79 ± 0.15
H-N1	0.81 ± 0.11
3U	0.69 ± 0.22
U2	0.69 ± 0.23

Due to problems with the assay quality based on the low Z' factor value for M5 - it was rejected in further research. Moreover, due to the problem with structural stability, M2 and M3 were denied.

In conclusion, the HTS assay was established for selected RNA motifs: M1V, M4, U1, N1, H-M1, H-M2, H-N1, 3U, and U2.

4.2.2. Lopac Library

The first library tested with high throughput screening was the Lopac library. This is a collection of 1280 bioactive small molecule compounds, where all the primary target classes are represented. It contains marketed drugs and pharmaceutically relevant compounds annotated with biological activities.

The following RNA structural motifs were used as targets in using this library:

- IAV motifs – (Table 2):
 - M1V;
 - M4.
- SARS-CoV-2 motifs – (Table 3):
 - N1;
 - U1.

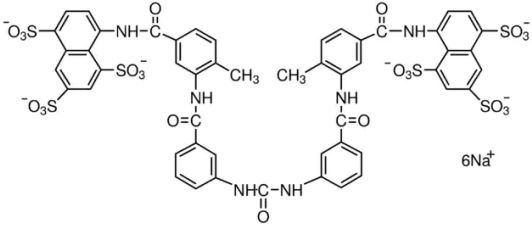
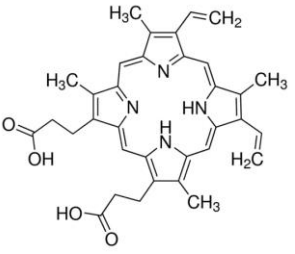
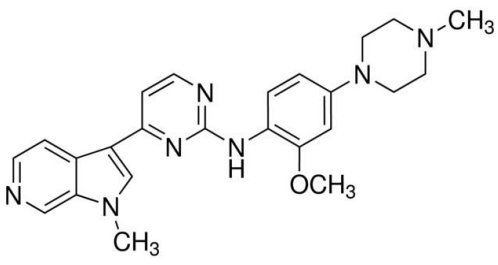
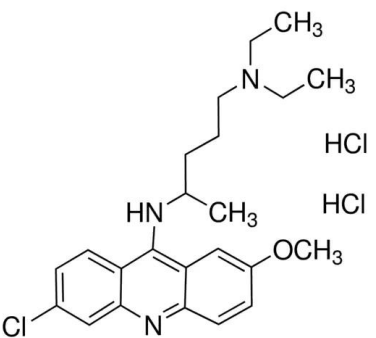
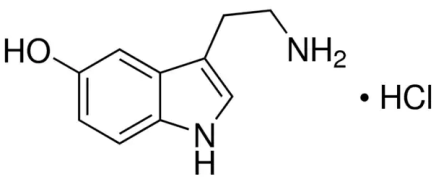
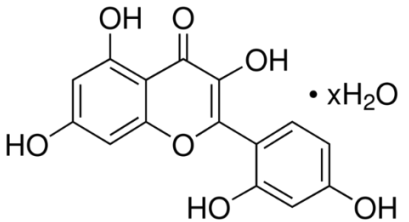
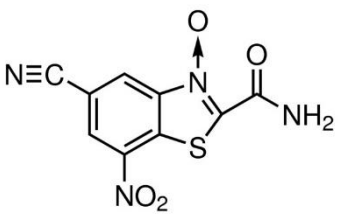
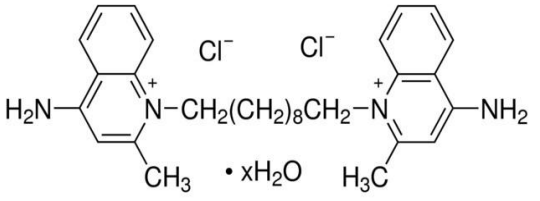
The HTS was performed as described in Methods and Materials (6.2.17 High throughput screening (HTS)). Primary screening was performed, where all RNA motifs were tested against all compounds from the library with an additional reference compound: SM_{ref} . The cut-off value has been established, above which all selected compounds were called hits. The cut-off was calculated based on average plus three standard deviations of the observed fluorescence response for all library compounds.

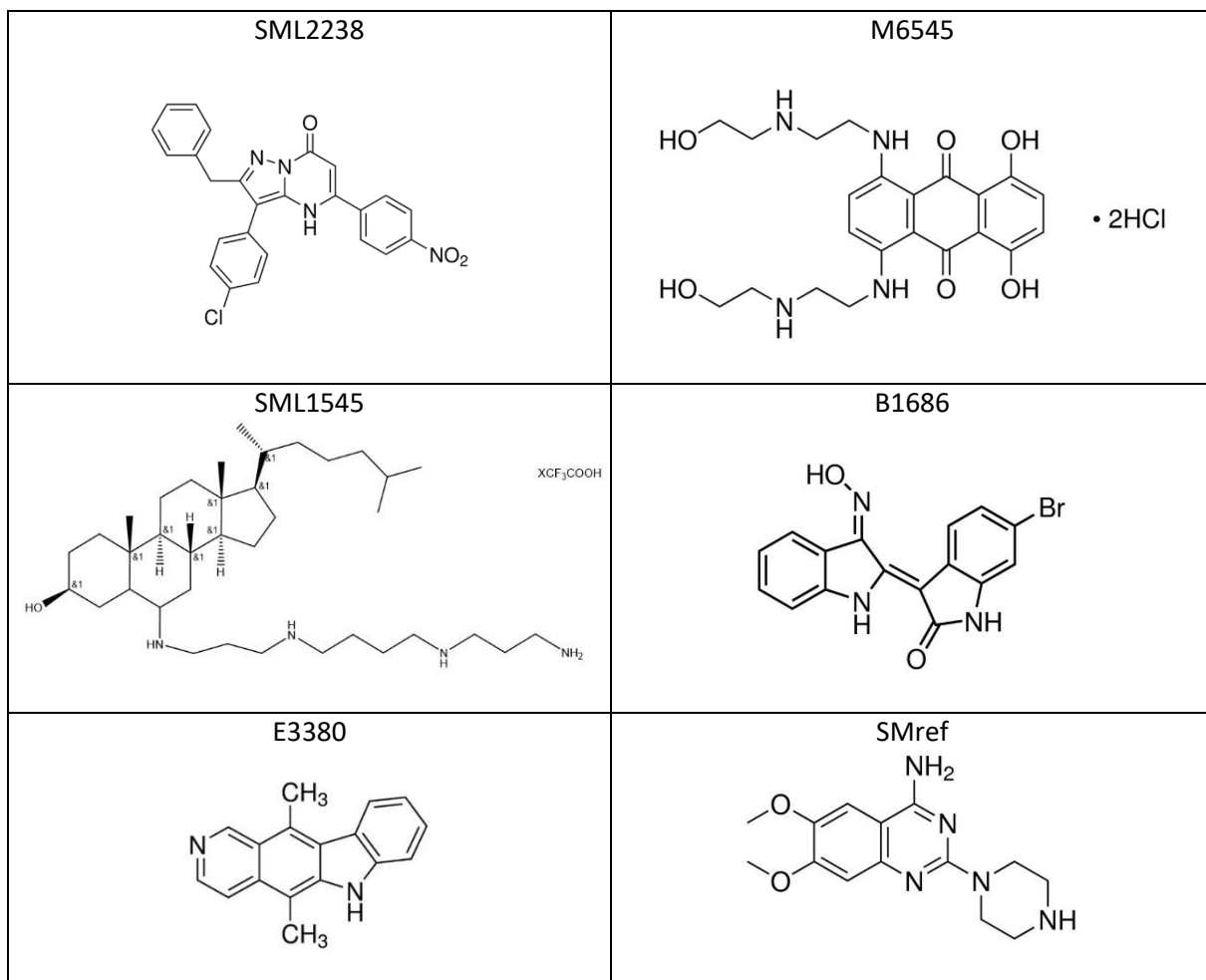
One hundred-twelve compounds were identified as hits after the primary screening. Forty-nine hit compounds were selected from the secondary screening, where 5 bind to 4 RNA motifs, 36 bind to U1 only, 3 bind to 3 RNA motifs, and 5 bind to 2 RNA motifs.

In the last stage, fourteen of the selected compounds were confirmed as decreasing the fluorescent signal (bind to RNA) in a range of concentrations (hits confirmation step). In detail, established SMs (Table 6) were tested in 11 concentrations for IC_{50} determination with all chosen RNA motifs. The IC_{50} values for all SMs and RNA

motifs were determined as described in Methods and Materials (6.2.16 Determination of IC₅₀).

Table 6. SMs selected in Lopac Library HTS for IAV and SARS-CoV-2 RNA motifs.

<p style="text-align: center;">S2671</p>  <p style="text-align: right;">6Na⁺</p>	<p style="text-align: center;">P8293</p> 
<p style="text-align: center;">SML1089</p> 	<p style="text-align: center;">Q3251</p>  <p style="text-align: right;">HCl HCl</p>
<p style="text-align: center;">H9523</p>  <p style="text-align: right;">• HCl</p>	<p style="text-align: center;">M4008</p>  <p style="text-align: right;">• xH₂O</p>
<p style="text-align: center;">B6311</p> 	<p style="text-align: center;">D3768</p>  <p style="text-align: right;">Cl⁻ Cl⁻ • xH₂O</p>



IC₅₀ values were determined for each compound and RNA motif (Table 7).

Table 7. IC₅₀ values for the selected SMs from the Lopac library.

Compound name	IC ₅₀ [μM]			
	M1V	M4	N1	U1
B1686	18.5	-	-	-
D3768	4.1	-	-	-
B6311	12.8	27.9	-	-
H9523	110.5	29.2	-	-
M4008	31.7	26.8	26.8	-
M6545	2.5	1.0	1.0	0.6
P8293	20.6	20.3	-	-

SML1089	20.4	35.0	-	40.5
SML1545	12.6	-	29.2	23.0
SML2238	52.2	-	-	-
Q3251	24.1	-	24.6	-
E3380	27.8	-	48.8	-
S2671	52.2	-	21.2	-
SM _{ref}	60.5	193.7	323.5	281.2

For the M1V motif, all fourteen compounds were qualified as hits – based on the cut-off value set in this experiment. It confirms the binding of particular SM to target RNA (Figure 11). Compounds that appeared in the negative part of the graph during identification were identified as autofluorescent and were rejected in further analyses.

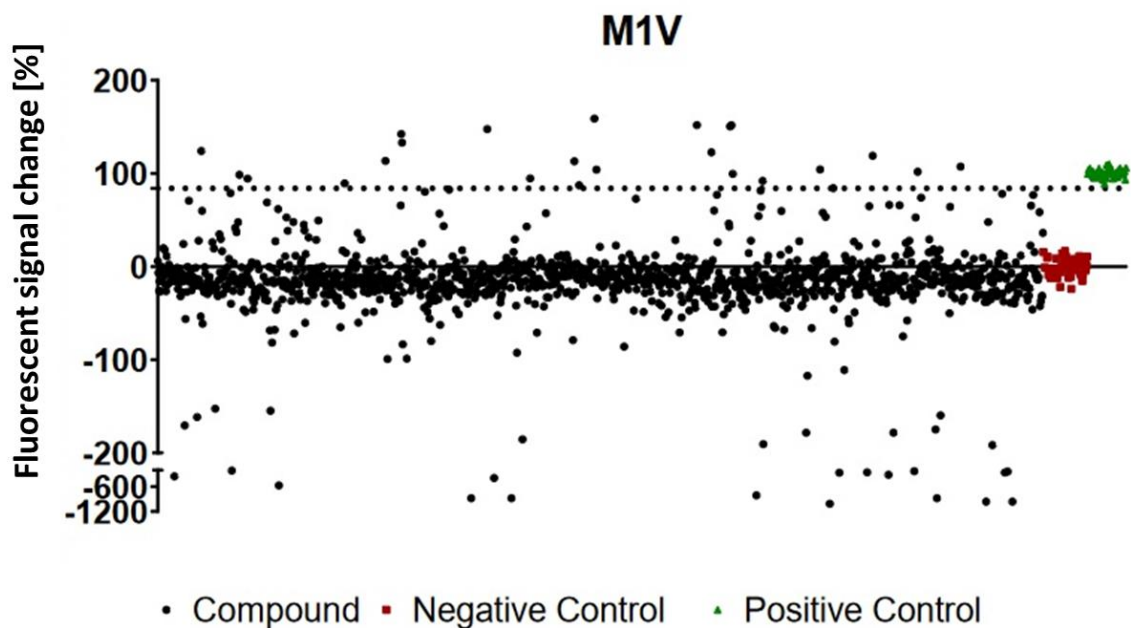
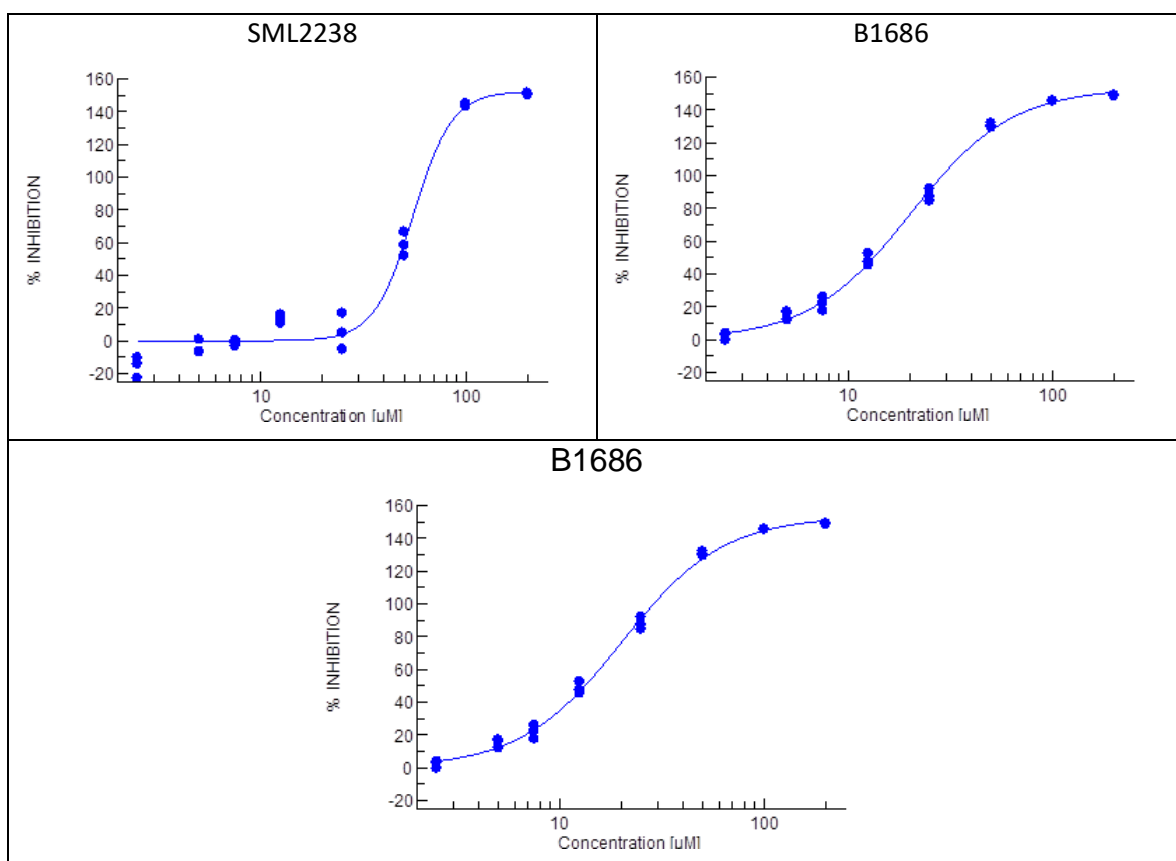


Figure 11. Graphic representation of the primary screening results of Lopac SMs with M1V motif.

Three of the 14 selected compounds were classified as selective ones for the M1V motif, in a sense, bound to only one RNA structural motif in the conducted experiment. The particular compounds are SML2238, B1686, and D3768, with IC_{50} values 52.2 μ M, 18.5 μ M, and 4.1 μ M, respectively (Table 8).

From the determined IC_{50} value for the three mentioned SMs, it can be concluded that the nature of the binding between them and the M1V motif is stronger due to the lower IC_{50} value in relation to the reference compound. It can be concluded that they bind more tightly to the discussed structural motif than SM_{ref} .

Table 8. IC_{50} curves for the most selective Lopac compounds for the M1V motif. The percentage of inhibition in these plots represents the value of the change in the fluorescence signal in FID assay for the mixture of RNA with the compound.



Whereas, for the M4 motif, seven SMs were qualified as binders in the interval between the positive and negative control in the so-called measurement window:

P8293, SML1089, H9523, M4008, B6311, M6545, SM_{ref} (Figure 12) and were selected for the next analysis step.

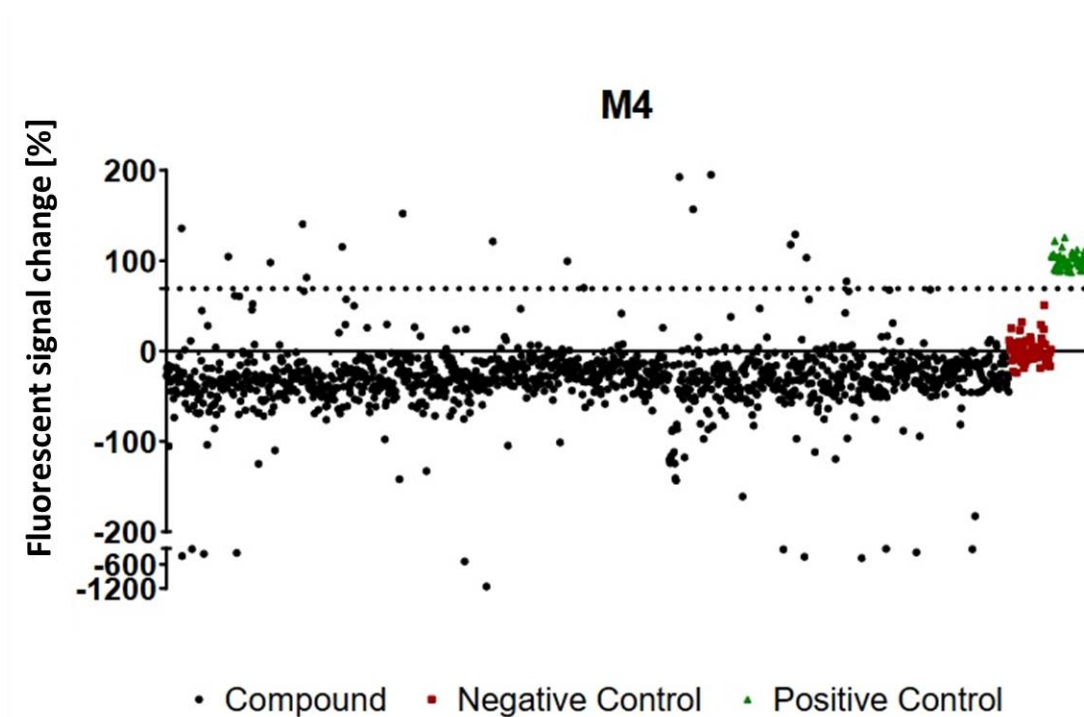
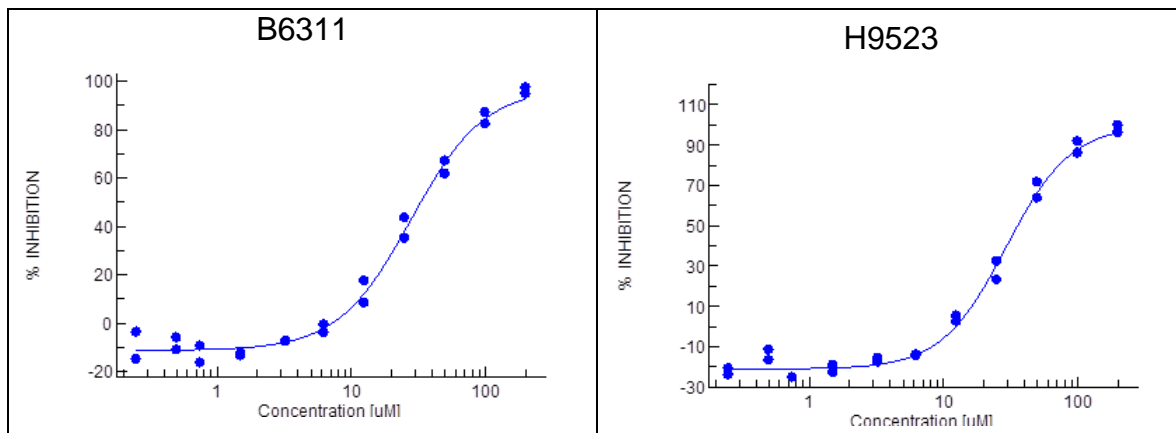


Figure 12. Graphic representation of the primary screening results for Lopac SMs with M4 motif.

The selected compounds were confirmed to be target binders, two of which were selectively bound to the target RNA in this experiment: B6311, and H9523, where IC₅₀ is 27.9 μ M and 29.2 μ M, respectively (Table 9). Both of the binders are characterized by higher binding affinity to the structural motif than the reference molecule, as indicated by their lower IC₅₀ value.

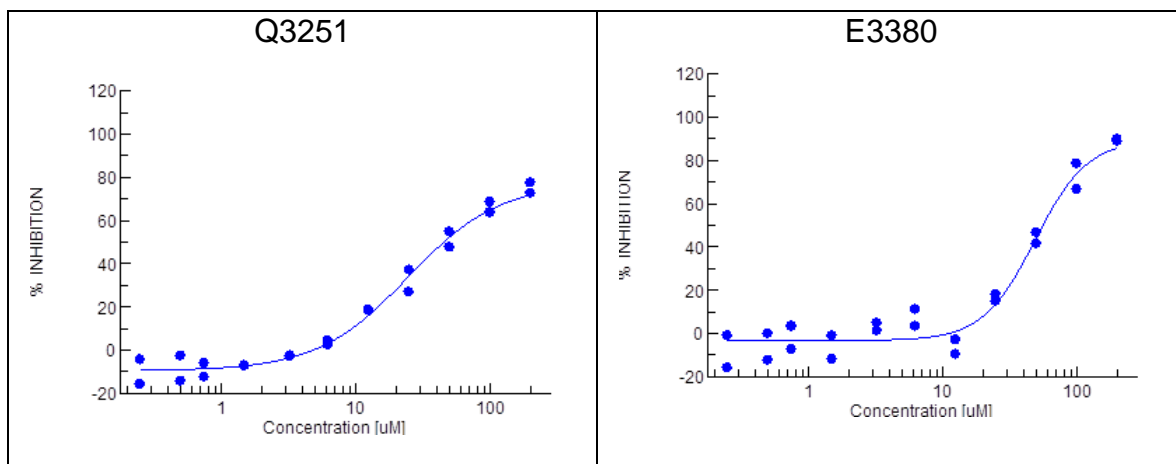
SMs that appeared in the negative part of the graph during identification were identified as autofluorescent and were rejected in further analyses.

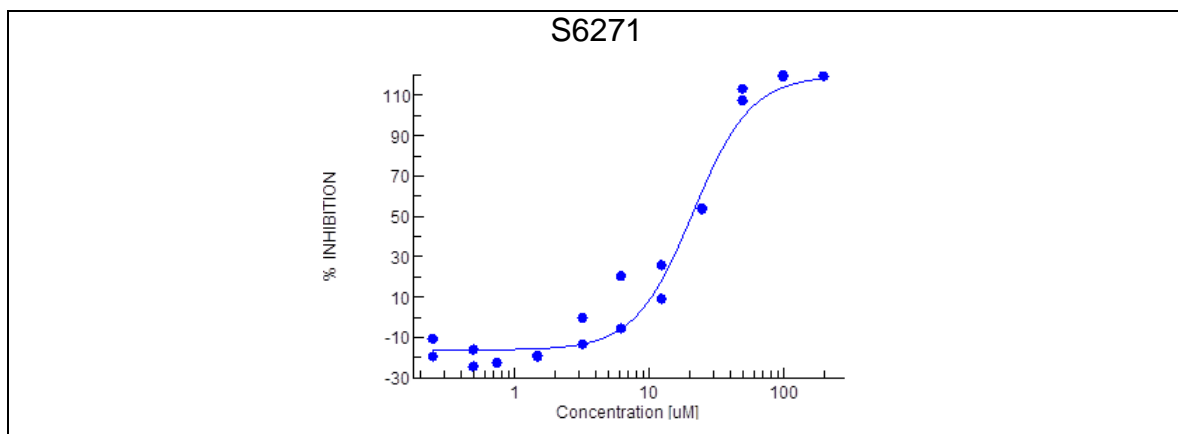
Table 9. IC_{50} curves for the most selective Lopac compounds for the M4 motif. . The percentage of inhibition in these plots represents the value of the change in the fluorescence signal in FID assay for the mixture of RNA with the compound.



Below are the results of HTS for SARS-CoV-2 RNA motifs: the N1 motif, there were 7 hit compounds (S2671, Q3251, M4008, M6545, SML1545, E3380, SM_{ref}), 3 of them were selective, in a sense, bound to only this RNA structural motif in the conducted experiment. The Q3251, E3380, and S2671 were characterized as tightly bound SMs, where IC_{50} is 24.6 µM, 48.8 µM, and 21.2 µM, respectively (Table 10).

Table 10. IC_{50} curves for the most selective Lopac compounds for the N1 motif. The percentage of inhibition in these plots represents the value of the change in the fluorescence signal in FID assay for the mixture of RNA with the compound.





In the case of the U1 motif, there were 4 hits, none of which were selective. This motif's tightly bound compounds are SML1089, M6545, SML1545, and SM_{ref}.

4.2.3. Enamine Library

The second library tested in the FID assay was the Enamine library, which was designed to possess compounds likely to bind RNA. This is a set of 8960 bioactive small molecules, representing the vast majority of the primary target classes.

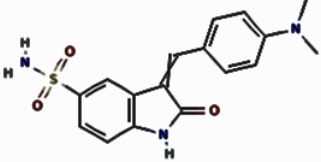
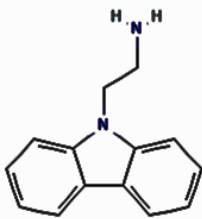
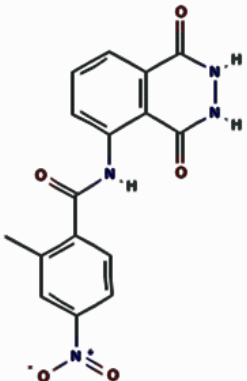
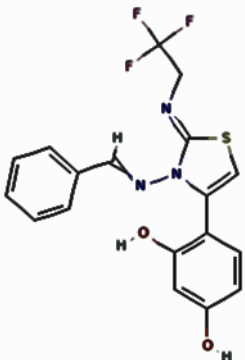
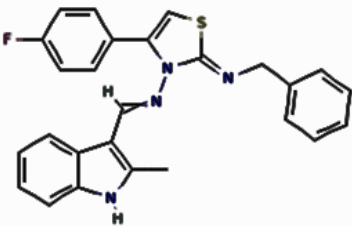
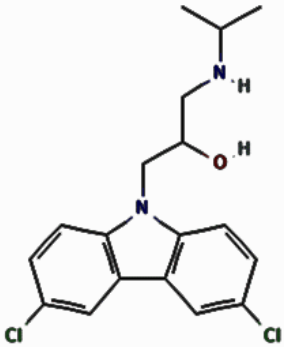
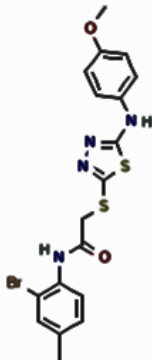
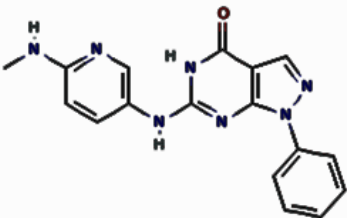
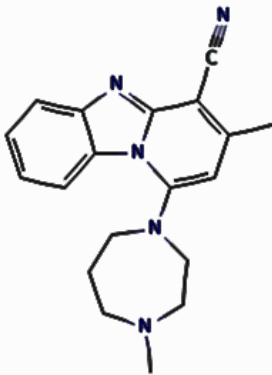
The following RNA structural motifs were used as targets in using this library:

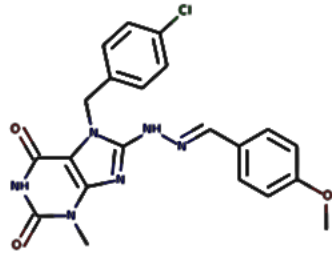
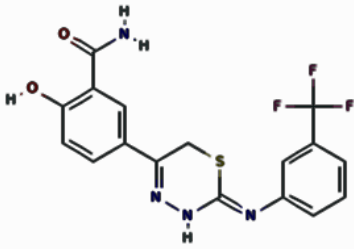
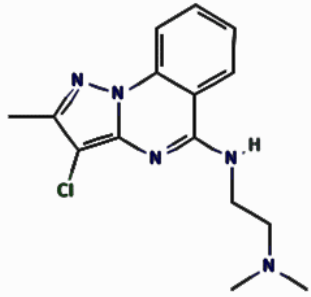
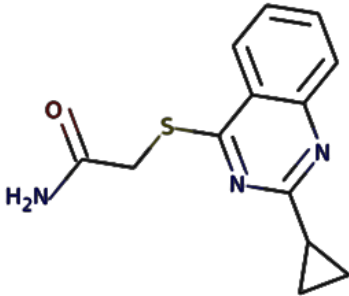
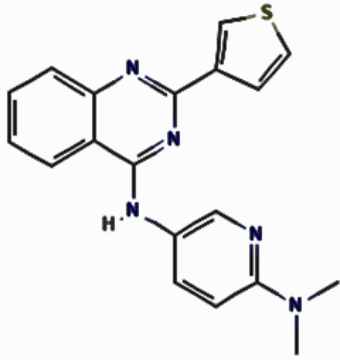
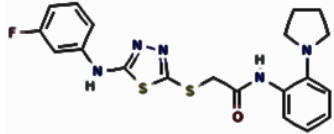
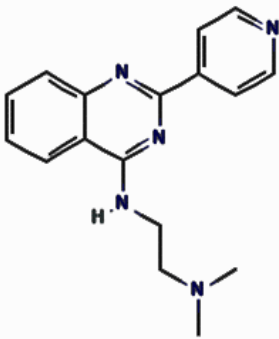
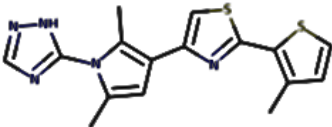
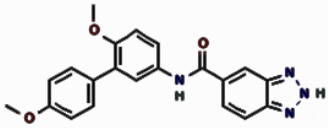
- IAV motifs (Table 2):
 - M1V as a reference motif.
- SARS-CoV-2 motifs (Table 3):
 - U1
 - N1
 - H-M1
 - H-M2
 - H-N1
 - 3U
 - U2.

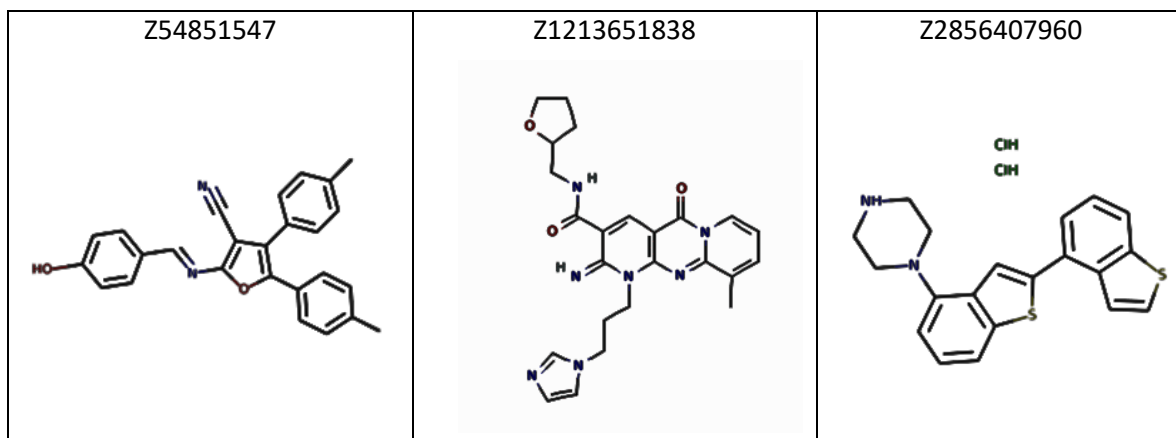
The HTS was performed as described in Methods and Materials (6.2.17 High throughput screening (HTS)). Primary screening was conducted where all RNA motifs were tested against all compounds from the library with additional reference compound SM_{Ref} . Similarly, as for the HTS of the Lopac library, the cut-off value has been established, above which all selected compounds were called hits. The cut-off was calculated based on average plus three standard deviations of the observed fluorescence response for all library compounds.

In primary screening, 647 SMs were selected as hits. Twenty one hit compounds (Table 11) were selected from secondary screening. Selected compounds were confirmed to decrease the fluorescent signal in the hits confirmation step. The IC_{50} values were determined as described in Methods and Materials (6.2.16 Determination of IC_{50}).

Table 11. SMs selected in Enamine Library HTS for IAV and SARS-CoV-2 RNA motifs.

<p>Z650090926</p> 	<p>Z1318256185</p>  <p>Cl-H</p>	<p>Z1175020943</p> 
<p>Z933632926</p> 	<p>Z48626148</p> 	<p>Z56768568</p> 
<p>Z19601649</p> 	<p>Z1272208728</p> 	<p>Z223816872</p> 

<p>Z281877654</p> 	<p>Z134817028</p> 	<p>Z165209348</p> 
<p>Z215664726</p> 	<p>Z238682876</p> 	<p>Z154467994</p> 
<p>Z239612492</p> 	<p>Z355285978</p> 	<p>Z202047774</p> 



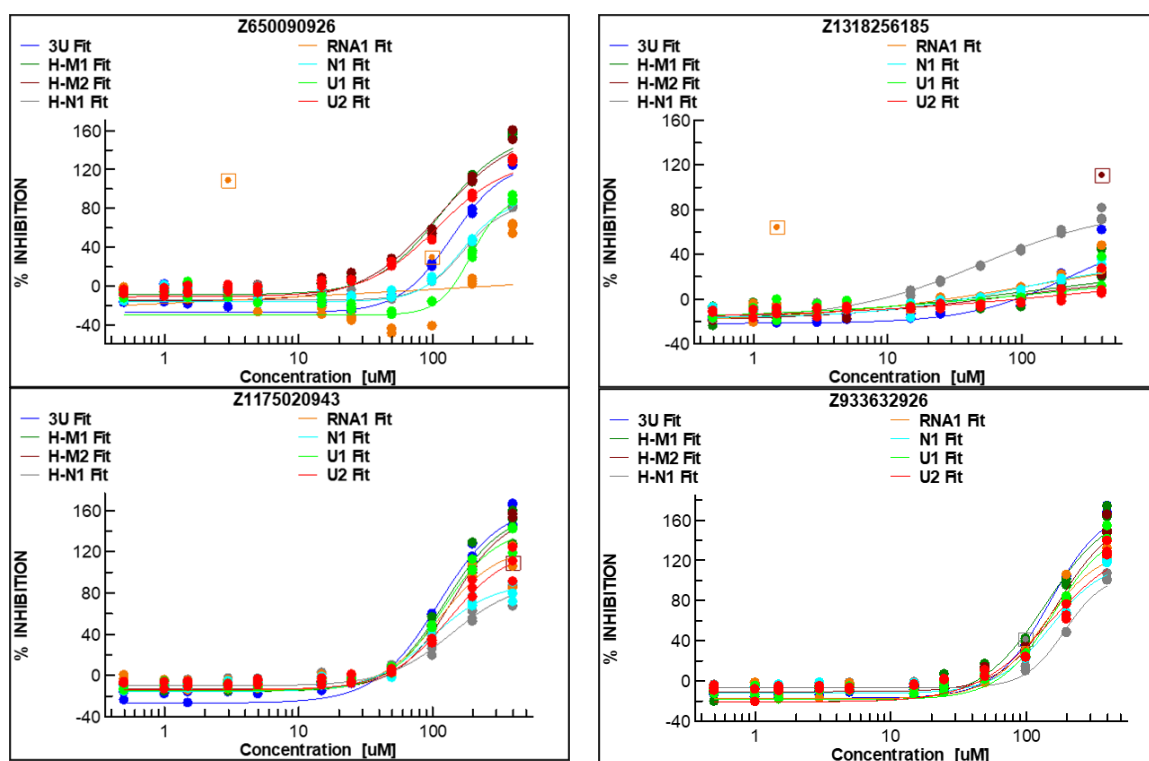
IC₅₀ values were determined for each compound and RNA motif (Table 12). The H-N1 motif is characterized by the highest number of SM binders (10 ligands were selected as decreasing fluorescence signal).

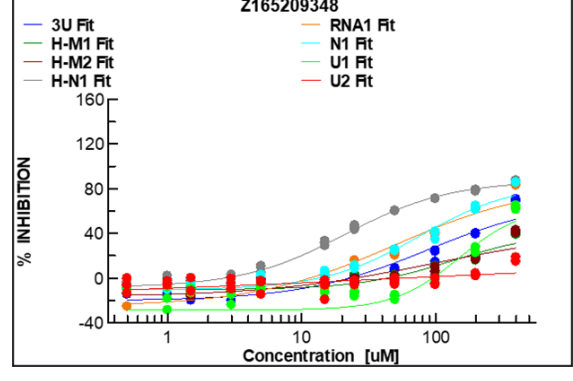
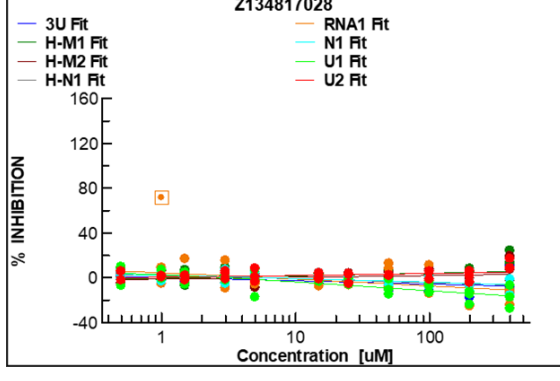
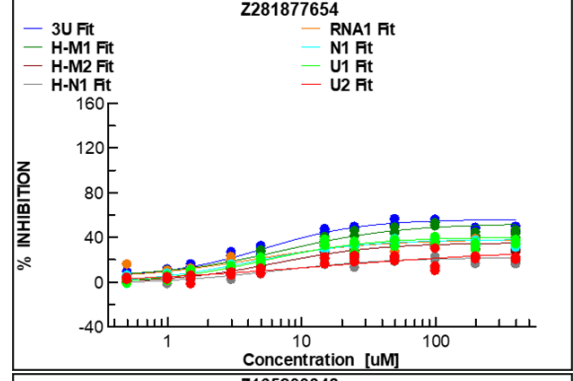
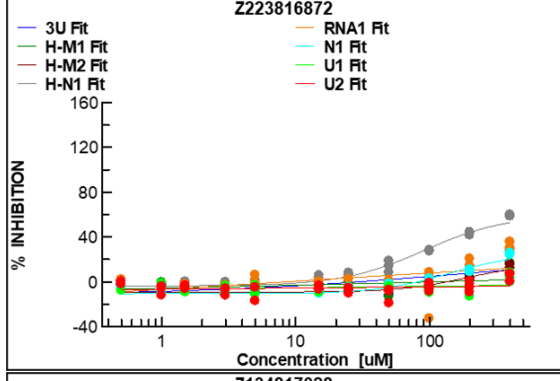
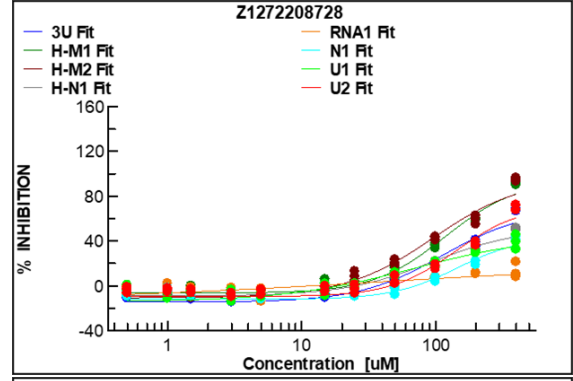
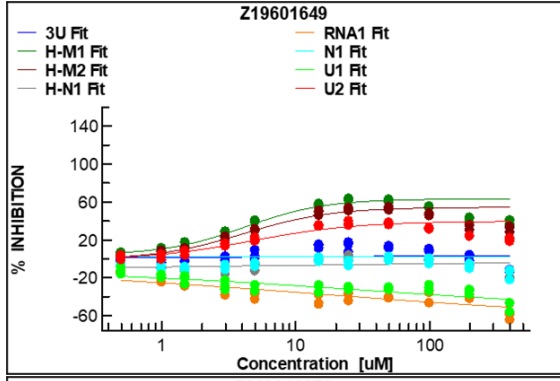
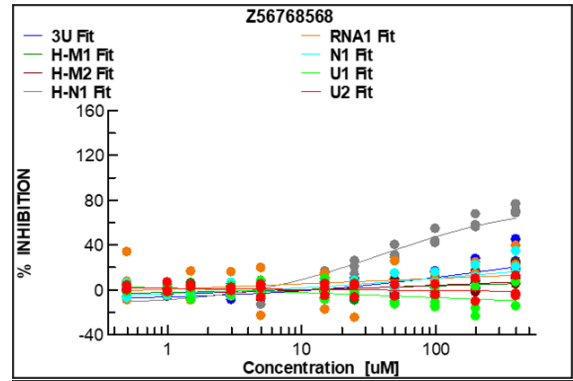
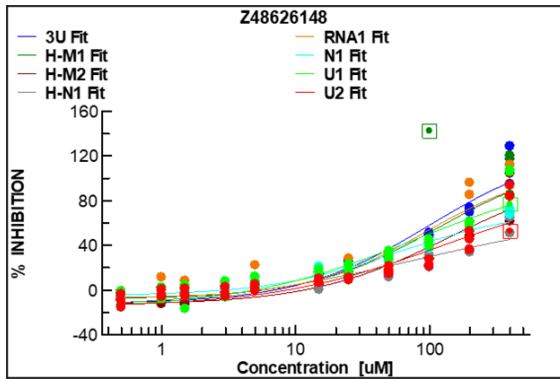
Table 12. IC₅₀ values for Enamine hits.

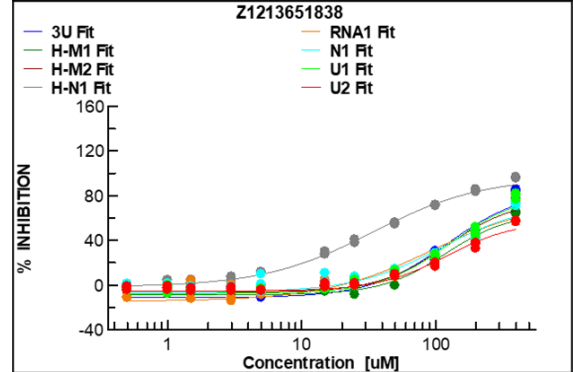
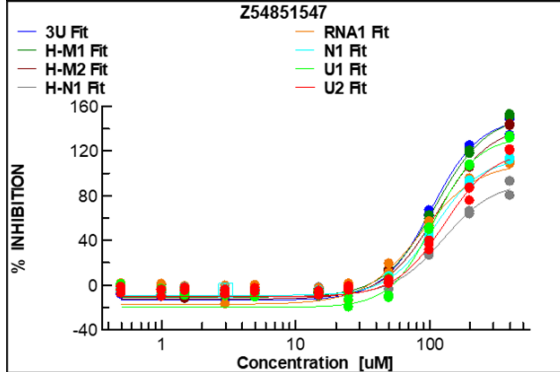
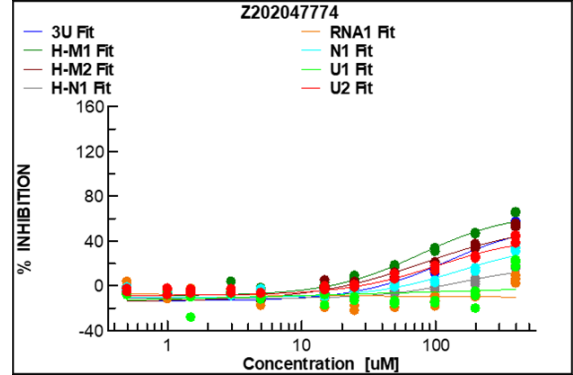
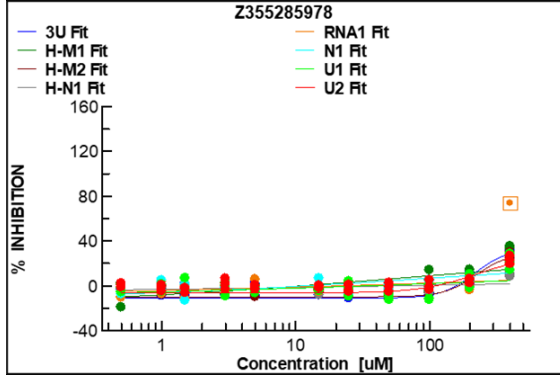
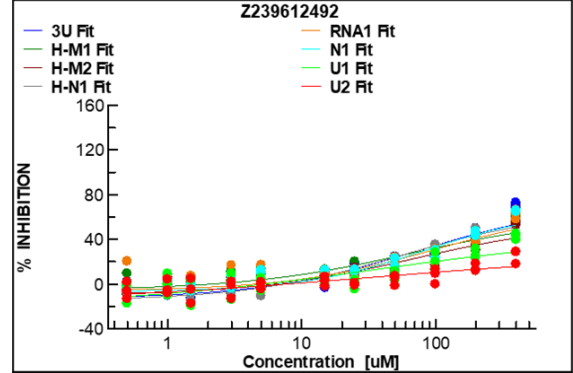
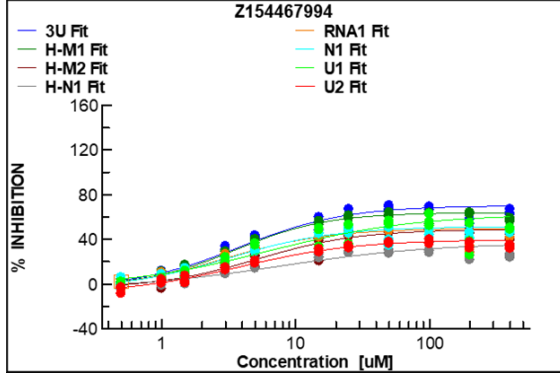
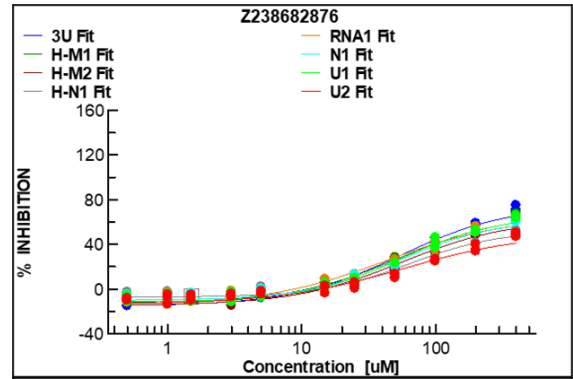
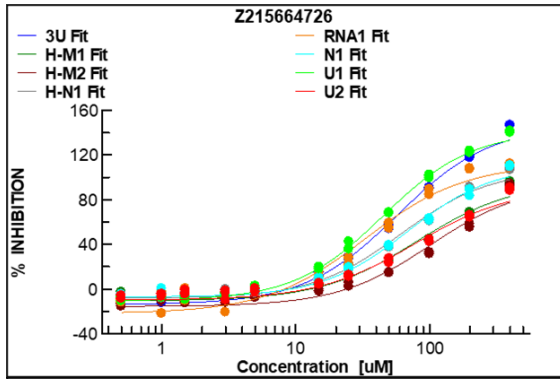
Compound name	IC ₅₀ [μM]							
	3U	H-M1	H-M2	H-N1	N1	M1V	U1	U2
Z650090926	-	-	110.9	-	-	-	-	-
Z1318256185	-	-	-	50.5	-	34.0	-	-
Z1175020943	110.6	-	-	-	-	-	-	-
Z933632926	-	-	171.6	-	-	-	-	-
Z48626148	-	-	-	-	56.8	-	-	-
Z56768568	-	-	-	39.4	-	-	-	-
Z19601649	-	-	4.2	-	-	-	-	-
Z1272208728	-	118.4	96.0	-	-	-	69.5	-
Z223816872	-	-	-	90.9	-	-	-	-
Z281877654	5.3	-	-	-	-	4.4	-	-
Z134817028	-	118.4	96.0	63.7	-	-	-	-
Z165209348	-	-	-	21.4	-	-	-	-
Z215664726	-	-	-	61.2	-	-	45.0	-
Z238682876	-	-	56.1	-	-	-	-	-
Z154467994	3.8	-	-	-	-	-	-	-
Z239612492	-	-	-	55.3	-	-	-	-
Z355285978	-	-	224.0	-	-	-	-	-
Z202047774	-	-	82.3	-	-	-	-	-
Z54851547	-	-	-	126.9	-	-	-	-
Z1213651838	-	-	-	34.0	-	-	-	-
Z2856407960	-	-	-	168.1	-	-	-	-

Eight ligands were identified as specific for the H-M2 motif as a target, 6 of selected SMs, i.e., Z650090926, Z933632926, Z19601649, Z238682876, Z355285978, Z202047774 were selective, in a sense, bound to only one vRNA structural motif in the conducted experiment. The H-M1 motif was confirmed to bind to two SMs: Z1272208728 and Z134817028. None of these SMs were selective. The decrease of fluorescence signal using compounds Z1175020943, Z281877654, and Z154467994 was significant for the 3U motif. The Z1318256185 and Z281877654 decreased the fluorescence signal in the case of the M1V motif. At the same time, the U1 motifs binders were Z1272208728 and Z215664726. The compound known as Z48626148 bound selectively to the N1 structural motif. Interestingly, no compounds were identified for the U2 motif in the tested concentration range.

IC₅₀ curves for all selected compounds with tested RNA targets are collected in the graphs below (Figure 13).







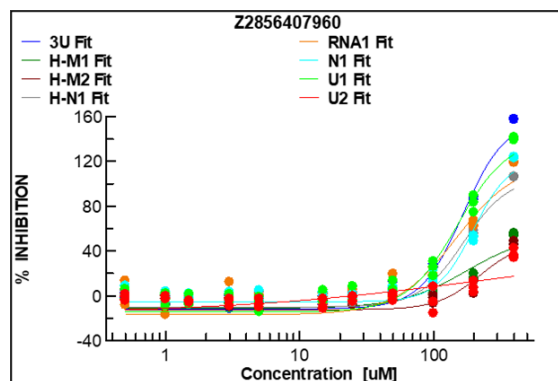


Figure 13 IC_{50} curves for selected SMs targeting RNA motifs. The data was processed with the Office Professional package using the Excel Professional software. The percentage of inhibition in these plots represents the value of the change in the fluorescence signal in the FID assay for the mixture of RNA with the compound. The M1V curve is named here as RNA1.

Results show that adapted and improved FID assay allowed to distinguish the reasonable number of small molecules that bind to conserved RNA motifs of IAV and SARS-CoV-2. The number of found hits is 1.10% for Lopac library screening for 4 targets, while 0.24% for Enamine library screening for 8 targets, on average. Hit rates in the presented analysis are up to 2%, which is defined in the literature as correct for HTS experiments [103].

Applied in this research, FID assay has advantages, such as not complicated protocol, allowance to use not changed, unlabeled RNA, and relatively short running time of the experiment. There are also disadvantages, such as limitations in chosen targets and difficulty finding positive control for new RNA, which affects the test quality and sometimes the assay's feasibility. Also, only small molecules that displace fluorescent indicators will be detected and which do not impair indicator fluorescence. All selected from HTS small molecules need to be validated in terms of their needed properties in followed-up methods.

Later in this research, the selected compounds from Lopac and Enamine libraries were molecularly docked to check the interaction between the targeted RNA and the selected ligand (4.4 Binding affinity of selected SMs). Also, the inhibitory properties of described SMs were evaluated against IAV, strain A/California/04/2009 (H1N1) in

MDCK cells (4.5.1 Inhibitory potential of selected Lopac library compounds; 4.5.2 Inhibitory potential of selected Enamine library compounds).

Interestingly, the M6545 compound presents very low IC_{50} values for every RNA target in the FID assay. Moreover, it binds to each of the tested structural motifs, so it can be concluded that the SM can interact easily and non-specifically with RNA motifs. This fact can be considered an advantage of the M6545 because it could be used as a good positive control in testing new RNA structural motifs in the new FID assay preparation for HTS of small molecules library.

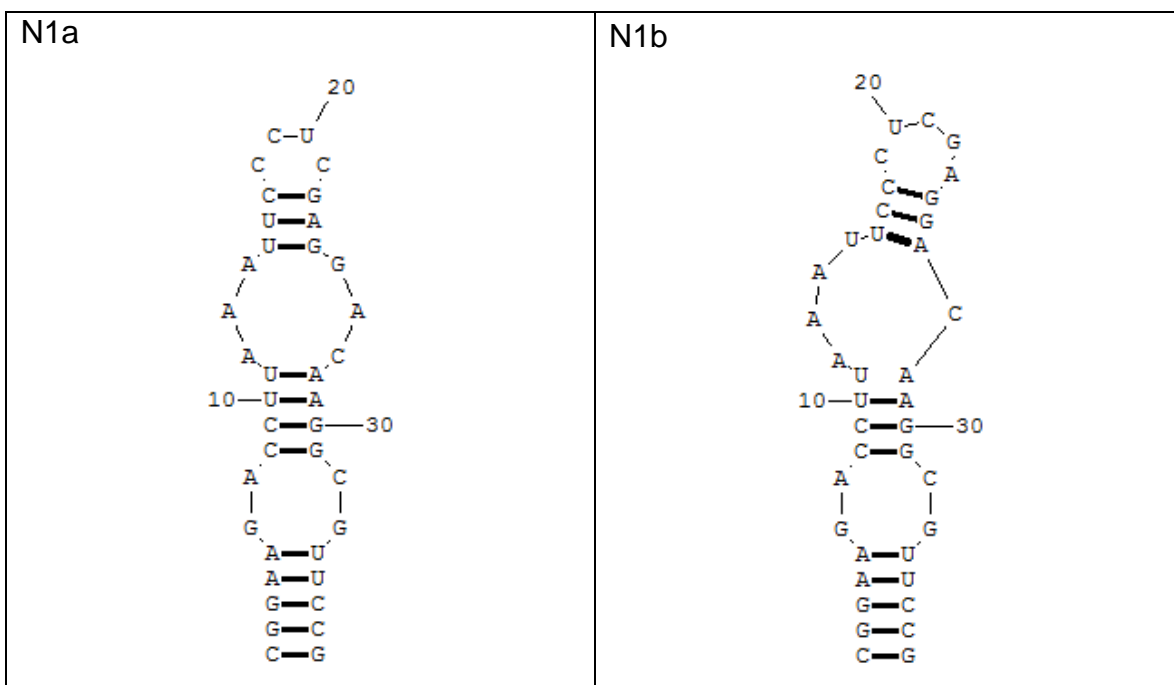
4.3. Characterization of the tertiary structure of selected RNA structural motifs generated in Molecular Dynamic Simulations.

The Molecular Dynamics Simulation (MDS) consists of the numerical, step-by-step solution of the classical equations of motion. Computer simulations are carried out to understand the properties of molecules' assemblies in terms of their structure and interactions. It should not be forgotten that it is still a prediction of structure behavior, not a conventional experiment. Therefore, to increase the credibility of the obtained data, the results of such activities should be confirmed in a traditional experiment. MDS enables researchers to learn something new that cannot be found in other ways. MDS aims to reduce the amount of fitting and guesswork in the conducted experiment to a minimum.

The presented data was created in cooperation with the Biomolecular Machines Laboratory (Prof. Joanna Trylska), Centre of New Technology, University of Warsaw, during the internship of the author of this dissertation.

Secondary structures of selected motifs were well known and understood in terms of thermodynamics. The molecular dynamic simulation was conducted to obtain the 3D structure of chosen vRNA of SARS-CoV-2 for molecular docking. During the internship it was possible to simulate U1, N1, H-M1, H-M2, H-N1, 3U and 3U motifs (Table 3). In the case of the N1 motif, two structures were considered – N1a and N1b (Table 13). N1a has been bioinformatically predicted to be more thermodynamically stable, and N1b is an *in vitro* and *in cellulo* proven motif [92]. The simulations for mentioned motifs have been extended concerning the rest of the structural motifs to 1000 ns. The remaining experiments were run for 100 ns, except for the simulation for the U1 motif, for which the simulation took 500 ns due to the length of the RNA. The MDS was performed as described in Methods and Materials (6.2.18 Molecular dynamics).

Table 13. Secondary structures of N1a and N1b motifs.



A series of analyzes for each of the structures were performed. The root-mean-square deviation (RMSD) was analyzed (Table 14). The RMSD is a simple way of summarizing the quality of the tertiary structure model at the level of its overall fold. It is a widely used quantitative measure of the similarity between two superimposed atomic coordinates.

$$RMSD = \sqrt{\sum_{i=1}^y e_i^2 \frac{1}{x}}$$

Where the averaging is performed over the x pairs of equivalent atoms, and e_i is the distance between the two atoms in the i -th pair [104].

RMSD values are presented and calculated in Å. It can be understood as an agreement between predicted and accepted RNA structures over a representative set of atoms. The significant value of the RMSD parameter is the possibility of using the estimated quality for both simplified and all-atom models [105], [106].

Presented values of RMSD are analyzed for each production of MDS distinctly in VMD software [107]. The RMSD values for selected motifs ranged from 2.5 Å to 6.5 Å. These values testify to the high quality of the simulation (Table 15).

Table 14. RMSD results for each production of MDS of selected structural motifs.

RMSD parameters from VMD [Å]						
RNA	Prod	Avg	SD	min	max	num
3U	Prod 1	3.588	0.787	0	6.371	20000
	Prod 2	3.602	1.245	1.318	7.579	20000
	Prod 3	3.156	0.509	1.682	5.256	20000
H-M1	Prod 1	6.492	0.970	2.714	9.599	20000
	Prod 2	4.933	1.032	2.128	10.794	20000
	Prod 3	5.929	1.395	2.200	9.272	20000
H-M2	Prod 1	3.718	0.317	2.784	5.275	20000
	Prod 2	3.851	0.317	3.069	5.945	20000
	Prod 3	3.585	0.3066	2.778	5.016	20000
H-N1	Prod 1	2.557	0.406	1.490	4.304	20000
	Prod 2	2.807	0.399	1.724	4.344	20000
	Prod 3	2.800	0.577	1.643	4.962	20000
N1a	Prod 1	3.737	0.521	2.463	5.860	20000
	Prod 2	4.511	0.506	2.847	6.635	20000
	Prod 3	4.229	0.524	3.023	7.011	20000
N1b	Prod 1	4.838	0.734	2.690	7.175	20000
	Prod 2	4.865	0.827	2.355	7.934	20000
	Prod 3	5.062	0.751	2.921	7.685	20000
U1	Prod 1	3.231	0.737	1.651	6.418	20000
	Prod 2	3.909	1.146	1.138	8.401	20000
	Prod 3	3.287	0.771	1.255	6.605	20000
U2	Prod 1	4.696	0.681	2.839	6.975	20000
	Prod 2	4.606	0.781	2.172	8.642	20000
	Prod 3	4.444	0.672	2.532	6.964	20000

In order to compare the stability of the N1a/b structures during the MDS, the Root-Mean-Square-Fluctuations (RMSF) were performed. It measures the displacement of a particular atom, or group of atoms, relative to the reference structure, averaged over the number of atoms [108], [109].

The fluctuations of mentioned motifs are presented in the diagrams (Figure 14, Figure 15). Based on the analyzed data, it can be concluded that both predictions of

the structure of the N1 (Table 13) motifs are characterized by similar stability in the simulated molecular dynamics system. Moreover, it means that both the N1a and N1b structural motifs are characterized by similar thermodynamic stability, and both types of motif have an equal probability of occurrence. What is more, based on the presented fluctuation analysis, it can be concluded that there is a higher mobility within the terminal helix during the MDS. Such fluctuations are noticeable in both N1a and N1b.

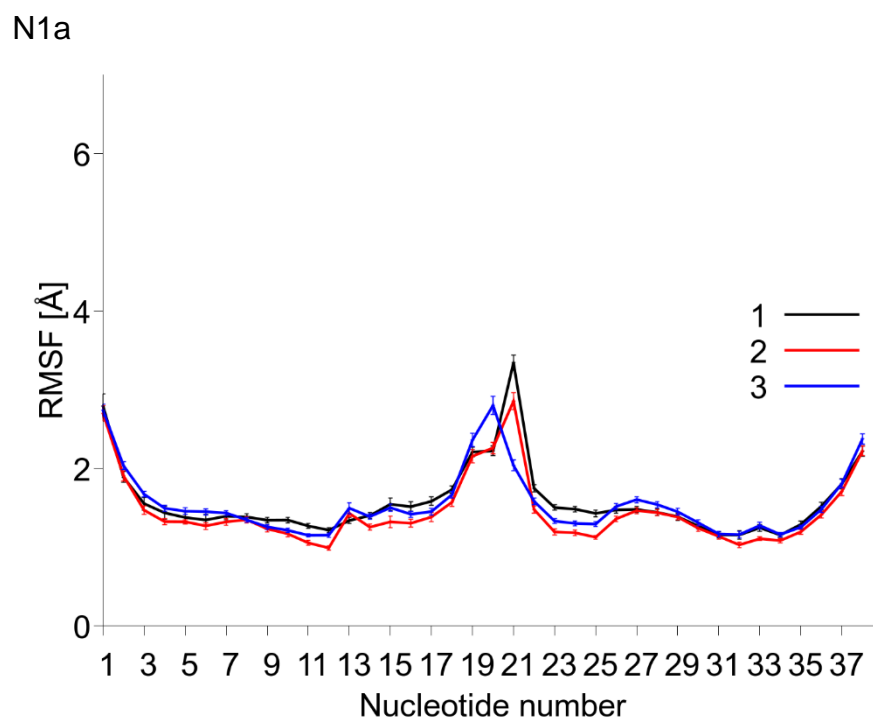


Figure 14. Fluctuation of N1a simulated structure. The black line represents the first production, the red one is for the second, and the blue line represents the third production.

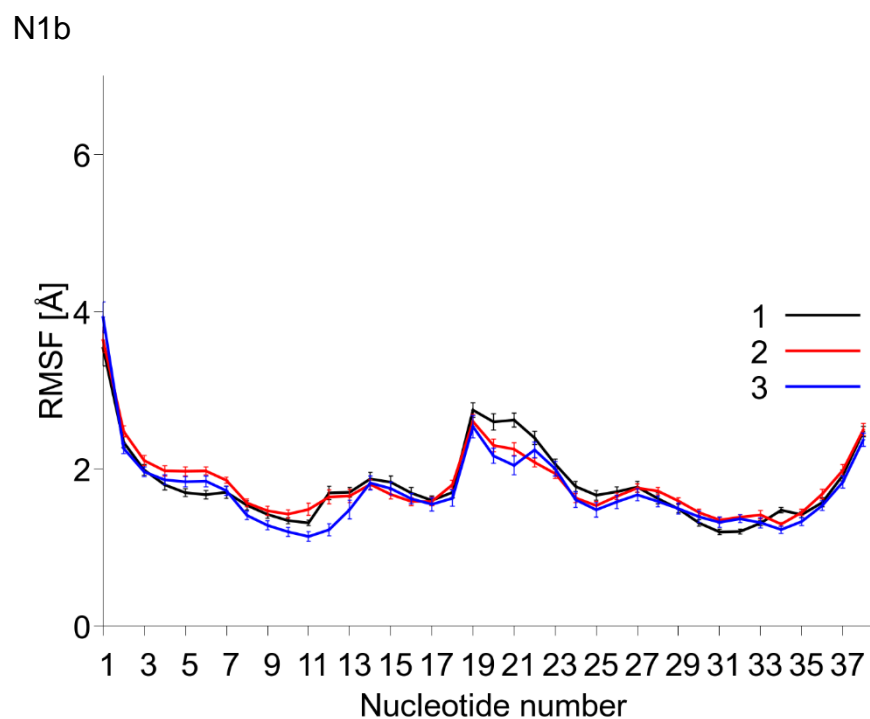


Figure 15. Fluctuation of N1b simulated structure. The black line represents the first production, the red one is for the second, and the blue represents the third production.

Clustering is the further step after the MDS to select representative structures for molecular docking. This process is a common analysis that allows grouping together similar conformations of the simulated structures [110]. The k-means algorithm was used in the case of structural motifs simulated for this dissertation.

K-means is one of the simplest and most popular clustering algorithms available. This works by first randomly seeding the centroids of k clusters, where k is the desired cluster count. In the case of this research, it is 5. The assigning of each data point to the group which centroid is nearest to it. The centroid of each cluster is nextly recalculated. This process continues until there are no changes when recalculating the centroids [110], [111].

The clustering was performed as described in Methods and Materials (6.2.19 Simulated RNA structure clustering). During the analysis, 5 frames from the simulation were selected (Table 15), where % of the frame means its repeatability in

the entire simulation system. The frames are ranked based on decreasing frequency of occurrence in the layout. The metrics of clustering quality are the Davies–Bouldin index (DBI) and the pseudo-F-statistic (pSF) [112]. DBI is calculated as the average similarity of each cluster with a cluster most similar to it [113]. This is based on the approximate estimation of the distances between clusters and their dispersions to obtain a final value that represents the quality of the partition [114]. The pSF is based on a comparison of intracluster variance to the residual variance over all points. This is determined from the classical regression model coefficients of the sum of regression (SSR) and the sum of the square errors (SSE):

$$pSF = \frac{\frac{SSR}{q} - 1}{SSE/(n - g)}$$

Where n represents all points and g represents all clusters [115]. Due to the research experience, using both metrics in conjunction appears to be a promising way to assess clustering quality.

An excellent clustering is characterized by low DBI values and high pSF values. According to the presented data (Table 15), the clustering occurred correctly for the simulated motifs. Individual frames were, after appropriate preparation, used as a receptor in molecular docking.

Table 15. Values of DBI, pSF, and frames for clustered motifs of simulated vRNA structures.

RNA	Cluster No	Frames		DBI	pSF
H-M1	0	17255	28.8%	1.954825	13979.40582
	1	16090	26.8%		
	2	11199	18.7%		
	3	7739	12.9%		
	4	7717	12.9%		
U1	0	15936	26.6%	1.959684	8312.359794
	1	14680	24.5%		
	2	13846	23.1%		
	3	9046	15.1%		
	4	6492	10.8%		
H-M2	0	21986	36.6%	2.221729	40022.09367
	1	15620	26.0%		
	2	12133	20.2%		

	3	5994	10.0%		
	4	4267	7.1%		
U2	0	14408	24.0%	2.253157	7364.887826
	1	11932	19.9%		
	2	11474	19.1%		
	3	11323	18.9%		
	4	10863	18.1%		
N1a	0	17364	28.9%	1.784151	13441.91862
	1	13654	22.8%		
	2	10611	17.7%		
	3	10080	16.8%		
	4	8291	13.8%		
N1b	0	16415	27.4%	2.186444	6962.976803
	1	15163	25.3%		
	2	11735	19.6%		
	3	10491	17.5%		
	4	6196	10.3%		
3U	0	14002	24.2%	1.702384	12587.93798
	1	12996	22.5%		
	2	12916	22.3%		
	3	11076	19.1%		
	4	6887	11.9%		
H-N1	0	14577	25.6%	2.069828	6538.420158
	1	13356	23.5%		
	2	11802	20.7%		
	3	8607	15.1%		
	4	8552	15.0%		

The next planned step is to perform a molecular dynamics simulation and clustering of the prepared system for the M4 motif. Thanks to this, it will be possible to carry out molecular docking to the M4 motif for compounds found in the HTS of two examined libraries.

4.4. The binding affinity of selected SMs

Molecular docking (MD) is a computer simulation tool carried out to investigate and interpret the interactions between the target molecule (receptor) and ligand. As a receptor, in the case of this dissertation, various RNA motifs of IAV and SARS-CoV-2 were used, and as a ligand, the selected SMs from Lopac or Enamine library were used. MD software predicts the SM affinity to the RNA motif and its binding site, including interactions in the complex. The AutoDock Vina 1.1.2 software [116]–[118] was used as a docking tool. The program is designed to predict the binding of SM to targeted receptors 3D structures. To analyze the data, i.g. interactions between the target molecule and SM, hydrogen bonds, and distances, the AutoDock Tools 1.5.6 [116]–[118], the UCSF Chimera 1.14 [119] and the Maestro 12.5 [120] were used. The MDs were performed as described in Methods and Materials (6.2.20 Molecular docking).

4.4.1. Characterization of the binding with the selected Lopac SMs

The small molecules selected in the high throughput screening of the Lopac library were docked to molecular targets, which structures are available (M1V, NMR structure; Table 2) or were generated by molecular dynamics (U1, N1a, and N1b; Table 3). The criteria for choosing the SMs for docking was usually selectivity of compounds, understanding as binding to one RNA motif of the virus, from tested motifs or/and low IC₅₀.

The first presented molecular docking is the M1V with 3 selected hits from the Lopac library: SML2238, D3768, and B1686 (Figure 16). The interaction between the RNA motif and ligands were investigated, and it has been found that a hydrogen bond between the M1V motif and B1686 occurred between ligands oxygen of the OH group and H62 from the A5. The bond has the following length: 1.972 Å. One H-bond was detected in SML2238 docking: nitrogen of the aromatic ring of the SM interacts with H42 of the A25 (2.107 Å). The D3768 is characterized by three H-bonds detected:

- Between N7 of A7 and H of the ligand NH group (2.760 Å),
- Between O4 of U26 and H of the ligand NH₂ group (2.329 Å),
- Between O4 of U27 and H of the ligand NH₂ group (1.953 Å);

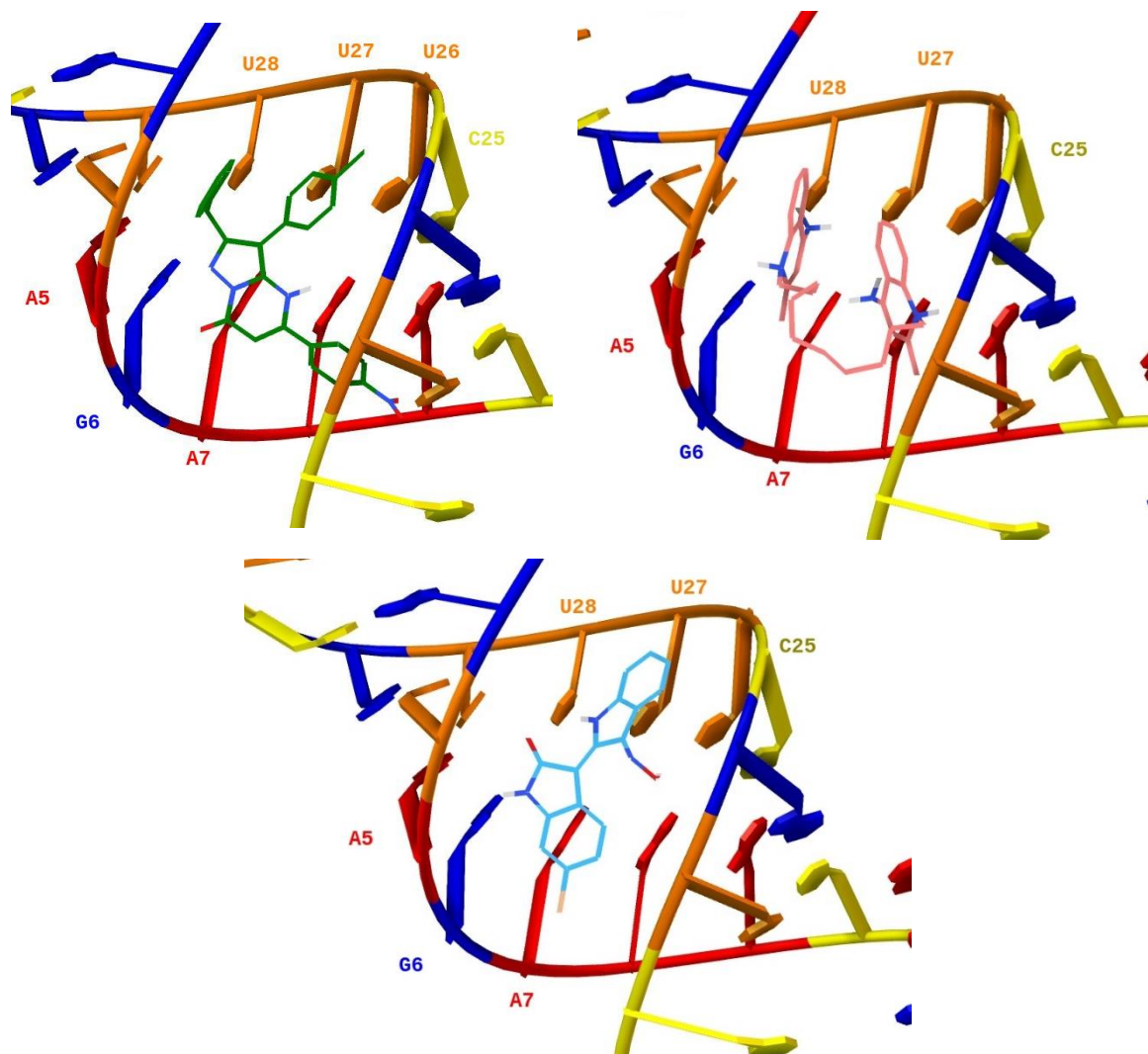


Figure 16. Molecular docking of the specific Lopac SMs for M1V motif. The colors of the ligands are the following: SML2238 (green), D3768 (light pink), B1668 (baby blue), and for residues: U (orange), G (blue), A (red), and C (yellow). The presented figures were prepared in AutoDockTools 1.1.2.

The binding affinity of the selected SMs to the M1V motif were analyzed for all 9 docking scores of each molecular experiment (Figure 17). The level of free energy (ΔG) indicates that the described experiment ran well and with high efficiency. The

values of the individual molecular docking are the following: SML2238 (-8.425 kcal/mol), B1689 (-7.550 kcal/mol), and D3768 (-4.565 kcal/mol).

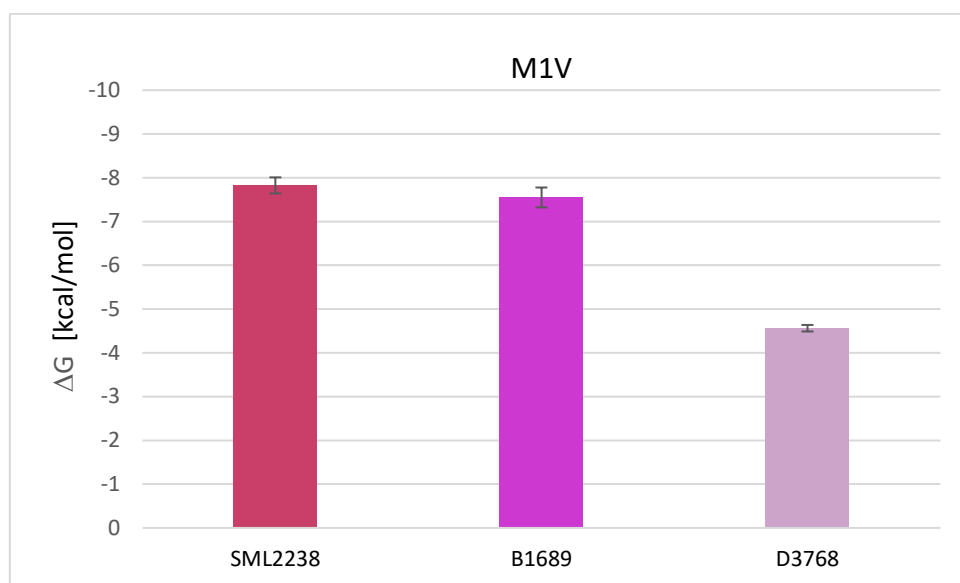


Figure 17. The binding affinity of specific Lopac SMs for the M1V motif measured in ΔG of the complex.

Nextly, the clusters of N1 were undergone MD. The molecular dynamics simulation experiment and the analysis of the results show that the presence of both forms N1a and N1b is comparably probable. Therefore, both versions of the N1 structural motif were used in the molecular docking experiment.

The N1 motifs were docked with three selected ligands from the Lopac library: E3380, Q3251, and S2671 (Figure 18). The presented molecular docking was performed with cluster 1 of the N1a motif for each SM. The interaction between ligands and the tested motif was analyzed. Two hydrogen bonds have been detected between Q3251 and N1a motif: O of the SM OMe group and H21 and H3 of the G28484. The length of the mentioned H-bonds is following: 2.442 Å and 2.299 Å. The E3380 ligand is characterized by one H-bond with the N1a motif: H62 of the A28462 with N from the ligands` aromatic ring (2.286 Å). One hydrogen bond was identified between O of the SO₃ from the S2671 and H62 of the A28462 (2.054 Å).

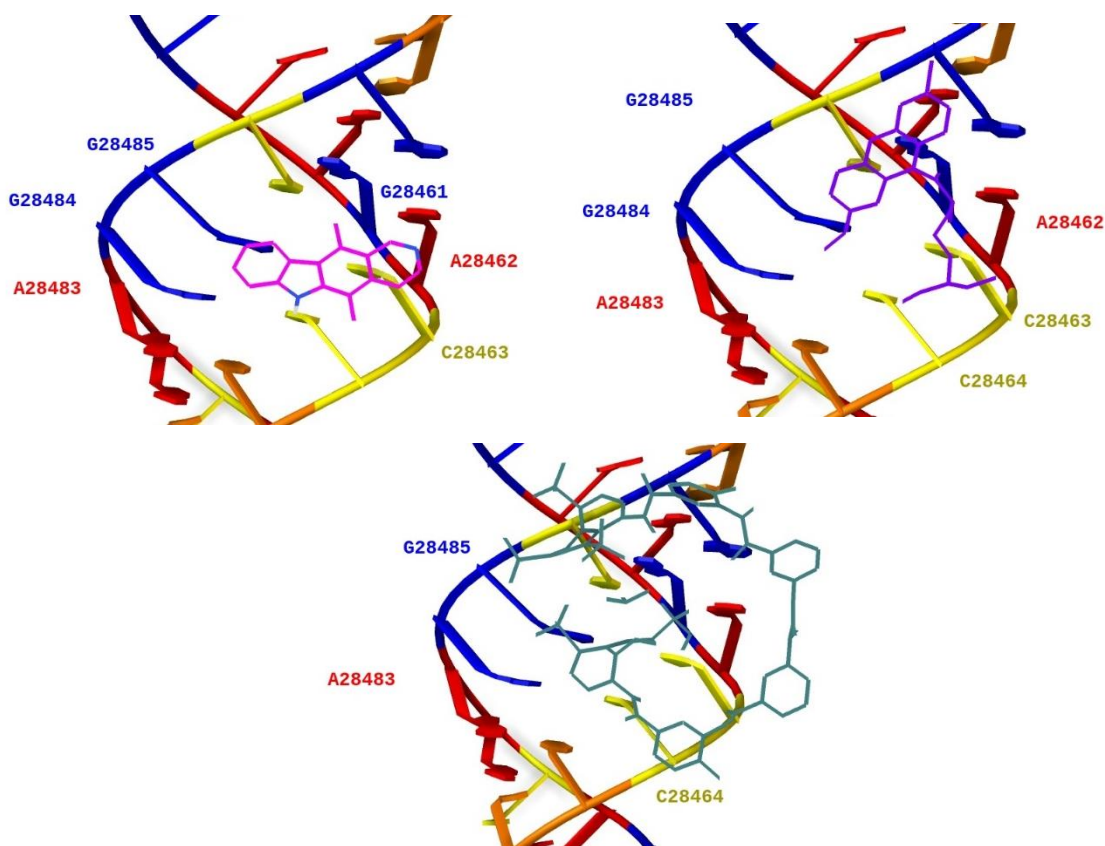


Figure 18. Molecular docking of the specific Lopac SMs for N1a motif. The colors of the ligands are following: E3380 (pink), Q3251 (purple), S2671 (emerald), and for residues: U (orange), G (blue), A (red), and C (yellow). The presented figures were prepared in AutoDockTools 1.1.2.

Even though the S2671 ligand is relatively long and its molecular docking is partly in the structure of the target motif and partly next to it, one hydrogen bond was found. The bond between SM oxygen and the donor is from A28462 of the N1a structural motif.

The selected SMs and N1a motif binding affinity were analyzed for all 5 clusters and 9 docking scores of each molecular experiment (Figure 19). The free energy (ΔG) value indicates that the mentioned experiment ran profitably and efficiently in each case. The values of the individual molecular docking listed in order from the first to the fifth cluster are as follows: E3380 (-5.345; -5.767; -4.812; -6.845; -6.923 kcal/mol), Q3251 (-3.878; -4.356; -3.212; -6.033; -6.255 kcal/mol) and S2671 (-5.834; -7.122; -6.867; -12.855; -13.322 kcal/mol).

There are no significant differences between clusters in binding affinity for the first two ligands. Molecular docking in the case of the S2671 ligand for clusters 4 and 5 has an increased binding affinity value concerning the first three clusters, which results from the arrangement of the ligand in the structure and the characteristics of these clusters. It should be remembered that in molecular docking, the structural motif is immobile, while the ligand can move within the designated gridbox.

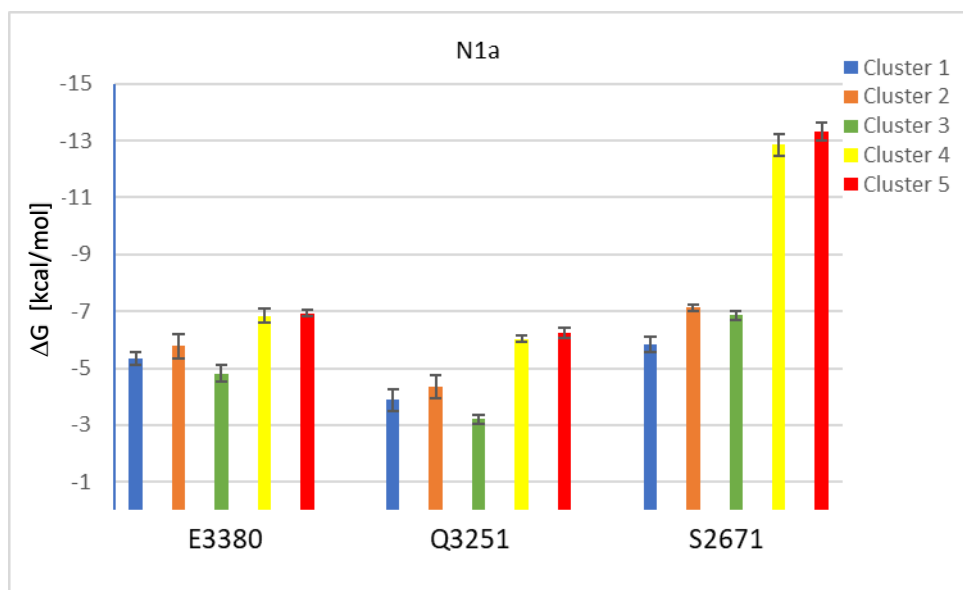


Figure 19. The binding affinity of specific Lopac SMs to the N1a motif measured in ΔG of the complex.

The N1b motif was, as well as N1a, docked with three selected ligands from the Lopac library: E3380, Q3251, and S2671 (Figure 20). The presented molecular docking was performed with cluster 1 for each SM. The interactions between ligands and tested motif were checked. One hydrogen bond has been detected between E3380 and N1b motif: the acceptor of the bond is N of the aromatic ring, and the proton donor is H61 from A28479. The length of the mentioned H-bond is equal: 2.519 Å. Three hydrogen bonds have been detected between Q3251 and N1b motif: between N from the SM aromatic ring and H7 of the A28479 (2.468 Å), between N from the SM aromatic ring and H41 of the C28480 (2.218 Å), and between OP2 of the G28478 and H of the ligand NH group (2.214 Å).

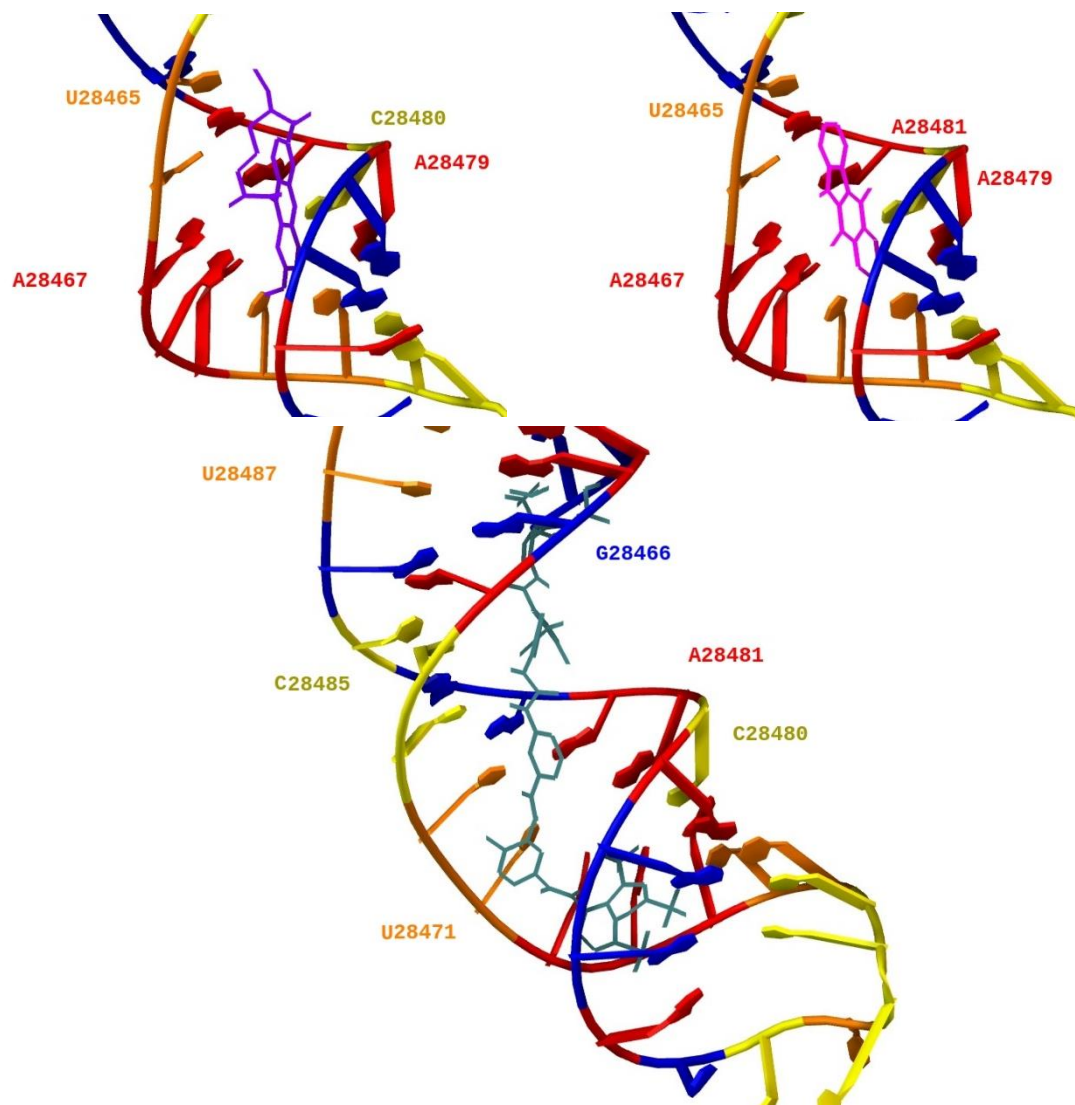


Figure 20. Molecular docking of the specific Lopac SMs for N1b motif. The colors of the ligands are following: E3380 (pink), Q3251 (purple), S2671 (emerald), and for residues: U (orange), G (blue), A (red), and C (yellow). The presented figures were prepared in AutoDockTools 1.1.2.

A very interesting result of the interaction between the N1b motif and the ligand is the case of the S2671. A rather long ligand took a position inside the vRNA structure, allowing many interactions. This binding is characterized by as many as 8 hydrogen bonds:

- H7 from G28466 and O of the ligand SO₃ group (2.247 Å)
- H61 from A28467 and O of the ligand SO₃ group (2.057 Å)
- H7 from A28481 and O of the ligand SO₃ group (2.204 Å)

- H7 from A28472 and O of the ligand SO₃ group (2.549 Å)
- H7 from A28482 and O of the ligand SO₃ group (1.682 Å)
- H7 from G28466 and O of the ligand SO₃ group (2.331 Å)
- H of the ligand NH group and O of the OP2 from G28463 (2.456 Å)
- H7 from G28486 and O of the ligands SO₃ group (1.847 Å).

The binding affinity of the selected SMs to the N1b motif were analyzed for all 5 clusters and 9 docking scores of each molecular experiment (Figure 21). The (ΔG) value suggests that the conducted investigation ran successfully and efficiently in each of the given cases. The values of the individual molecular docking listed in order from the first to the fifth cluster are as follows: E3380 (-7.633; -7.400; -6.812; -6.378; -7.400 kcal/mol), Q3251 (-6.755; -6.433; 5.945; 6.684; 5.554 kcal/mol) and S2671 (-12.478; -13.445; -12.467; -11.367; -13.233 kcal/mol).

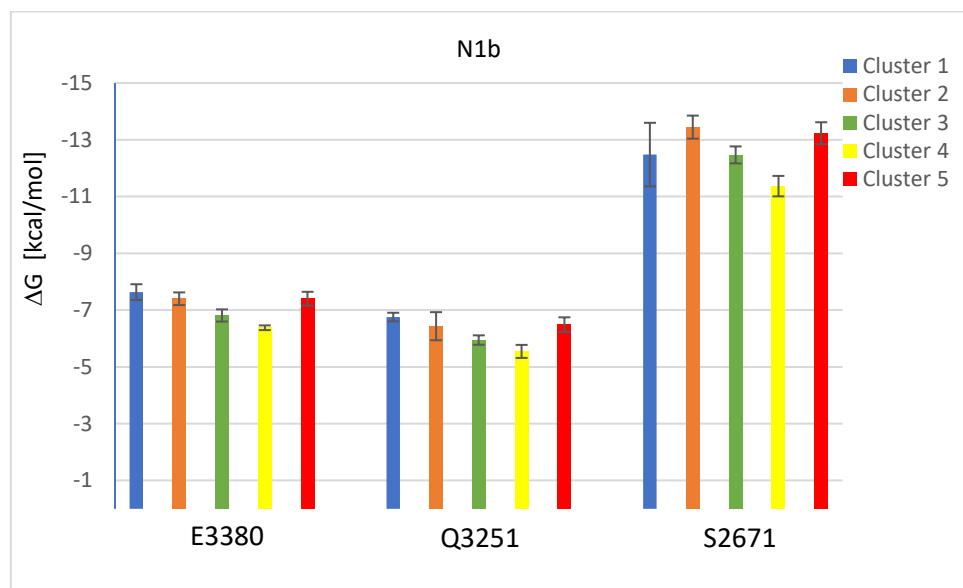


Figure 21. The binding affinity of specific Lopac SMs and the N1b motif measured in ΔG of the complex.

There are no significant differences between clusters in binding affinity. The affinity values in the case of all ligands are higher for N1b compared to N1a. However, more inter-structural interactions were found for the N1b motif. In addition, the S2671 ligand docked to this motif for all clusters showed a high number of interactions and docking within the structure.

Two ligands selected in Lopac HTS: SML1545 and SML1089, were docked to U1 structural motifs (Figure 22). The presented molecular docking was performed with cluster 1 for each SM. The interactions between ligands and tested motif were examined. Three hydrogen bonds have been detected between SML1089 and U1 motif: the acceptor of the bond is O of the OMe group, the proton donor is H7 from A118; the proton donor is H41 from C92 and ligand nitrogen of the NH group as an acceptor; O6 of the G91 and hydrogen of the NH group from the ligand. The H-bonds' lengths are as follows: 2.476 Å, 2.578 Å, 2.163 Å.

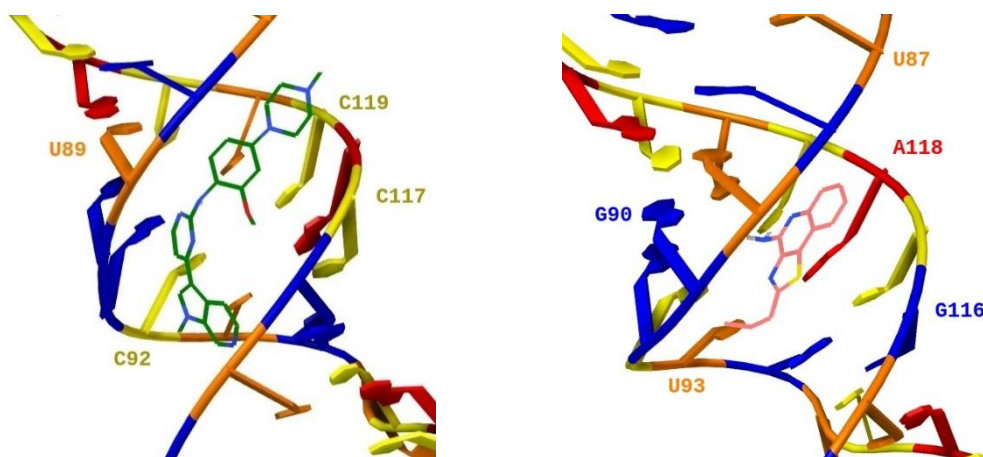


Figure 22. Molecular docking of the specific Lopac SMs for U1 motif. The colors of the ligands are following: SML1545 (pink), SML1089 (green), and for residues: U (orange), G (blue), A (red), and C (yellow). The presented figures were prepared in AutoDockTools 1.1.2.

Two hydrogen bonds have been detected between SML1545 and U1 motif: the bond acceptor is SM N of the NH group, and the proton donor is H61 from A118; the proton donor is H42 from C92, and SM nitrogen of the NH group is an acceptor. The lengths of the mentioned H-bonds are as follows: 2.351 Å and 2.198 Å.

The selected SMs and U1 motif binding affinity were analyzed for all 5 clusters and 9 docking scores of each molecular experiment (Figure 23). The value of the ΔG shows that the mentioned experiment ran well and with high efficiency in each of the given cases. The values of the individual molecular docking listed in order from the first to the fifth cluster are as follows: SML1089 (-8.565; -8.362; -8.463; -8.387; -7.972 kcal/mol) and SML1545 (-6.387; -6.287; -6.385; -6.237; -6.050 kcal/mol).

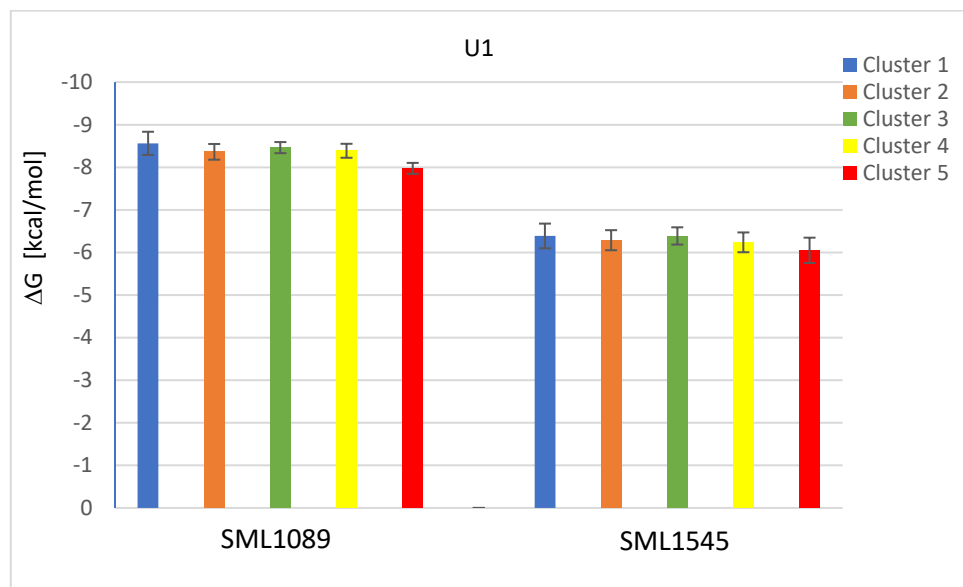


Figure 23. The binding affinity of specific Lopac SMs for the U1 motif measured in ΔG of the complex.

4.4.2. Characterization of the binding with the selected Enamine SM

The small molecules that were selected in the high throughput screening of the Enamine library were docked to molecular targets which structures were generated by molecular dynamics. The molecular dockings were performed to the following structural motifs: 3U, H-M1, H-M2, H-N1, N1a, N1b, U1, and U2. As it was for the selection of Lopac SMs, chosen compounds for docking were selective and/or possessed low IC₅₀ in FID assay.

The first presented molecular docking is the 3U motif with 3 specific hits from the Enamine library: Z281877654, Z1175020943, and Z154467994 (Figure 24). The interaction between the molecular target and ligands was investigated, and it has been found that two hydrogen bonds between the 3U motif and Z281877654 occurred between ligand N of the NH group and H61 from A29667 and H61 of the C29668. Those bonds have the following lengths: 2.783 Å and 2.198 Å, respectively.

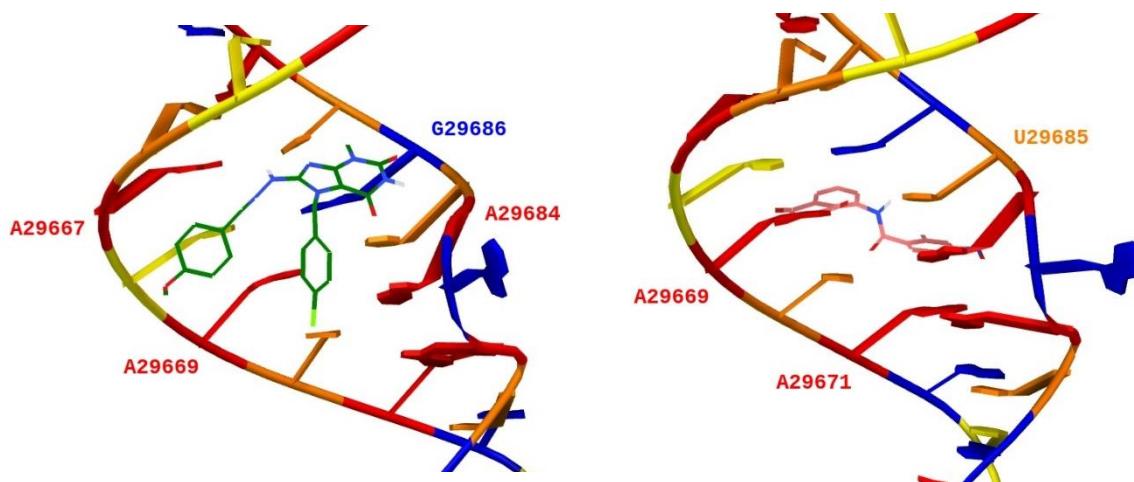




Figure 24. Molecular docking of the specific Enamine SMs for 3U motif. The colors of the ligands are following: Z281877654 (green), Z1175020943 (light pink), and Z154467994 (baby blue), and for residues: U (orange), G (blue), A (red), and C (yellow). The presented figures were prepared in AutoDockTools 1.1.2.

One hydrogen bond has been detected between the 3U motif and Z1175020943, which has occurred between ligands H of the NH group and N3 from the A29665 (2.197 Å). There were no H-bonds found between the 3U motif and Z154467994.

The selected SMs and 3U motif binding affinity were analyzed for all 5 clusters and 9 docking scores of each molecular experiment (Figure 25). The level of ΔG proves that the molecular docking ran effectively and with high efficiency in each of the given cases. The values of the individual molecular docking listed in order from the first to the fifth cluster are as follows: Z281877654 (-7.5232; -7.655; -7.667; -7.912; -6.933 kcal/mol), Z1175020943 (-7.533; -7.778; -7.656; -7.578; -7.411 kcal/mol), and Z154467994 (-7.556; -7.055; -7.155; -7.433; -7.400 kcal/mol).

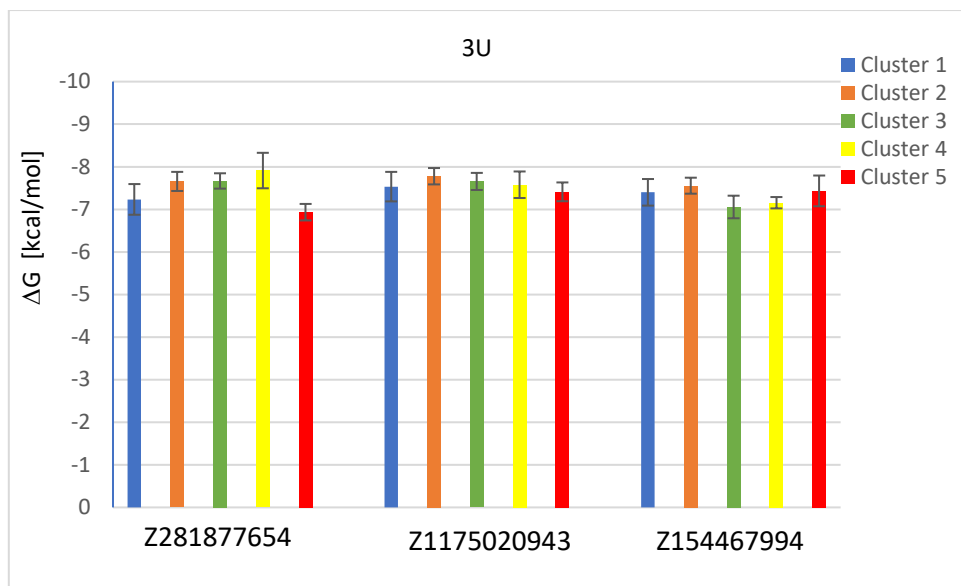
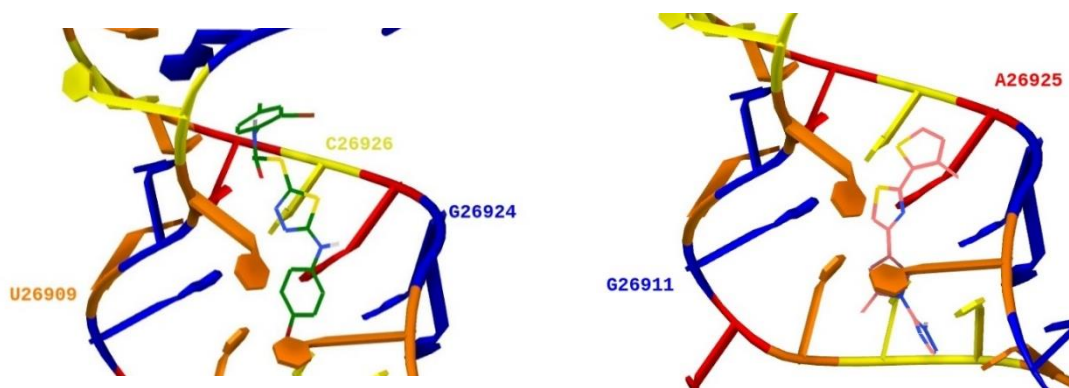


Figure 25. The binding affinity of specific Enamine SMs for the 3U motif measured in ΔG of the complex.

In the case of the H-M2 structural motif, as many as 6 selective SMs were selected based on the screening experiment with the Enamine library. The docked ligands are as follows: Z19601649, Z355285978, Z650090926, Z933632926, Z202047774, and Z238682876 (Figure 26).



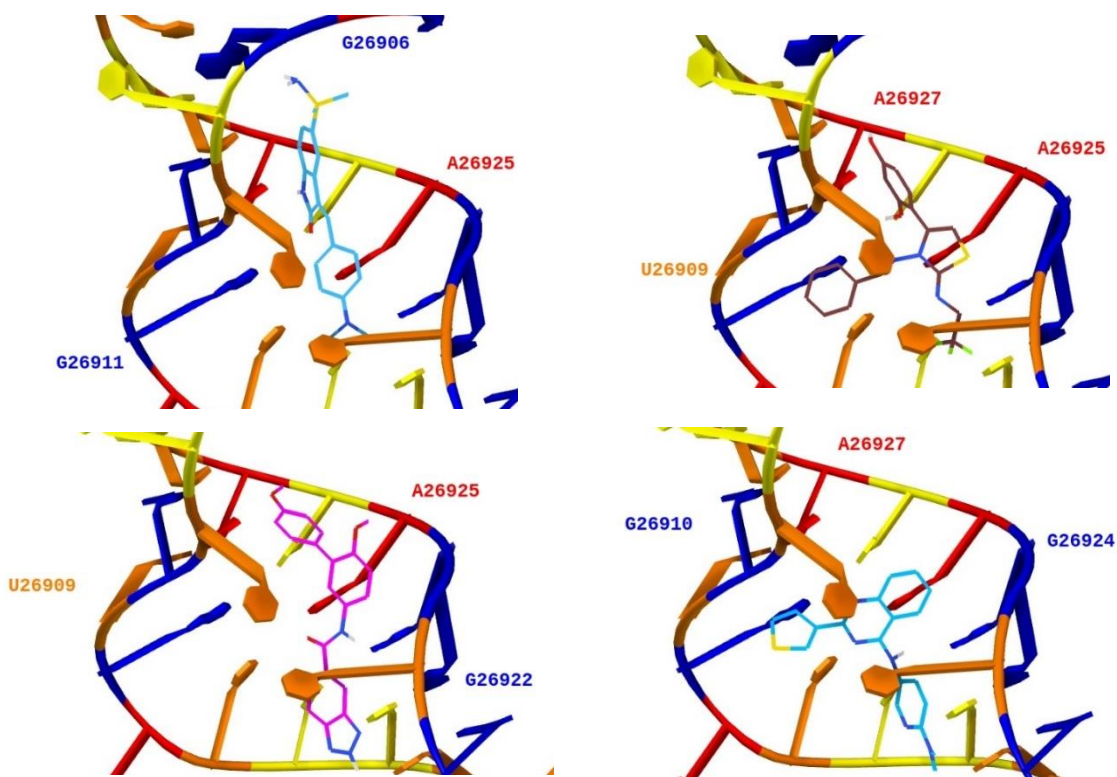


Figure 26. Molecular docking of the specific Enamine SMs for H-M2 motif. The colors of the ligands are following: Z19601649 (green), Z355285978 (light pink), Z650090926 (blue), Z933632926 (brown), Z202047774 (pink), Z238682876 (baby blue) and for residues: U (orange), G (blue), A (red) and C (yellow). The presented figures were prepared in AutoDockTools 1.1.2.

The analysis of the binding between the target molecule and selected SMs was performed, and only in the case of Z933632926 were no H-bonds found. The Z19601649 compound is characterized by a single H-bond between N from the ligand aromatic ring and H41 of C26926 (2.350 Å). One H-bond was also determined in the case of the Z355285978 and Z650090926: between SM N of the aromatic ring and H61 of A26925 (2.180 Å) and ligands H of the NH group and N7 from G26906 (2.003 Å), respectively. The Z202047774 compound is characterized by as many as 2 hydrogen bonds: between H61 from A26925 and SM of the OH (2.383 Å) and between ligands H of the NH group and N7 from G26922 (2.504 Å). The last mentioned compound, Z238682876, is described with one hydrogen bond: between O6 from the G26924 and ligand H of the NH group.

The binding affinity of the selected ligands to the H-M2 motif were analyzed for all clusters and every docking score of each molecular docking experiment (Figure 27). The energy level stipulates that the described experiment ran successfully and efficiently in each of the given cases.

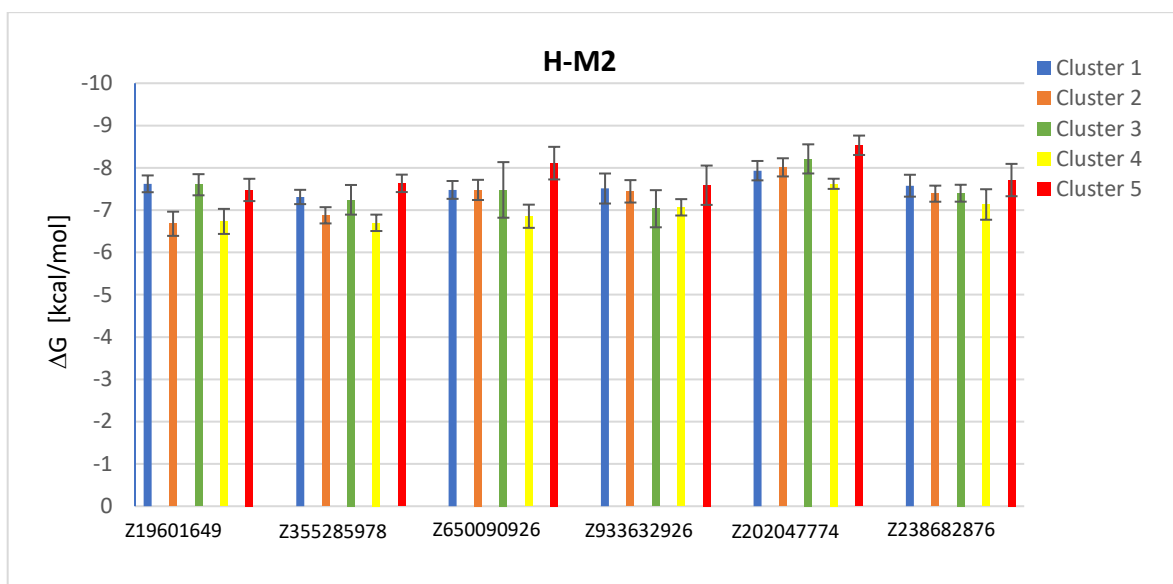


Figure 27. The binding affinity of specific Enamine SMs for the H-M2 motif measured in ΔG of the complex.

The ΔG values of the individual molecular docking are listed in order from the first to the fifth cluster in the table below (Table 16).

Table 16. Values of ΔG for H-M2 clusters complexed with ligands.

SMs name	ΔG [kcal/mol]				
	Cluster 1	Cluster 2	Cluster 3	Cluster 4	Cluster 5
Z19601649	-7.622	-6.678	-7.600	-6.733	-7.478
Z355285978	-7.311	-6.878	-7.244	-6.700	-7.633
Z650090926	-7.478	-7.478	-7.478	-6.856	-8.111
Z933632926	-7.511	-7.444	-7.033	-7.067	-7.589
Z202047774	-7.933	-8.011	-8.211	-7.622	-8.533
Z238682876	-7.578	-7.389	-7.400	-7.133	-7.711

Nextly, the H-N1 was docked with a ligand. This motif is characterized by the highest match number with ligands in HTS (10 ligands selected as decreasing fluorescence

signal). Therefore, one ligand was chosen due to its selectivity in HTS analysis, IC_{50} value, and size. The SM docked to the H-N1 motif is Z1318256185 (Figure 28).

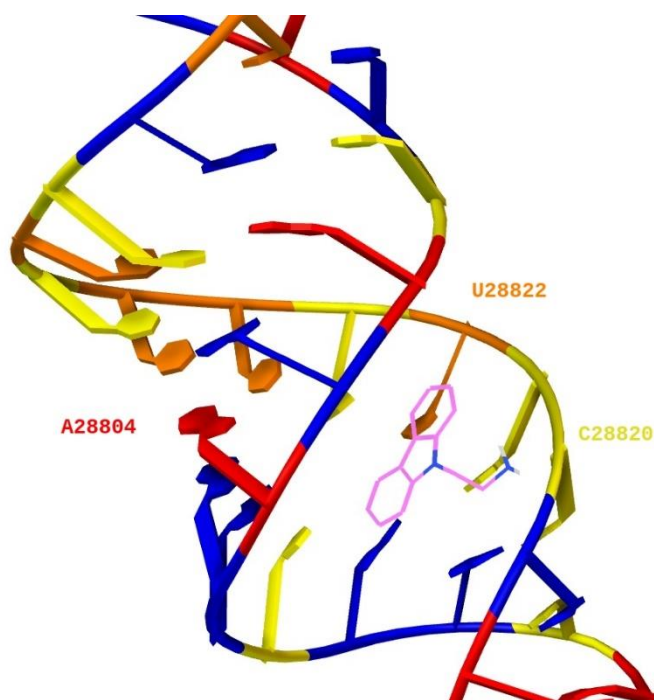


Figure 28. Molecular docking of the Enamine Z1318256185 (pink) to the H-N1 motif. Colors for residues: U (orange), and for residues: U (orange), G (blue), A (red), and C (yellow). The presented figures were prepared in AutoDockTools 1.1.2.

The analysis of the binding between H-N1 and selected SM was performed, and one H-bond was found between H of the NH group and O5 of the C28820. The ligand is docked inside the vRNA, and the free energy level shows that the described experiment ran well and with high efficiency.

The binding affinity of the Z1318256185 to the H-N1 motif was analyzed for all 5 clusters and 9 docking scores of each molecular docking experiment (Figure 29). The free energy values for clusters are as follows: -5.065; -5.237; -5.450; -5.400; -5.250 kcal/mol.

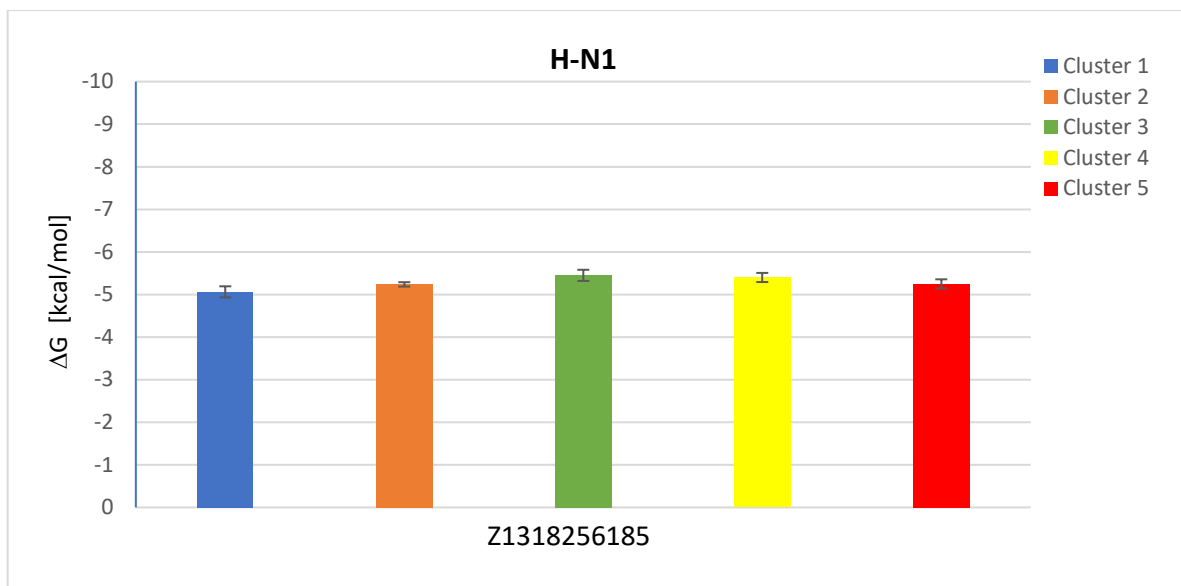


Figure 29. The binding affinity of the Z1318256185 to the H-N1 motif measured in ΔG of the complex.

The molecular docking with N1a and N1b as a target was performed. One of the Enamine SMs was selected and docked to the motif due to the fact that there was only one specific molecule in HTS for this structural motif. The selected SM is Z48626148 (Figure 30).

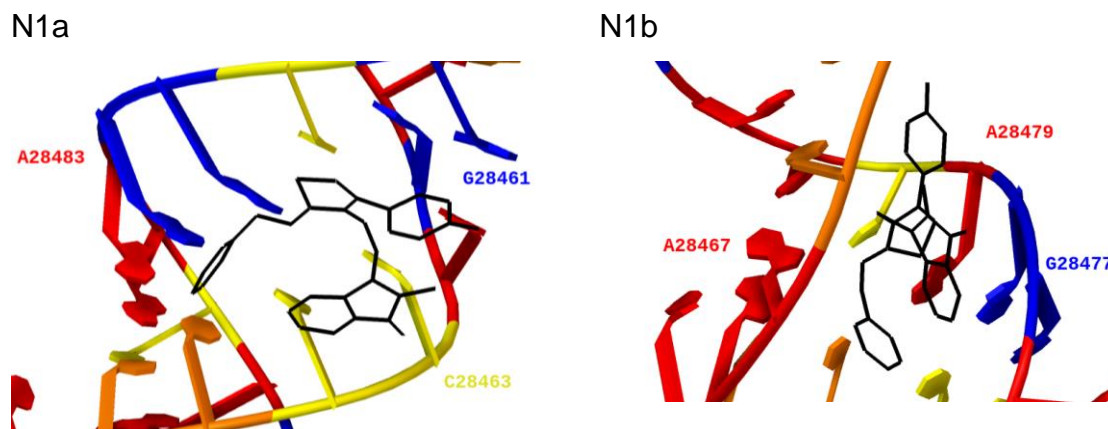


Figure 30. Molecular docking of the Z48626148 (black) to N1a and N1b motifs. The colors for residues are as follows: U (orange), G (blue), A (red), and C (yellow). The presented figures were prepared in AutoDockTools 1.1.2.

The interactions between the N1a, N1b, and ligand were investigated. It has been found that only one hydrogen bond between the N1a motif and Z48626148 occurred between ligand N of the aromatic ring and H62 of the A28462 (2.467 Å). In the case

of the N1b motif, as shown in the docking with Lopac library ligands, the formed complex is characterized by more interactions. Four hydrogen bonds have been detected between the N1b motif and Z48626148:

- H of the ligands NH group and N7 from A28467 (3.008 Å),
- H7 from A28467 and N from the ligand aromatic ring (2.145 Å),
- H7 from G28477 and sulfur from the aromatic ring of the Z48626148 (2.869 Å).

The binding affinity of the Z48626148 to N1a and N1b motifs were analyzed for all 5 clusters and 9 docking scores of each molecular docking experiment (Figure 31). The values of ΔG for clusters are as follows: N1a (-5.312; -5.733; -4.450; -7.544; -7.566 kcal/mol); N1b (-7.433; -8.300; -7.644; -6.967; -7.344 kcal/mol).

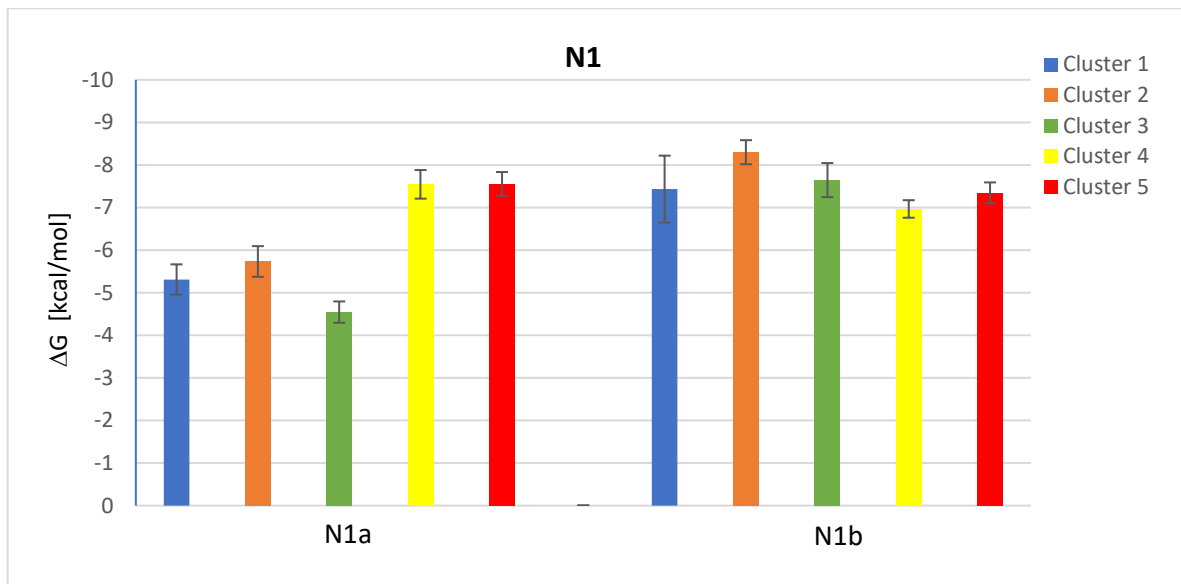


Figure 31. The binding affinity of the Z48626148 to the N1a and N1b motifs measured in ΔG of the complex.

Lastly, the Z203972446 was docked to U2 structural motif (Figure 32). During the characterization of the interaction between molecules, two hydrogen bonds were found: between H41 from the C364 and ligand O of the CO group (2.428 Å) and between ligand H of the NH group and O6 from G362 (2.166 Å).

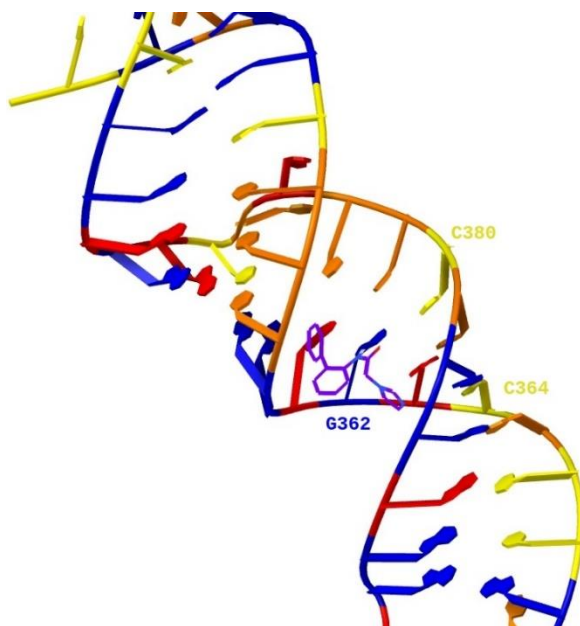


Figure 32. Molecular docking of the Z203972446 (purple) to the U2 motif. The colors for residues are as follows: U (orange), G (blue), A (red), and C (yellow). The presented figures were prepared in AutoDockTools 1.1.2.

The binding affinity of the Z203972446 to U2 was analyzed for all clusters and every docking score of each molecular docking experiment (Figure 33). The free energy for the complexes are as follows (-5.885; -5.987; -6.037; -5.987; -6.105 kcal/mol).

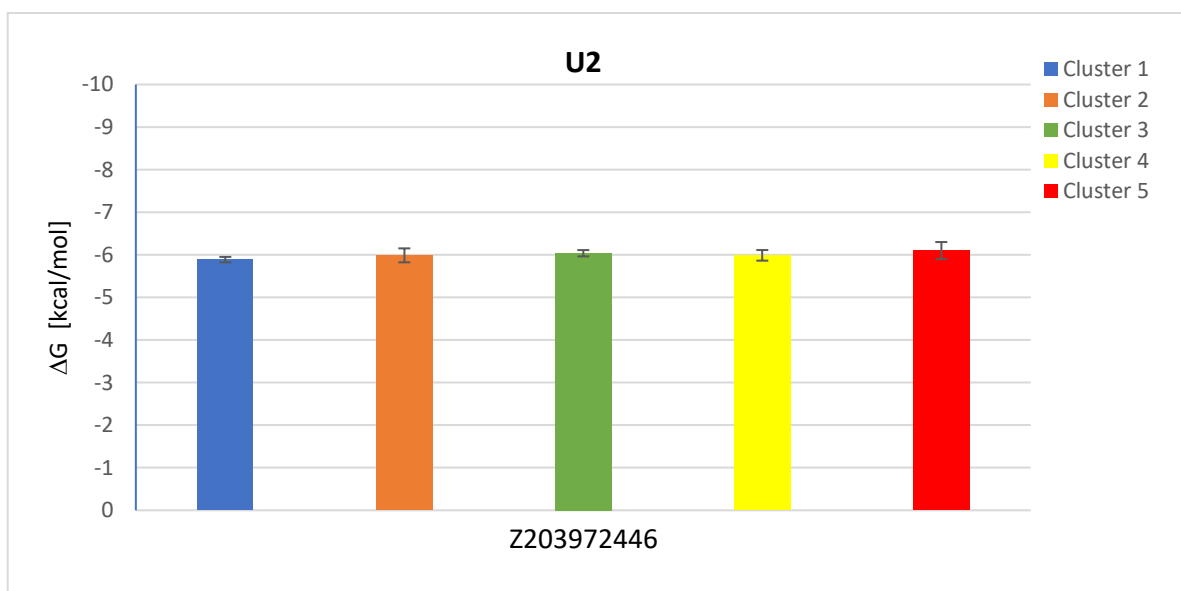


Figure 33. The binding affinity of the Z203972446 to the U2 motif measured in ΔG of the complex.

Due to the continuous underestimation of vRNA in relation to viral proteins in terms of molecular docking, no data were found for the SARS-CoV-2 vRNA structural motifs discussed in this dissertation to compare to another docking. However, it is worth mentioning the molecular docking performed with the panhandle structure (M1V motif) as a target (Figure 34) [90].

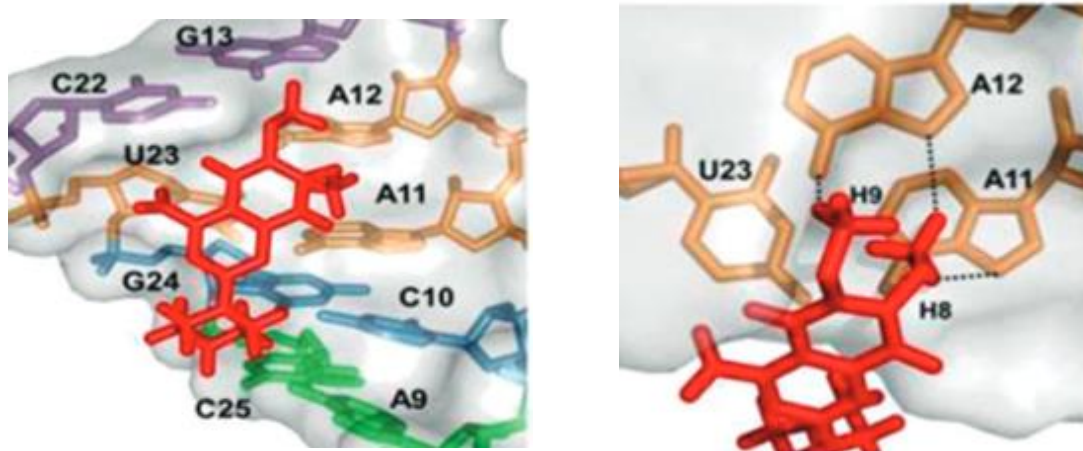


Figure 34. Molecular docking of the SM_{ref} to M1V motif [90].

In this published research, SM_{ref} was docked to the M1V motif. The interactions with the internal loop and its proximal base pairs were interpreted – three hydrogen bonds were identified and marked in the picture by black dotted lines. They were identified based on close contacts observed in the structure. The A9–A11, C21–G24, and U29–U32 were proposed as binding residues and confirmed in this dissertation as well. Selected ligands (SML2238, D3768, B1686) docked to the M1V motif in this work also bound in the area of the mentioned binding site. The compound interpreted as having the most interactions is D3768, which has three hydrogen bonds in the (A–A)–U loop and terminal helix region. Interestingly, D3768 possessed one of the lowest IC_{50} value (4.1 μM), while SM_{ref} had IC_{50} equal to 60.5 μM in the FID assay. In comparison, SML2238 had the best binding affinity ($\Delta G = -8.425$ kcal/mol) from docked compounds and better than SM_{ref} IC_{50} (52.2 μM). It was previously shown that SM_{ref} analogs bind to the M1V and inhibit IAV proliferation [83]. Finding small molecules that interact with mentioned regions of the promotor structure (panhandle, M1V) could be a fruitful approach to developing new anti-influenza drugs.

To validate the docking experiment, SM_{ref} was also docked to the M1V for this dissertation (Figure 35). The results of the docking carried out by the author of the dissertation and presented in the cited publication can be compared as similar. There are similar ligand binding sites. Also, in the case of the dissertation, hydrogen bonds have been identified. Three hydrogen bonds were identified: between N6 of the A5 and H of the ligand OMe group (2.318 Å), between N6 of the A7 and H of the SM NH₂ group (2.502 Å), between N of the ligand aromatic ring and H62 of the A7 (2.289 Å). The binding affinity value is equal - 6.9 kcal/mol measured in the ΔG .

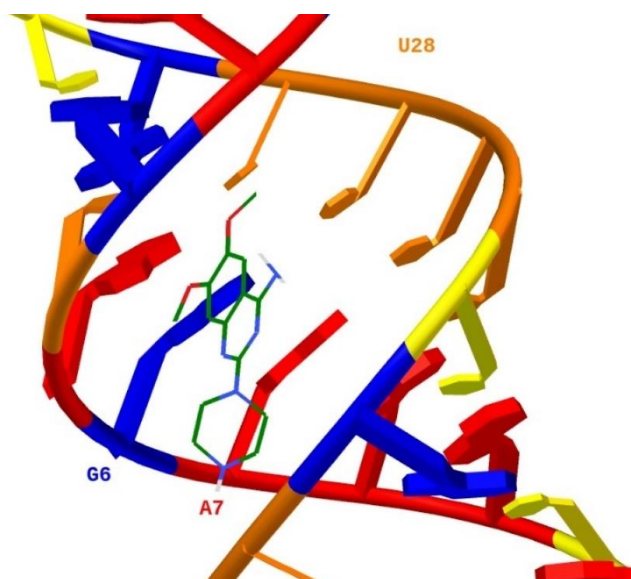


Figure 35. Molecular docking of the SM_{ref} to M1V motif was performed by the author of this dissertation.

Referring to the fact that docking is a random experiment based on the Monte Carlo method, it is known that the results could not show identical values. Unfortunately, due to the fact that the experiment in this work was performed *in silico* and the binding affinity value in the reference publication was based on an *in vitro* experiment, it cannot be compared.

The most important conclusion from the analysis for all complexes of target vRNAs is that the data about SM binders from the HTS experiment were confirmed. The compounds selected in the high throughput analysis were correctly docked in the conducted experiments. Based on molecular docking, it was possible to determine the binding site of individual ligands. In all cases, the interactions between vRNA

structural motifs and ligands were visualized, the distances between individual atoms were measured, and the binding affinity was calculated.

It should be remembered that virtual experiments are still at the stage of dynamic development, and their result is not indisputable. The wet-lab is more reliable, and its results cannot be undermined by the results of a virtual experiment. However, combining the data of both experiments seems to be the most appropriate and broad approach in the field, which not only enriches the knowledge of given interactions or predicted ligand binding site and enables further development of the virtual analysis.

4.5. Small molecules as inhibitors of IAV replication

Cell experiments were conducted to confirm the inhibitory properties of selected SMs of the Enamine/Lopac library. The research is divided into 2 groups for each library. The cell experiments proceeded for IAV only due to the unavailability of BSL III conditions.

4.5.1. Inhibitory potential of selected Lopac library compounds

To confirm that the change in viral RNA concentration is only due to the inhibitory properties of the test compounds, the experiment was preceded with a cell viability test. The CellTiter-Glo Luminescent Cell Viability Assay (Promega) was performed to assess the impact of selected Lopac library SMs for MDCK cell viability (Figure 36). The results of the presented assay showed that six out of fourteen compounds negatively impact on cell viability, at least in the highest concentration. Due to this fact, results for 10 μ M concentration of P8293, Q3251, B1686, D3786, and E3380 were no longer analyzed, and M6545 was excluded from the analysis.

The remaining compounds do not show a cytotoxic effect on MDCK cells in the tested concentration range compared to the untreated control. Therefore, it can be concluded that their inhibitory effect on the viral replication of IAV is related to the specific activity of the SMs and not to cell viability reduction.

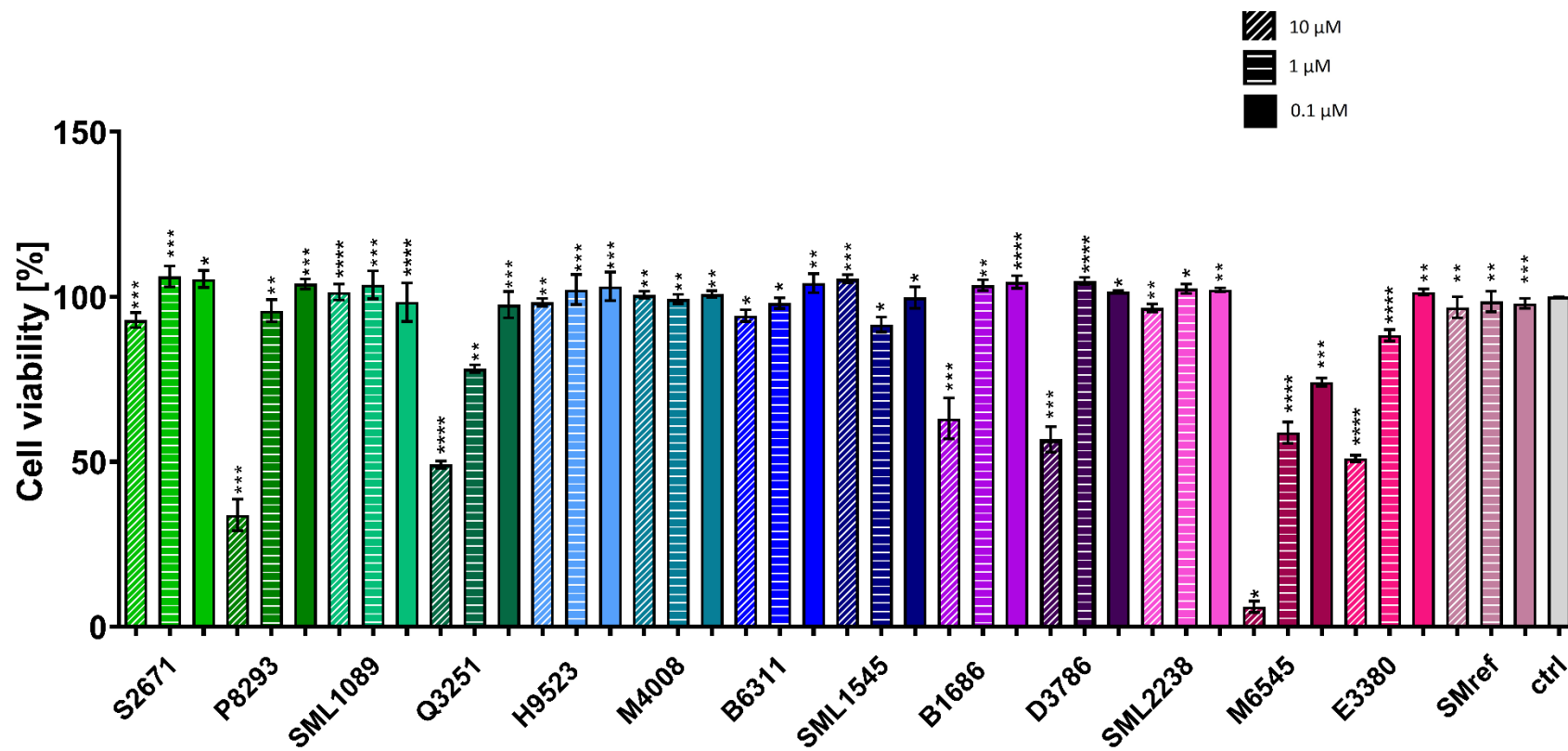


Figure 36. Viability test results for the MDCK cells treated with Lopac small molecules in three different concentrations. Error bars represent standard deviations of independent experiments. Statistical analysis has been done using the student's t-test (***) $p < 0.001$; **) $p < 0.01$; *) $p < 0.05$).

Next, cell culture experiments were performed to determine the antiviral potential of selected SMs. MDCK cell line was treated separately with S2671, P8293, SML1089, Q3251, H9523, M4008, B6311, SML1545, B1686, D3768, SML2238, M6545, E3380, SM_{ref} and infected with influenza A/California/04/2009 (H1N1) virus. The level of the virus in SM-treated samples and controls was tested by immunofluorescence focus formation assay (IFA) and RT-qPCR. Both analyses were conducted as described in Methods and Materials (6.2.9 Immunofluorescence Focus Formation Assay; 6.2.13 Real-time qPCR with reference gene).

The immunofluorescence focus formation assay helps to exclude inactive and infectious incapable virions from quantitative virus analysis. Nine out of thirteen selected compounds of the Lopac Library, in nontoxic concentrations, can inhibit the multiplication of IAV, as was shown in IFA. S2671, P8293, Q3251, M4008, SML1545, SML2238, and SM_{ref} inhibit IAV multiplication with at least 10-fold efficiency. B6311 and B1686 inhibit IAV multiplication with at least 5-fold efficiency due to the lowest concentration. Thus, the highest inhibition is observed for 10 μ M concentration of SML2238 (Figure 37). The mentioned SM caused a 30-fold viral

titer decrease. A tendency was observed that the inhibition efficiency increased with the increase of the tested ligand concentration.

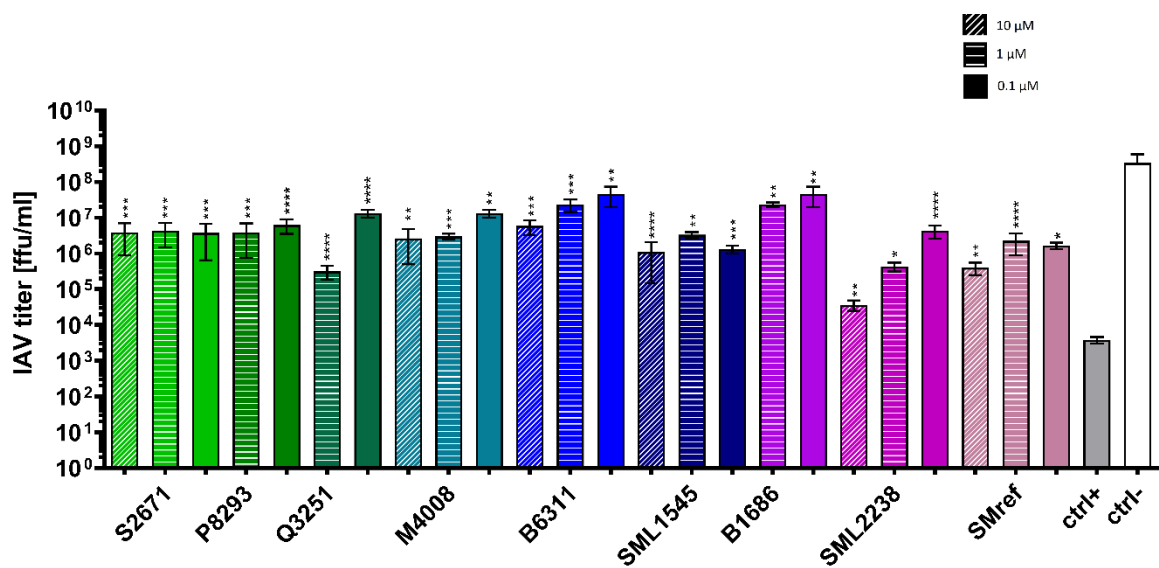


Figure 37 Antiviral activity of selected Lopac SMs in the IFA test. The results obtained for the SMs were compared with the negative control (ctrl-, representing 100%). Ctrl+ is cells treated with ribavirin, and ctrl- is untreated cells. Error bars represent the standard deviation of independent experiments. Statistical analysis was performed using the student's t-test (** $p < 0.001$, ** $p < 0.01$, * $p < 0.05$).

The inhibitory properties of SML2238 are shown in the fluorescence microscopy images (Figure 38). The number of infected nuclei in the SM-treated well and the negative control can be compared when analyzing the presented images. Based on the data presented, it can be unequivocally concluded that the tested SML2238 causes a decrease in the production of infectious virions compared to the untreated control.

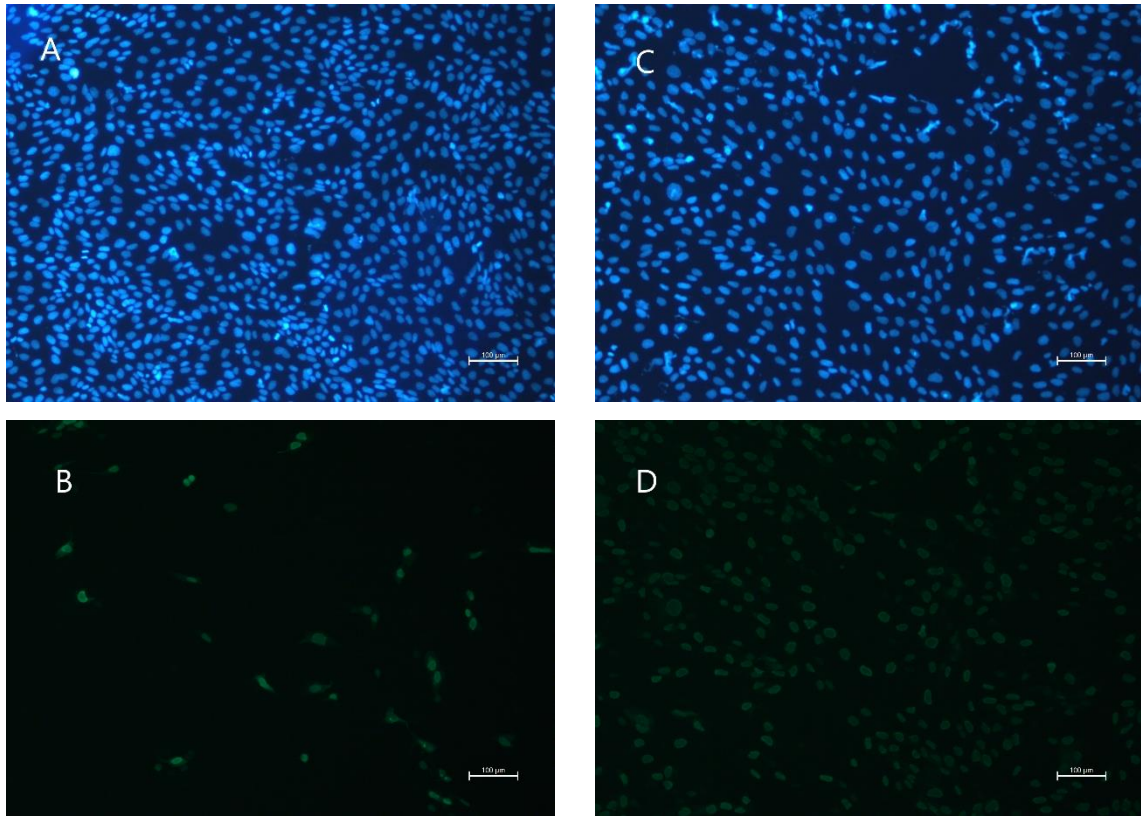


Figure 38 Fluorescence microscopy images of MDCK cell cultures infected with influenza virus in the IFA assay. (A) and (B) show a culture treated with SML2238 at a concentration of 10 μ M (C) and (D) a negative control. Green fluorescence is from influenza virus antibodies targeting the NP protein, and blue is nuclear staining using DAPI.

Next, the antiviral activity of the selected SMs was determined by measurements of viral RNA level by RT-qPCR analysis. The reaction determined the number of viral RNA copies in the SMs-treated cells and compared them with untreated controls (Figure 39).

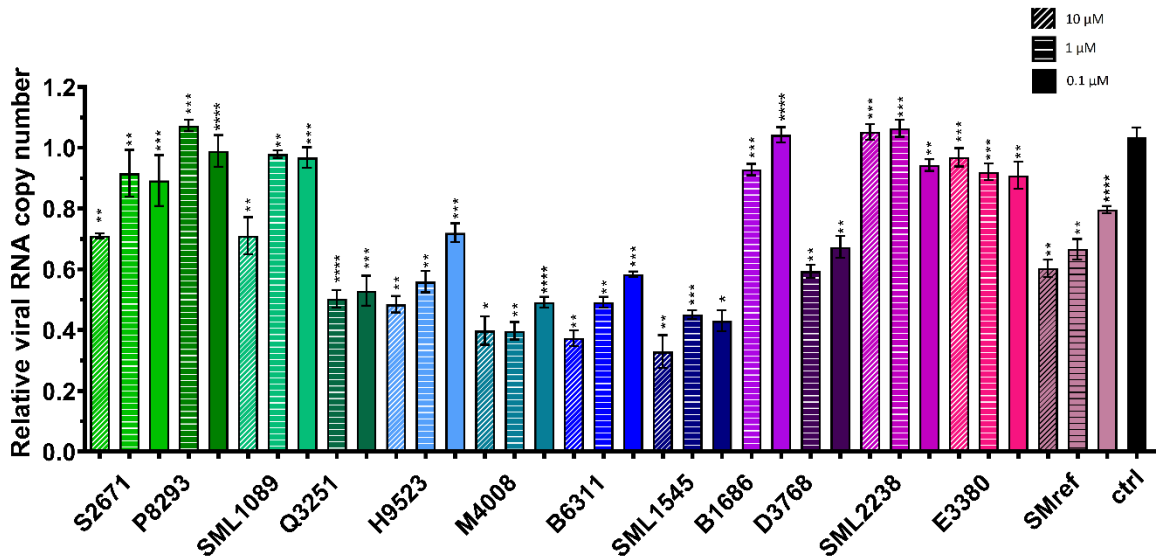


Figure 39. Inhibitory potential of SMs against strain A/California/04/2009 (H1N1) in MDCK cells. The relative viral RNA copy number was determined by RT-qPCR. The values obtained for the SMs treated cells were compared with those obtained for the negative control (untreated, infected cells) (ctrl-, representing 1). Error bars represent the standard deviation of independent experiments. Statistical analysis has been performed using the student's t-test (** $p < 0.001$; ** $p < 0.01$; * $p < 0.05$).

Nine out of thirteen tested compounds showed significant inhibitory properties according to the RT-qPCR results: S2671, SML1089, Q3251, H9523, M4008, B6311, SML1545, D3768, and SM_{ref} (Table 17). The most crucial reduction of the relative vRNA copy number is caused by SML1545, B6311, and M4008. The mentioned SMs are characterized by a decrease in the number of vRNA copies in the experiment by over 60%.

Table 17. Results of relative vRNA copy number reduction for the best Lopac SMs in RT-qPCR analysis.

SMs name	Reduction of relative vRNA copy number		
	10 μ M	1 μ M	0.1 μ M
S2671	29.0 %	8.8 %	10.8 %
SML1089	28.9 %	2.1 %	3.2 %
Q3251	-	49.7 %	47.0 %
H9523	51.5 %	44.0 %	27.9 %
M4008	60.1 %	59.2 %	50.8 %
B6311	62.6 %	50.8 %	41.6 %
SML1545	67.0 %	54.8 %	56.9 %
D3768	-	40.6 %	32.6 %
SM _{ref}	39.7 %	33.4%	21.4 %

The compounds which inhibitory properties were confirmed in both experiments were: S2671 (29% of inhibition, viral titer decrease at least 10-fold), Q3251 (49.7% of inhibition, viral titer decrease at least 10-fold), M4008 (60.1% of inhibition, viral titer decrease at least 20-fold), SML1545 (67.1% of inhibition, viral titer decrease at least 20-fold), B6311 (62.6% of inhibition, viral titer decrease at least 5-fold), SM_{ref} (39.7% of inhibition, viral titer decrease at least 20-fold). The values in parentheses refer to the highest concentration tested for the compound. It is worth noting that several new compounds appeared to inhibit virus propagation better than SM_{ref}.

4.5.2. Inhibitory potential of selected Enamine library compounds

The CellTiter-Glo Luminescent Cell Viability Assay (Promega) was performed to assess the impact of selected SM on MDCK cell viability (Figure 40). The results of the presented assay show that from twenty-one selected in HTS hits, only seven compounds have no negative impact on cell viability. Due to this fact compounds Z1318256185, Z933632926, Z56768568, Z19601649, Z1272208728, Z223816872, Z281877654, Z165209348, Z238682876, Z239612492, Z355285978, Z54851547, Z1213651838 and Z2856407960 were no longer analyzed.

The remaining compounds do not show a cytotoxic effect on MDCK cells in the tested concentration range compared to the untreated control. Therefore, their inhibitory effect on the viral replication of IAV should be related to the specific activity of the SMs on the virus.

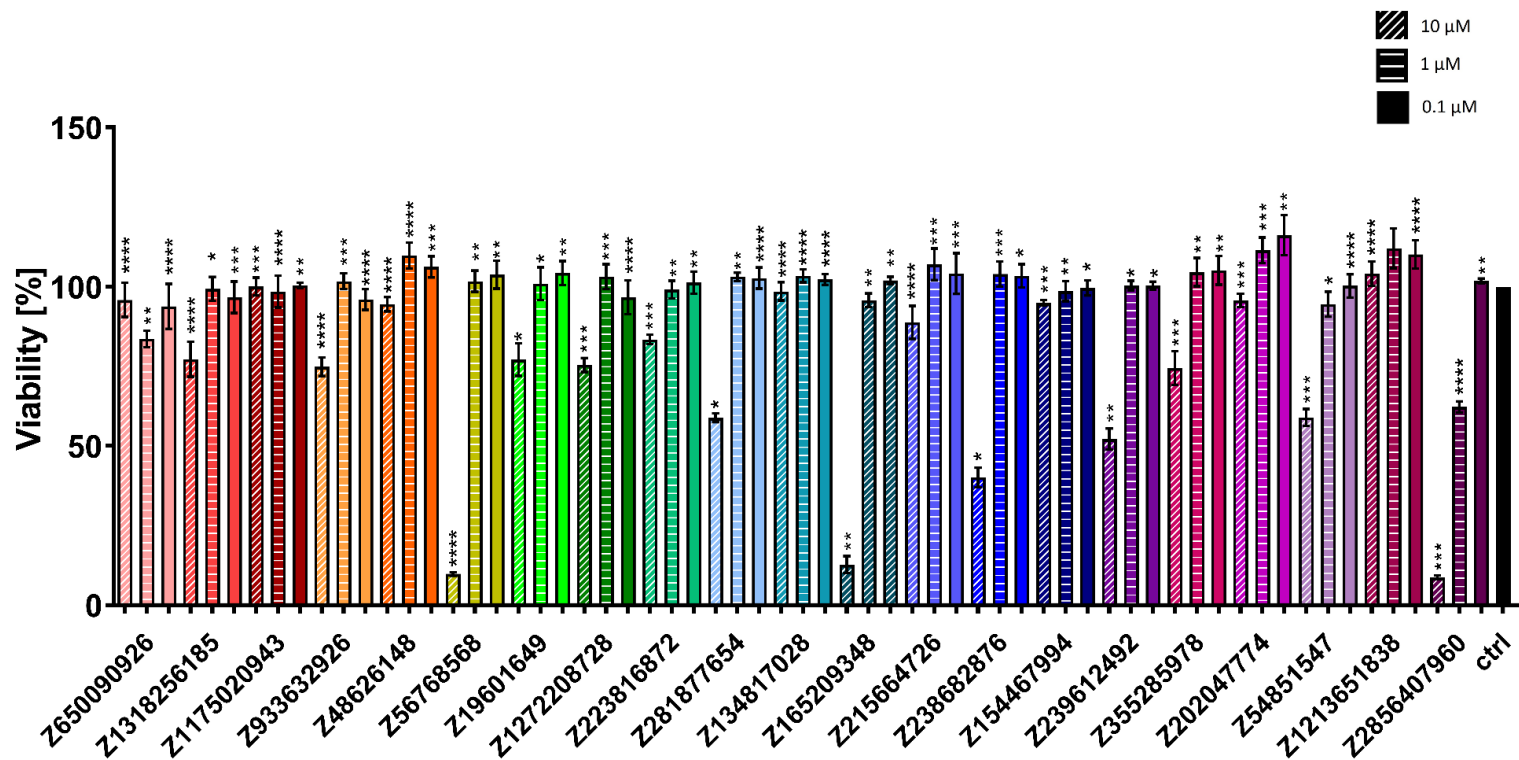


Figure 40. Viability test results for the MDCK cells treated with Enamine small molecules in three different concentrations. Error bars represent standard deviations of independent experiments. Statistical analysis has been performed using the student's t-test (**p<0.001; **p<0.01; *p<0.05).

Cell culture experiments were performed to determine the antiviral potential of selected SMs. MDCK cell line was treated with Z650090926, Z1175020943, Z48626148, Z134817028, Z215664726, Z154467994, Z202047774 and infected with influenza A/California/04/2009 (H1N1) virus. Similarly, as for Lopac library SMs, the level of the virus in SM-treated cells was measured by IFA and RT-qPCR. Both analyses were conducted as described in Methods and Materials (6.2.9 Immunofluorescence Focus Formation Assay; 6.2.13 Real-time qPCR with reference gene).

Two of the Enamine Library's seven compounds, Z134817028 and Z215664726, in nontoxic concentrations, can effectively inhibit the replication of IAV, showed in IFA. The highest inhibition is observed for a 10 μ M concentration of Z215664726 (Figure 41). The mentioned SM caused a viral titer decrease for over 2 logs. In the case of the Z154467994 in the highest concentration, the compound is observed to inhibit IAV multiplication with at least 5-fold efficiency. A dose-dependent inhibition was observed: inhibition efficiency increased with the increase of the tested ligand concentration.

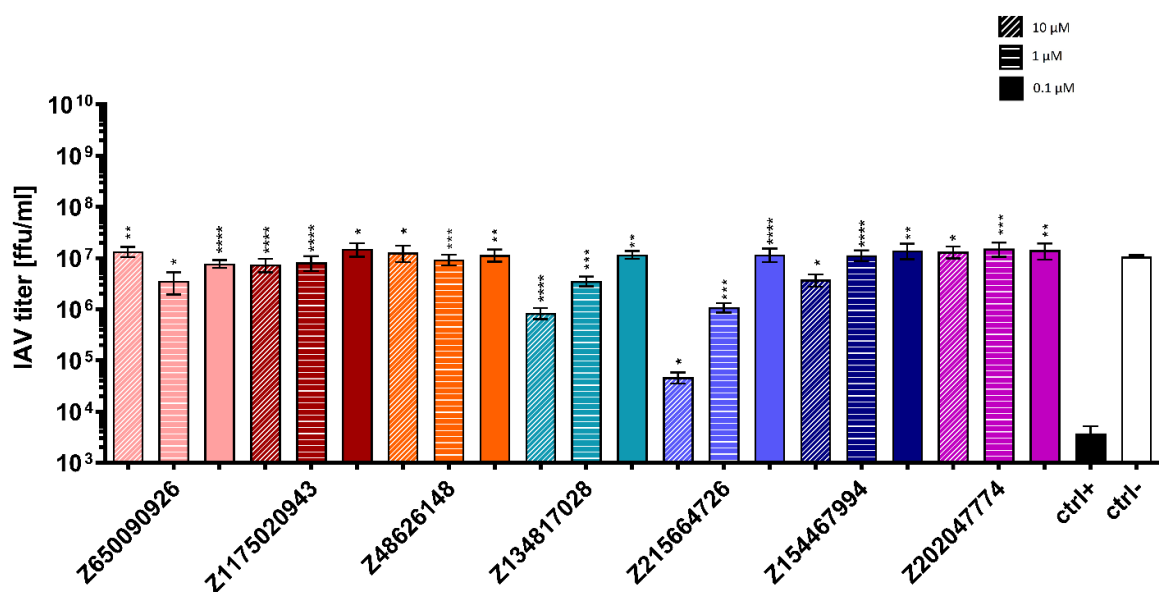


Figure 41. Antiviral activity of selected Enamine SMs in the IFA test. The results obtained for the SMs were compared with the negative control (ctrl-, representing 100%). Ctrl+ is infected cells treated with ribavirin, and ctrl- is infected untreated cells. Error bars represent

the standard deviation of independent experiments. Statistical analysis has been performed using the student's t-test (** $p < 0.001$; ** $p < 0.01$; * $p < 0.05$).

The fluorescence microscopy images show the inhibitory properties of Z215664726 analyzed in IFA (Figure 42). During IFA, the number of infected nuclei in the SM-treated and in the negative control wells can be compared. The measurement showed that Z215664726 causes a decrease in the production of infectious virions compared to the untreated control.

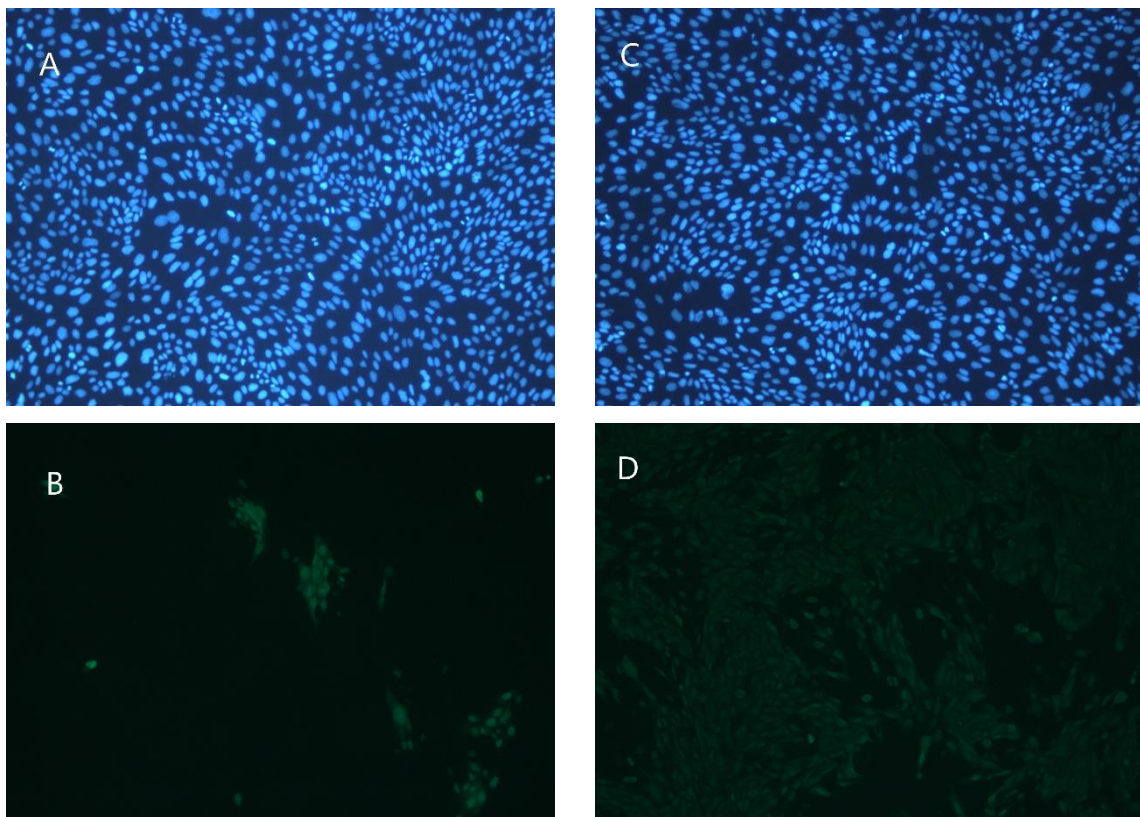


Figure 42 Fluorescence microscopy images of MDCK cell cultures infected with influenza virus in the IFA assay. (A) and (B) show a culture treated with Z215664726 at a concentration of 10 μM (C) and (D) a negative control (infected and untreated cells). Green fluorescence is from influenza virus antibodies targeting the NP protein. Blue is nuclear staining using DAPI.

Next, the antiviral activity of the selected SMs was determined by measurements of viral RNA level by RT-qPCR analysis. The analysis determined the number of viral

RNA copies in the SMs-treated cells and compared them with untreated controls (untreated infected cells) (Materials and Methods). Three of the seven selected nontoxic compounds showed a significant decrease in relative vRNA copy level (Figure 43).

Z134817028 reduces viral RNA copy number by over 27% in the highest concentration. For 1 μM , the inhibition level equals 21.7% and mentioned SM does not show inhibitory properties at the lowest concentration. Z215664726 at the highest concentration lowered relative vRNA copy number compared to control by 35.1%. For 1 μM , it is 20.4%, and there are no significant changes in the relative vRNA copy number at the lowest concentration. Z154467994 showed the most crucial inhibitory properties of all selected SMs. At 10 μM , it reduced the relative vRNA copy number by over 36 % compared to the untreated control. Lower inhibitory properties characterize the middle concentration, which is 13.3 % compared to the untreated control. There are no significant changes in the relative vRNA copy number at the lowest concentration.

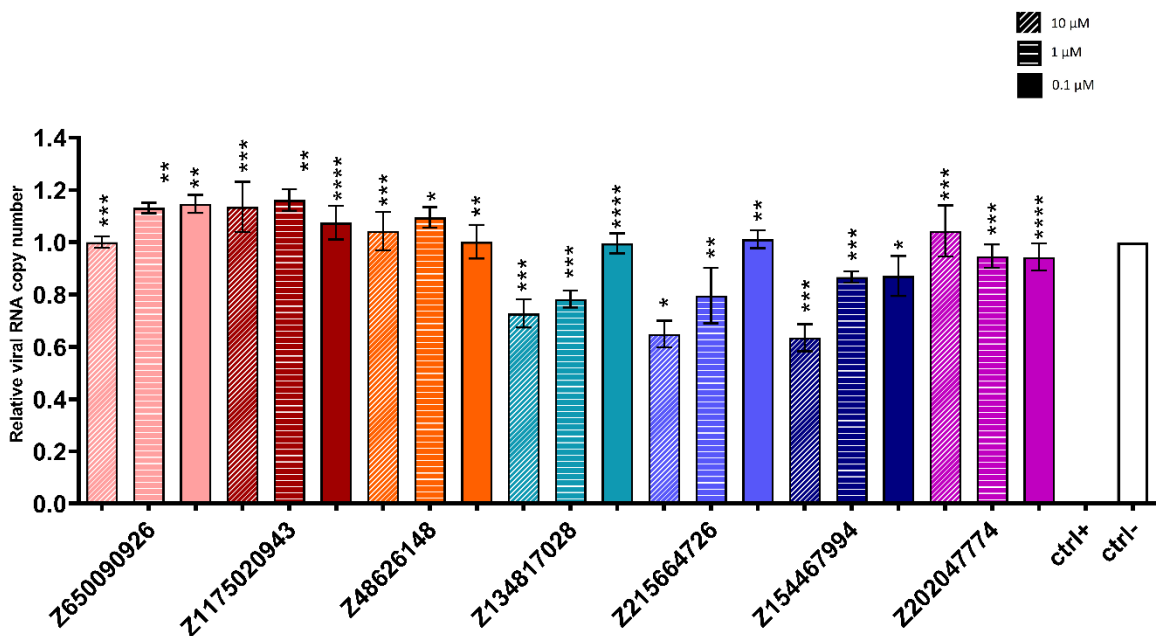


Figure 43. Inhibitory potential of Enamine SMs against strain A/California/04/2009 (H1N1) in MDCK cells. The relative viral RNA copy number was determined by RT-qPCR. The

*values obtained for the SMs treated cells were compared with those obtained for the negative control, ctrl- (untreated, infected cells; representing 1). Ctrl + are cells treated with 40 μ M ribavirin. Error bars present the standard deviation of independent experiments. Statistical analysis has been done using the student's t-test (** $p < 0.001$; * $p < 0.01$; $p < 0.05$).*

The conducted experiments confirmed antiviral properties against IAV of a part selected small molecules from HTS. Such a result was expected in cellular conditions because the biological effect is dependent on the availability of RNA motif and its real importance in the viral cycle, as well as unexpected binding to other molecules can occur that can diminish inhibitory properties. The highest inhibition of virus propagation was achieved for Lopac small molecules SML1545, B6311, and M4008 (confirmed in RT-qPCR and IFA) as well as SML2238 (IFA).

The SML1545 is a protein tyrosine phosphatase inhibitor. It is an analog of Trodusquemine. The B6311 compound is a Polo-like kinase inhibitor, and M4008 is characterized as a flavonoid with anti-oxidant properties. While SML2238 shows the specificity to the ARF6 guanine nucleotide exchange factors (GEF) binding region. The Lopac library is a collection of pharmacologically active compounds, so it is an interesting observation that some of them interact with IAV RNA and effectively diminish virus propagation.

The best Enamine small molecules (Z154467994, Z134817028, and Z215664726) disturb IAV replication in the range of 36-27%. While the effect is not spectacular, it needs to be noted that none of these compounds have previously been published as potential drugs and are therefore worthy of further study.

Cell experiment on IAV was conducted with all compounds selected in HTS, which means there were small molecules recognized as binders to different studied RNA motifs from both IAV and SARS-CoV-2. Compounds that bind to SARS-CoV-2 RNA motifs were therefore tested as an additional control, assuming no effect. FID assay showed that the B6311 and M4008 mechanism of action during inhibition of IAV replication could be a tight binding to the M4 motif located in vRNA8, as well as they could bind tightly to panhandle motif (M1V), what is observed in HTS results (4.2 Selection of SMs from Lopac and Enamine library; Table 7). So far, only SMs that

bind to panhandle motif (M1V) have been published as RNA targeting anti-IAV small molecules [90]. M4 motifs appeared to be a good target for potential drugs not only for oligonucleotides [121] but also for SMs. The M4 motif is an excellent SM target, unlike the M1V, which was targeted by many compounds in high throughput analysis, indicating a lack of selectivity in binding. SML1545, discovered here as a SARS-CoV-2 U1 motif binder, surprisingly inhibited IAV propagation. The target is probably the M1V motif, which is deduced in the HTS analysis (4.2 Selection of SMs from Lopac and Enamine library; Table 7). All three Enamine small molecules: Z154467994, Z134817028, and Z215664726 in HTS were found to bind SARS-CoV-2 RNA motifs: 3U, H-M1, and U1, respectively. It could be concluded that these compounds have anti-viral properties with unknown targets in IAV, maybe functional RNA motifs, as these compounds are intended to be RNA specific (RNA Enamine library).

Z154467994 has a high potential to inhibit SARS-CoV-2 RNA because it could bind to the 3U motif, as it was shown in FID assay and molecular docking. 3U was previously a target for small molecule inhibitor design as a part of a bigger RNA domain, but found compound (D01) was not so far evaluated against the virus [122]. Whereas the U1 motif (named SL4 in 5'UTR of SARS-CoV-2 RNA) was already successfully targeted by small molecules inhibiting virus titer as well as expression in a model reporter assay [123]. It makes SMs specific to U1 discovered in this dissertation of great interest.

The M6545 compound from the LOPAC library was excluded from the analysis due to the negative impact on cell viability. The SM showed in the FID assay very low IC_{50} values for every structural target. It is bound to each of the tested structural motifs. Therefore, it can be concluded that its cytotoxic nature results from the fact that this compound easily and non-specifically binds to many RNA motifs. However, this can be seen as an advantage of this SM, and it could be used as a positive control in testing new RNA structural motifs in the newly established FID assay.

5. SUMMARY

Most IAV and SARS-CoV-2 replication inhibitors research is focused on viral proteins. However, RNA as a target for inhibitors is one of the innovative and fast-evolving approaches. Few research groups target viral RNA with antisense oligonucleotides, peptide nucleic acids, small interfering RNAs, and small molecules. This dissertation presents an approach to find small molecules from commercial small molecule libraries (Lopac and Enamine) that tightly bind viral RNA and could inhibit the propagation of targeted viruses.

In this work, several research methods were used, i.e., high throughput screening of two small molecule libraries, molecular dynamics of viral RNA motifs, molecular docking of SMs to the selected vRNA motifs, and evaluation of the antiviral potential of the chosen SMs in the cell line.

Very important was choosing an RNA target. The targets were conserved RNA motifs of viral RNA of IAV or SARS-CoV-2 that fulfill several criteria such as structural conservation, thermodynamic stability, and occurrence in the genome - ideally in virion or/and cellular condition. A confirmed function of the RNA motif was a valuable added bonus.

HTS of Lopac and Enamine libraries gives an analysis of over 10,000 compounds with 2 IAV RNA structural motifs and 7 SARS-CoV-2 RNA motifs. The main aim of this part was to find small molecules that strongly bind to selected conserved RNA structural motifs of the IAV and SARS-CoV-2. Based on the analyzed data, a total of 36 compounds were selected from the analysis and used in further investigations.

The molecular dynamics simulations' goal was to find and characterize 3D structures of selected RNA motifs. In MDS, seven SARS-CoV-2 RNA structures were prepared, nextly analyzed, clustered, and used in molecular docking with small molecules selected in the HTS analysis. Docked compounds were analyzed for the binding affinity to conserved RNA structural motifs, intermolecular interactions, and visualized. Valuable structural data about potential anti-IAV and anti-SARS-CoV-2 inhibitors were collected that can be used in future research in our group and also

for others scientists. Only part of the small molecules interesting in terms of binding properties to RNA motifs of IAV or SARS-CoV-2 genome were tested in cells against the virus. Based on the achieved *in vitro* data, it is highly possible that some of the SMs not tested yet can also influence viral propagation by targeting RNA.

Thirty-six selected SMs were evaluated for the putative antiviral potential against a strain of influenza A virus, A/California/04/2009 (H1N1), in the MDCK cell line. The CellTiter-Glo Luminescent Cell Viability Assay was performed to assess the impact of selected SMs on MDCK cell viability. The results of the mentioned assay show that from thirty-six selected in HTS hits, twenty-one compounds have no negative impact on cell viability. 11 SMs (S2671, Q3251, M4008, B6311, SML1545, SML1089, H9523, SM_{ref}, Z134817028, Z215664726, and Z154467994) of the tested compounds caused a significant reduction in viral RNA copy number checked by RT-qPCR analysis, and lowered viral titer in the immunofluorescence focus formation assay. Two compounds (P8293, SML2238) showed the inhibition of the multiplication of IAV in IFA, and the D3768 significantly reduced viral copy number (40.6% for 1 μ M concentration). However, the antiviral properties of these 3 compounds were not observed in the other evaluation method. Some acceptable differences in the results in both presented cell assays are from different measurement techniques: RT-qPCR analysis allows to measure of the amount of all vRNA isolated from cellular material. In contrast, in IFA measures only infectious particles and helps to exclude inactive and infectious incapable virions from quantitative virus analysis.

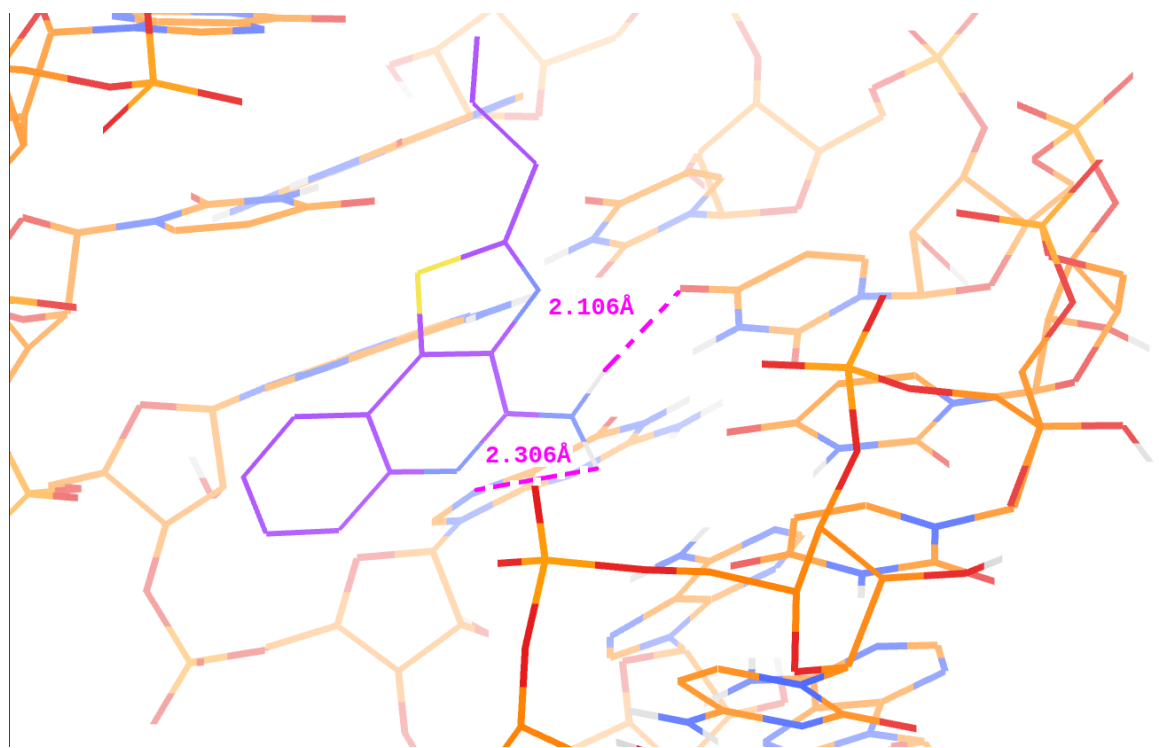
The most viral RNA copy-reducing compound from the Lopac library is SML1545, characterized by great antiviral properties – it decreased the viral RNA copy number at the highest concentration by 67% (structure: Table 6). It is also called Claramine TFA salt. Claramine is known as a protein tyrosine phosphatase 1B (PTB1B) inhibitor. This SM is a selective inhibitor of the PTB1B, not its closest related phosphatase TC-PTP. Claramine is responsible for activating insulin signaling and increasing phosphorylation of insulin receptor- β (IR β). The mentioned SM improved insulin sensitivity, restoring glycemic control in diabetic mice, and suppressing food intake could cause weight loss. SML1545 is believed to be useful for the treatment

of type II diabetes. It can cross the blood-brain barrier and is thought to mediate its action through the hypothalamus. The hypothalamus is responsible for maintaining metabolic homeostasis. The claramine is found to be an effective drug against nosocomial diseases resistant bacteria [124], [125]. It appears from this dissertation research that SML1545 possesses also anti-IAV properties.

What is more, interesting properties were shown by SML2238 from the Lopac library (structure: Table 6). In the presented research, the mentioned SM caused the 30-fold viral titer decrease against IAV in MDCK cells. SML2238 is known as causing therapeutic benefits in the reduction of the adverse effect of diabetic retinopathy in animal models. It is characterized as a non-nucleotide-competitive. A tangible ADP-ribosylation factor-6 (ARF6), a selective inhibitor, typifies SML2238 and targets the ARF6 guanine nucleotide exchange factors (GEF) binding region. The described SM prevents GEF-dependent ARF1 & ARF6 activity with higher potency against the Brefeldin A-resistant ArfGEF 2 (BRAG2) than guanine nucleotide exchange factor cytohesin-2 (ARNO)-dependent ARF1 activity [126]–[128].

FID assay showed binding of SML1545 and SML2238 to M1V. The interaction of these SMs with the M1V motif was characterized by molecular docking (Figure 44). In both cases, there are hydrogen bonds in the complex. Hydrogens of the NH₂ group of the SML1545 interact with O4 of the U28 (2.106 Å) and N7 of the A7 (2.306 Å).

SML1545



SML2238

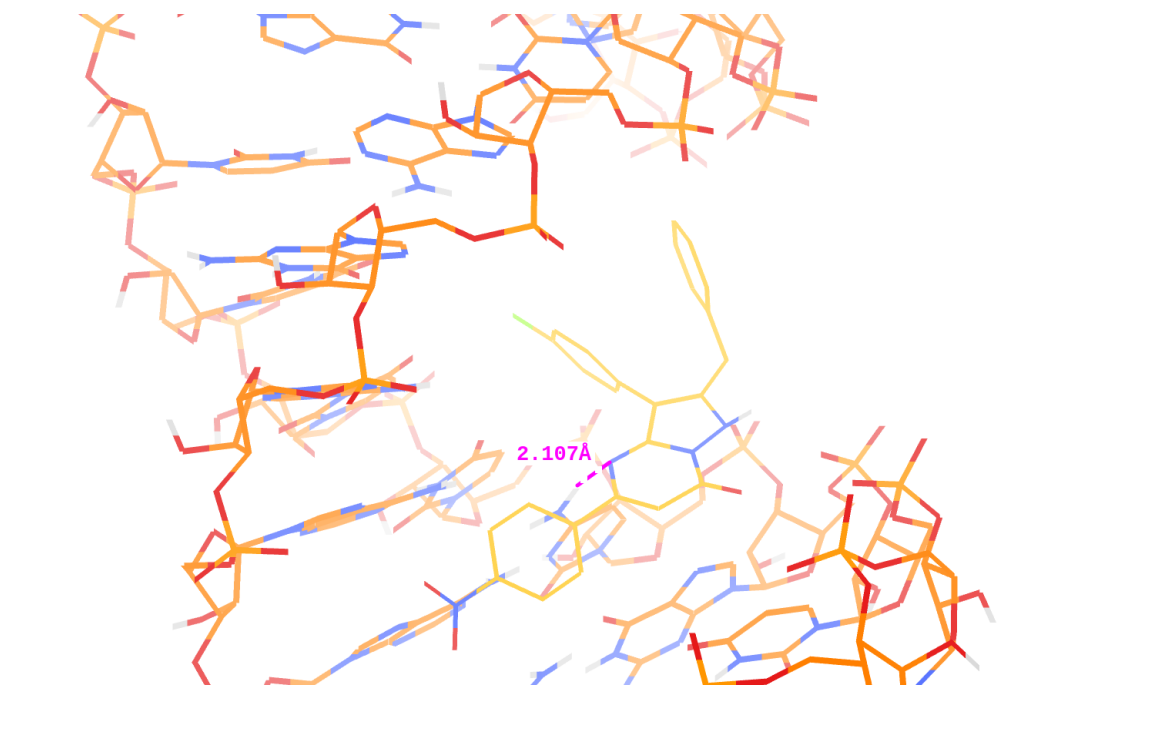


Figure 44. Molecular docking of the SML1545 (purple) and SML2238 (yellow) to the M1V motif. The color of the H-bond is pink.

There was one H-bond detected in the SML2238 complex: nitrogen of the aromatic ring of the SM interacts with H42 of the A25 (2.107 Å). Based on the analyzed data, it can be concluded that both molecular dockings led to a reasonable, thermodynamically stable complex. The values of ΔG are equal -6.2 kcal/mol (SML1545) and -8.4 kcal/mol (SML2238). The M1V is a probable viral target of SML1545 and SML2238 and, by forming a complex, inhibits IAV replication in cells.

B6311 and M4008 mechanism of inhibition of IAV propagation is probably a tight binding to the M4 motif of vRNA8 or M1V, as HTS results suggested. The M4 motif could be a very good target because of its selectivity of binding to SM in contrast to M1V. Finding better SMs targeting the M4 motif would be a promising pathway in antiviral research.

Based on the analysis of the presented research, it is worth taking a closer look at the Z215664726 compound from the Enamine library (structure: Table 10). The compound showed the greatest antiviral properties from the Enamine library in the performed cell experiments against IAV. The Z215664726 caused a decrease of the viral RNA copy number by over 35% compared to the untreated control and a 20-fold viral titer decrease. No published information on the use of this SM was found.

Z215664726 was detected in the FID assay as specific for the H-N1 motif. The interactions of the Z215664726 with the H-N1 motif were visualized and analyzed by molecular docking (Figure 45). In the complex, oxygen of the CO group of the SM creates an H-bond with H41 of the C28820 (2.096 Å). The value of the binding free energy (ΔG) (-6.5 kcal/mol) shows the stability of the complex. Z215664726 is a good candidate for further research against SARS-CoV-2.

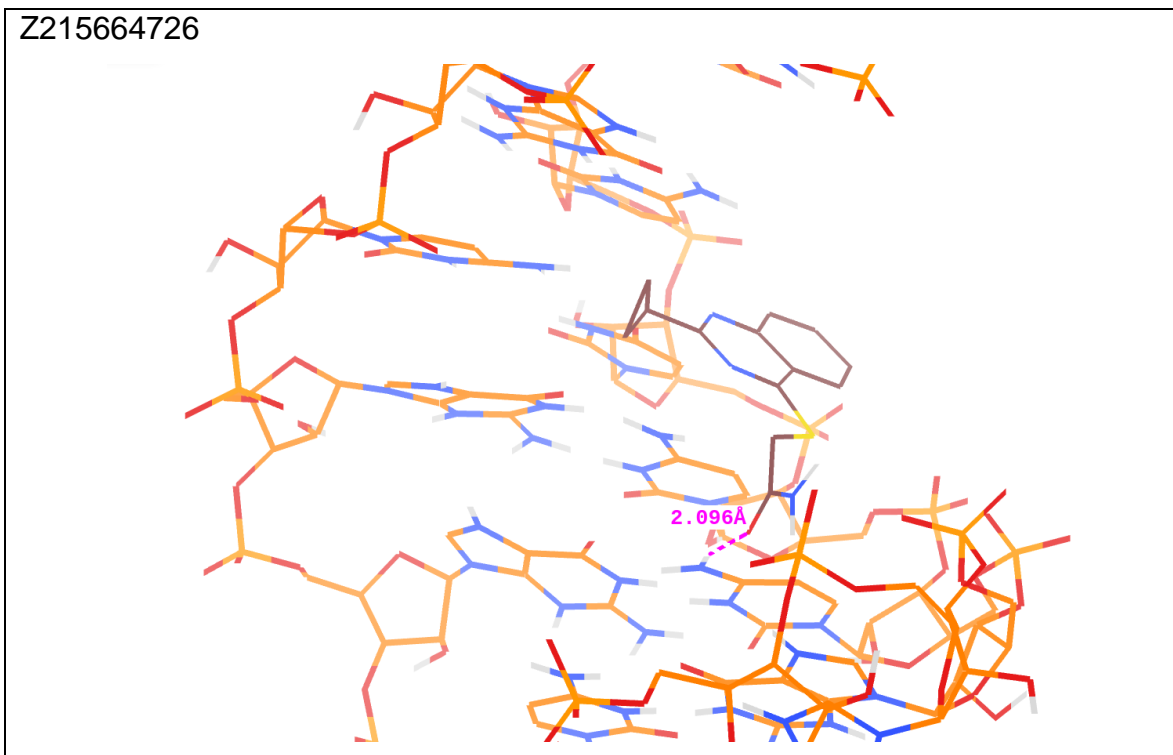


Figure 45. Molecular docking of the Z215664726 (brown) to the H-N1 motif. The color of the H-bond is pink.

Z154467994 and Z134817028 are also promising compounds to test their inhibitory properties against SARS-CoV-2. The support of this conclusion is a tight binding to 3U and H-M1 motifs, respectively, as was shown in HTS. 3U motif has already been proven to be influenced by SM, causing SARS-CoV-2 replication inhibition [122].

The Lopac library has already been used in high-throughput analysis against SARS-CoV-2, while in this work, the target was proteins, not viral RNA [129]. In the cited publication, an attempt was made to select inhibitory compounds for binding of the SARS-CoV-2 receptor binding domain (RBD), which is a part of the viral S protein to human angiotensin-converting enzyme-2 (ACE2). SMs selected as potential inhibitors and binders of the protein do not coincide with those in the submitted dissertation.

Another work using the Lopac library against SARS-CoV-2 also focuses on viral proteins, not vRNA. Tomar et al. tested Lopac library compounds against the binding domain of the spike protein (RDB-S) and ACE2 host cell receptor [130]. The studies carried out were *in silico*, and the selected compounds' binding properties were not

confirmed in the *in vitro* experiment. The identified molecules are hypothesized to assist in controlling the rapid spread of SARS-CoV-2. They could not only inhibit the virus at the entry step but could also act as anti-inflammatory agents, which possibly can impart relief in lung inflammation. The selected compounds in this experiment do not overlap with the chosen compounds in this dissertation.

Desai et al. experimented with the Lopac library and the viral protein (M1) of the IAV [131]. The researchers assumed that impairing the self-association of M1 through a small molecule interaction, which strongly binds to an M1-M1 interface, would result in a new class of anti-influenza agents. Indeed, the selected agent impaired the self-association of M1 through SM and inhibited *in ovo* propagation of multiple IAV strains, including H1N1, pandemic H1N1, H3N2, and H5N1 [131]. The selected compounds in this experiment are not the same as the compounds found in this dissertation.

The Enamine library is a commercial library that is regularly updated by the company, so finding a publication that uses the same set of compounds is impossible. So far, the Enamine library in the high-throughput analysis was used in the virtual screening of novel inhibitors of mycobacterium Z-ring formation to search for new SMs that could affect a cytoskeleton complex playing an important role in sensing the external signals, intracellular transport, and cell division. For this experiment, all Enamine libraries available around the year 2022 were used [132]. Selected in this dissertation, compounds from the Enamine library found as bioactive, and antiviral are unique so far and worth to further study.

An interesting approach to using the research results of the presented dissertation will be the application of chemical modification to promising SMs. It is a natural step in the research pathway that the SMs that represented the best inhibitory character in conducted cell studies are candidates for chemical changes to increase the expected properties, increase the selectivity of the chosen compounds, and improve intracellular transport of the ligand. Certain assumptions of the modified SMs nextly should be verified in cell retests.

There are many possible chemical modifications of small molecules. One of the popular approaches is carbon tail modification, which could be used in the case of SML1545. Based on the molecular docking analysis predictions, it can be assumed that such a modification would increase the strength of the interaction between the ligand and the target binding site in the vRNA. In the case of SML2238, it is worth focusing on the Cl substituent, which could be substituted similarly to the SML1545 compound. In theory, synthesizing several analogs with an increasingly long tail containing NH groups would also allow for more possible interactions. Structural modifications in recent works were based on multiple parameters rather than a single parameter. It avoids sacrificing target activity but also considers more than one criterion.

Very interesting approaches to chemical modification of the SMs were shown in the article by Sun et al. [133] It reviews the improvement in chemical modifications of ligands that penetrate the blood-brain barrier (BBB). They drew several general conclusions that allow for determining the strategy worth adopting for ligands' chemical modifications. To sum up, the careful addition of polar atoms to the structure, breaking the ring system, and attaching long substituents should be carefully considered due to changes in the flexibility of the SM. It would also be worth considering the use of the target vRNA 3D structure that is already proven in MD and the docking of designed modified ligands to compare the binding site and binding affinity, which could help determine the further direction of research. In general, the understanding of the molecular interactions between small molecules and their targets is critical in novel drug discovery. The use of knowledge about the secondary structure of viral RNA, such as IAV and SARS-CoV-2 vRNA, as a first step in searching for specific small molecules, seems to be an effective approach leading to future therapeutics. The present work proved that conserved structural motifs of viral RNA are good targets for RNA-targeted inhibitory strategies. Compared to antisense oligonucleotides, right now, small molecules are considered less cost-effective potential drugs. There is a realistic possibility to find or design a very specific and selective small molecule by targeting the binding pocket

determined by the secondary and tertiary structure of pathogenic RNA. The presented research is at the beginning of this big challenge.

6. MATERIALS AND METHODS

6.1. MATERIALS

6.1.1. Oligonucleotides

Table 18. Oligonucleotides used in experiments performed for the purpose of this work.

Name	Sequence (5`-3`)
RNA used in High throughput Screening (IAV)	
M1V	AGUAGAAACAAGGCUUCGGCCUGCUUUUGCU
M2	GCGAAUCUCUGUAUAUUUUCAGAGACUCGC
M3	GCGCAUAAAUGUUAUUUGUUCGAAACUAUUCUCUGUGC
M4	GCGAAUCUCUUAUAUUUUCAGAGACUCGC
M5	CGCAUUCAAGUCCUCCGAUGAGGACCCCAACUGCG
RNA used in High throughput Screening (SARS-CoV-2)	
U1	CUGUGUGGCUGUCACUCGGCUGCAUGCUUAGUGCACUCACGCA G
N1	CGGAAGACCUUAAAUCCUCGAGGACAAGGCGUUCG
H-M1	UACAAUUUGCCUAUGCCAACAGGAAUAGGUUUUUGUA
H-M2	CGGAGCUGUGAUCCUUCGUGGACAUCUUCG
H-N1	CGGAGCAGAGGCGGCAGUCAAGCCUCUUCUCGUUCG
3U	AACUACAUAGCACAAGUAGAUGUAGUU
U2	ACGUGGCUUUGGAGACUCCGUGGAGGAGGUCUUAUCAGAGGCA CGU
DNA primers for real time qPCR	
vRNA7 forward	TGTTCCATAGCCTTTGCCGT
vRNA7 4 reverse	TGCTGATTCACAGCATCGGT
GAPD H forward	CGGGAACTTGTCATCAAGGG

GAPD H reverse	GCACCAGCATCACCCCATTT
----------------------	----------------------

6.1.2. Commercially available sets:

- LOPAC®¹²⁸⁰ library – purchased 12.16.2020 (LO1280, Sigma),
- Enamine library – purchased 10.22.2020 (Enamine RNA-8960-Y-10 library).

6.1.3. Commercially available sets:

- SuperScript III Reverse Transcriptase (Invitrogen),
- HOT FIREPol Probe qPCR Mix Plus (Solis BioDyne),
- Ambion DNase I RNase-free (Thermo Fisher),
- CellTiter-Glo Luminescent Cell Viability Assay (Promega).

6.1.4. Antibodies:

- mouse anti-influenza primary antibody targeting nucleoprotein (NP) (MAB8257 Merck),
- FITC-conjugated secondary rabbit anti-mouse IgG antibody (AP160F Merck).

6.1.5. Fluorescent dyes:

- TO-PRO™-1 Iodide (515/531) - 1 mM Solution in DMSO (Invitrogen),
- DAPI (4',6-Diamidino-2-phenylindole dihydrochloride), (Invitrogen).

6.1.6. Buffers:

- Screening buffer
 - 8 mM Na₂HPO₄, pH 7.0,
 - 0.185 mM NaCl,
 - 0.1 mM EDTA.

6.1.7. Cell line:

- Madin-Darby Canine Kidney (MDCK) cell line (Sigma Aldrich).

6.1.8. Influenza strain:

- A/California/04/2009 (H1N1) (gift from Professor Luis Martinez-Sobrido, University of Rochester, Rochester, NY, USA).

6.1.9. Cell medium:

- culture medium:
 - 1x Dulbecco's Modified Eagle Medium (DMEM) (4500 mg/l L-glucose, 110 mg/l sodium pyruvate),
 - 10% fetal bovine serum (FBS),
 - 2 mM glutamine,
 - 100 U/ml penicillin,
 - 100 µg/ml streptomycin;

- infectious medium:
 - 1x PBS,
 - 0.3% bovine serum albumin (BSA),
 - 100 U/ml penicillin,
 - 100 µg/ml streptomycin;

- postinfectious medium:
 - 1x DMEM,
 - 0.3% bovine serum albumin (BSA),
 - 100 U/ml penicillin,
 - 100 µg/ml streptomycin,
 - 2 mM glutamine,
 - 1 µg/ml TPCK-treated trypsin;

- Avicel medium:
 - 2/3 postinfectious medium,
 - 1/3 Avicel 3%,
 - 1 µg/ml TPCK-treated trypsin;

- Fix&Perm medium:
 - 1x PBS,
 - Paraformaldehyde 4%,
 - Triton 0.5%;

- blocking buffer:
 - BSA 2%,
 - 1x PBS.

6.2. Methods

6.2.1. Oligonucleotides synthesis

Synthesis of all oligonucleotides was performed using the phosphoramidite method on a solid support. It was supported by the MerMade 12 DNA/RNA synthesizer (BioAutomation) at the Department of Structural Chemistry and Biology of Nucleic Acids IBCH PAS. Commercially available RNA phosphoramidites and controlled pore glass (CPG) supports were used for the synthesis.

6.2.2. RNA deprotection

1.5 ml of 32% ammonia solution and 0.5 ml of 96% ethanol solution were added to the test tube containing CPG with protected oligonucleotide after synthesis. After incubation for 16 hours at 55 °C, samples were cooled at -20 °C for 20 minutes. The supernatant solution was filtered through the column into a new tube and evaporated using a vacuum pump in SpeedVac. 30 µl of dimethylformamide (DMF) and 270 µl of triethylamine trihydrofluoride (TEA3HF) were added to dried samples and incubated at 55 °C for 2 hours. After that time, 4 ml of n-butanol was added to the samples, and precipitation was performed for one h at -20 °C. After drying, the precipitate desalination was carried out using a SEP-PAK column, and the synthesized material was separated by polyacrylamide gel electrophoresis.

6.2.3. RNA elution from polyacrylamide gels

The gel fragments corresponding to the RNA molecules were excised from the gel and transferred to test tubes, where they were dissolved in 0.3 M sodium acetate (pH 5.5). Elution was carried out overnight at 4 °C in a shaking thermoblock. The eluate was transferred to fresh tubes, and ethanol precipitation was performed. The procedure was then repeated twice.

6.2.4. RNA precipitation

The nucleic acid solution was precipitated with three volumes of 96% ethanol at -20 °C for at least 2 hours. After the sample incubation time has elapsed, centrifugation for 30 min at 4 °C and 12,000 rpm. After removing the supernatant, the pellet was washed with 70% ethanol and centrifuged again for 15 min at 4 °C and 12,000 rpm. The supernatant was removed, and the nucleic acid pellet was dried on the bench at room temperature and dissolved in water.

6.2.5. RNA concentration measurement

The concentration of the prepared oligonucleotides was determined by measuring the absorbance at wavelength $\lambda = 260$ nm at Nanodrop2000 (Thermo).

6.2.6. MDCK cell culture

Cells were grown in a culture medium under 5% CO₂ and temperature of 37 °C, humidity 96%, in 100 ml cell culture flasks. Cell passaging was made after the culture reached 80-95% confluence. The procedure begins with double cells washing with 1x PBS solution. Then, 1 ml of trypsin EDTA solution was added, and flasks were transferred to a 37 °C incubator for 10 min. After the incubation time had elapsed, cells were detached from the flask. Then 4 ml of culture medium was added, and the cell aggregates were disrupted and transferred to a falcon tube. The cell suspension was centrifuged for 3 min at 1000 rpm. The supernatant was removed, the pellet was dissolved in a fresh culture medium, and the cell suspension of appropriate density was seeded into a new flask.

6.2.7. IAV infection

160,000 cells/ml of MDCK cells were seeded in 24-well plates. After reaching 80-90% confluency, cells were washed twice with 1x PBS solution. Cells were infected with influenza virus A/California/04/2009 (H1N1) in the infectious medium. The

multiplicity of infection is equal to 0.01. It defines a ratio of infectious particles to infection target – cells. Incubation of cell monolayer in the diluted virus solution in the infectious medium lasted for 1 hour on a gently rocking platform at room temperature. Next, the infectious medium was removed, and the postinfectious medium was added alone or with a small molecule.

6.2.8. Incubation with small molecules

After one hour of infection, the supernatant was removed from the cells. Thereafter, small molecules solution in a postinfectious medium maintaining 0.1% DMSO concentration in each sample was sampled into the cells. Dilutions of selected small molecules were prepared in 3 different concentration variants: 0.1 μM , 1 μM , and 10 μM . Cells were next incubated for 24 hours under 5% CO_2 and temperature of 37 °C and a humidity of 96%. At this time, the supernatant with the grown virus was collected in 96-well plates for Immunofluorescence Focus Formation Assay (IFA), and total RNA was isolated from the cells for qPCR analysis. As a negative control (ctrl-), untreated cells with DMSO were used, and the positive control (ctrl+) were the MDCK cells treated with ribavirin in 40 μM concentration.

6.2.9. Immunofluorescence Focus Formation Assay (IFA)

MDCK cells were seeded at 1×10^5 cells/ml in 96 well plates. Supernatants harvested from the infected cell culture were used to prepare 10-fold serial dilutions of the virus in the infection medium. The cell monolayer in a 96-well plate was infected with serial dilutions of viral supernatants for 1 hour at room temperature in a gently rocking platform. Then, the supernatants were removed, and the cells were kept in an avicel medium for 12 hours at 37 °C in the atmosphere containing 5% CO_2 . After the incubation time had elapsed, the supernatants were removed, and the cells were fixed and permeabilized with Fix&Perm medium for 30 min at room temperature. Blocking was carried out using a blocking buffer for 1 hour at room temperature. Then, the solution was replaced with dissolved mouse primary antibody against

influenza targeting NP protein (MAB8257 Merck) in 1x PBS solution and incubated for 1 hour at room temperature. Detection was performed using a secondary rabbit anti-mouse IgG antibody FITC-conjugated (AP160F Merck) diluted in 1x PBS after 30 min incubation at room temperature. Fluorescence microscopic analysis of the dyeing allowed the calculation of fluorescence units (FFU/ml).

6.2.10. Total RNA isolation

Total RNA from the MDCK cell culture was isolated using the Chomczynski-Sacchi method with the use of Trizol [134]. The quality of the isolated RNA was checked after enzymatic DNA degradation by separation in 1% agarose gel.

6.2.11. DNA enzymatic degradation

500 ng of RNA from isolation with Trizol reagent was treated with Ambion DNase I RNase-free (Thermo Fisher) as recommended by the manufacturer in the buffer supplied with enzyme, at 37 °C for 30 min. The enzyme was inactivated by adding 1 µl of 25 mM EDTA to a final concentration of 2.3 mM and heating at 75°C for 10 min.

6.2.12. Reverse transcription

Reverse transcription was performed with a random hexamer primer and SuperScript reverse transcriptase (Invitrogen). For this purpose, 1 µl of RNA isolate (45 ng) after DNase I treatment was mixed with 1x First-Strand Buffer, a random hexamer primer to give a final concentration of 0.4 µM and water to a final volume of 5 µL and incubated 3 min at 90 °C. After this, 10 min at 55 °C incubation was conducted, and the sample was placed on ice. Thereafter, the mix of 10 mM DTT, 2.5 mM dNTPs, 1x First-Strand Buffer, 10 U of RNase inhibitor rRNasin, 50 U of SuperScript III reverse transcriptase, and water to a final volume of 10 µl was added. Samples were incubated for 50 min at 55 °C. The reaction was stopped by heating at 70 °C for 10 min.

6.2.13. Real-time qPCR with the reference gene

1 µl of each cDNA dilution obtained from RNA from the isolation was amplified in double triplicate in real-time PCR for each pair of starters (Table 18): GAPDH reference gene and vRNA7 primers and 5x Hot Firepol EvaGreen qPCR Mix Plus (no ROX). The amplification took place in parallel. The number of viral RNA copies in each sample was counted.

Reaction for each test sample was performed in double triplicate on the CFX96™ Real-Time System (BioRad) according to the following program: 95 °C for 15 min, 40 cycles 95°C for 15 sec, 60°C for 20 sec, 72 °C for 30 sec. Fluorescence readouts from the plate were taken after each cycle. Relative quantification analysis allowed the comparison of viral RNA copies in the samples treated with inhibitors and controls.

6.2.14. Luminescent Cell Viability Assay

MDCK cells were seeded at 1×10^5 cells/ml in 96 well plates along with the tested compounds. Cells were grown for 48 hours. Celltiter-Glo reagents were added to cell supernatant at a 96-well plate, and after 2 minutes of mixing and 10 minutes of incubation, the solution was transferred to clear bottom plates. The analysis ended up with the measurement of luminescence on the HIDEX microplate reader.

6.2.15. Deterimantion of EC₅₀

The half-maximal effective concentration (EC₅₀) value was calculated to determine the appropriate concentration of the RNA to interact with fluorescent dye TO-PRO-1 Iodide (Invitrogen) for follow-up screening assay. The serial dilutions of RNA were dissolved in the screening buffer and heated in a thermoblock for 5 min at 65°C. After slow cooling on the bench to room temperature for the purpose of folding, bovine serum albumin (BSA, Sigma) was added to the final concentration of 1%.

The RNA solution was combined with 100 μ M TO-PRO-1 Iodide (Invitrogen). After 15 minutes of incubation at room temperature, the solution was transferred to a 384-well plate (Greiner Low-Volume 784076). The measurement was performed (excitation wavelength of 485 nm and an emission wavelength of 528 nm) using a plate reader (CLARIOstar Plus).

6.2.16. Determination of IC₅₀

The half-maximal inhibitory concentration (IC₅₀) was measured to determine the concentration of the control small molecule (6,7-dimethoxy-2-(1-piperaziny)-4-quinazolinamine), where the fluorescent signal was inhibited by half. To perform this process RNA M1V (Table 2) with a concentration resulting from EC₅₀ was diluted in a screening buffer and folded. Thereafter, the solution was cooled down to room temperature, and bovine serum albumin (BSA, Sigma) was added to the final concentration 1%. The RNA solution was next combined with the 100 μ M TO-PRO-1 fluorescent indicator. After 15 minutes of incubation at room temperature, the solution was transferred to a 384-well plate (Greiner Low-Volume 784076). Next, serial dilution of 6,7-dimethoxy-2-(1-piperaziny)-4-quinazolinamine in screening buffer was prepared and added to the mixture. After 15 min of incubation at room temperature, the measurement was performed (excitation wavelength of 485 nm and an emission wavelength of 528 nm) using a plate reader (CLARIOstar Plus).

6.2.17. High throughput screening (HTS)

High throughput screening was performed with the significant participation of the author of this PhD dissertation in collaboration with the High Throughput Screening Laboratory and Laboratory of Molecular Assays of the IBCH PAS.

RNA concentration determined on the basis of EC_{50} was dissolved in the screening buffer and folded in a thermoblock for 5 min at 65 °C. After cooling on the bench top to room temperature, bovine serum albumin (BSA, Sigma) was added to the final concentration 1%.

Small molecule libraries Lopac (Sigma) and Enamine library (Enamine RNA-8960-Y-10 library) were stored in 384 well polypropylene plates at 10 mM concentration in 100% DMSO at -20 C. On the day of the experiment, compound plates were thawed, and the first 1 μ L of each compound was transferred to 384 well intermediate dilution plate containing 9 μ L of assay buffer using a Bravo pipetting station (Agilent). Then, 2 copies of the assay plate were prepared by adding 1 μ L of the diluted compound plate to 384 well black low-volume plates containing 4ul assay buffer per well. 6,7-dimethoxy-2-(1-piperazinyl)-4-quinazolinamine was used as a positive control, and DMSO as a negative control was diluted to a concentration 100 μ M, and 1 μ l of each compound solution was dispensed to the black 384-well plate (Greiner Low-Volume 784076) by automated liquid handling platform Bravo, (Agilent) to achieve final compound concentration 10 mM.

A fluorescent dye TO-PRO-1 Iodide (Invitrogen) was then added to achieve 100 nM final concentration and incubated for 15 min at room temperature. After 15 min of incubation, 10 μ l of the mixture RNA&TO-PRO-1 was dispensed into each well of a black 384-well plate with compounds by Tempest liquid handler (Formulatrix). Next, the measurement was performed (an excitation wavelength of 485 nm and an emission wavelength of 528 nm) using a plate reader (CLARIOstar Plus).

6.2.18. Molecular dynamics

Table 19. Na⁺, Cl⁻ ions, number of water molecules, and box size used in MD for simulated RNA motifs.

RNA motif	Na ⁺	Cl ⁻	Number of water molecules	Box size [Å] [x; y; z]
H-M1	76	40	12 077	[60; 81; 88]
H-M2	57	28	8 415	[59; 79; 64]
N1a	82	45	13 613	[72; 85; 77]
N1b	75	38	11 393	[71; 82; 69]
U1	80	37	11 185	[64; 84; 74]
U2	91	46	13 639	[60; 100; 83]
H-N1	70	34	10184	[56; 86; 72]
3U	55	29	8602	[63; 76; 63]
M4	60	31	9293	[67; 79; 60]

Firstly, each studied RNA motif structure (which are not available as a .pdb file from experimental studies; that means all, besides M1V) was predicted. A .pdb file with an initial tertiary RNA structure was generated based on the secondary structure implemented in RNAComposer. After the 3', and 5'-terminals were marked in the obtained .pdb file, the RNA was prepared for simulation by building the box and adding water and Na⁺ Cl⁻ ions in tleap (AmberTools20), as shown in Table 19.

The minimalization process was performed in 100 000 steps. Next, the thermalization was performed at 310K temperature and constant temperature and constant pressure (NpT) for 1610 ps. The minimization of energy was conducted using a sander. The preparation of the system for MD simulations, as well as minimization, were performed in AmberTools20. System thermalization was performed at a canonical ensemble, where the amount of substance, volume, and

temperature (NVT) are conserved. Equilibration was performed in 4 stages. Brief equilibration was performed in NpT, used for the purpose of reducing water gathering, last 600 ps. Secondly, equilibration in a constant-temperature, a constant-volume ensemble with a gradual reduction of constraints from an initial 20 kcal/mol*Å to close to zero, lasted 600 ps. Next, brief equilibration in 310K and non-constrained NVT, which purpose was to reset the system in NVT completely, lasted 500 ps. The last equilibration was performed in NpT conditions with no constraints and lasted 600 ps. All the above simulation steps were performed using Nanoscale Molecular Dynamics (NAMD) 2.12 with an Amber force field. Finally, the production was made with the prepared system at NAMD software and lasted from 100 to 500 ns, depending on the RNA motif.

6.2.19. Simulated RNA structure clustering

Produced 3D structures were submitted for clustering, and all of the steps described below have been performed in the cpptraj (AmberTools20). The k-mean algorithm was used for analysis. The stimulations were stripped of water and ions. All productions for each structural motif simulation were combined into one file. Each simulated structure received 5 representative and 5 average structures. The representative structures were used for molecular docking.

6.2.20. Molecular docking

As a docking receptor, the RNA structural motifs were used. Final 3D structural models of SARS-CoV-2 RNA motifs (U1, N1, H-M1, H-M2, H-N1, 3U, and U2) were obtained by molecular dynamic simulations and clustering as described above. RNA structure of the M1V motif was downloaded from RCSB Protein Data Bank (PDB: 2LWK).

After devoiding of water and other unusable structures like proteins, certain docking receptors were prepared by a series of steps. After adding hydrogen atoms in VMD software to the structure and transferring the file to a dockable .pdbqt file containing

information about the q charge and t type of the atom, the grid box was prepared in spacing 1.000 Å. The sizes and centers are shown in Table 20.

Table 20. Grid box sizes and centers for RNA motifs in molecular docking.

RNA motif	Grid box size [x; y; z]
M1V	[28; 42; 28]
U1	[28; 44; 48]
N1a	[46; 42; 44]
N1b	[40; 38; 40]
H-M1	[42; 40; 34]
H-M2	[38; 36; 40]
H-N1	[38; 52; 30]
3U	[38; 38; 40]
U2	[52; 60; 36]

Next, using BKChem, the .mol file of each ligand was obtained, and a 3D structure was generated in Open Babel 2.3.2 software or downloaded from the ZINC database and transferred to the dockable file containing information about the q charge and t type of the atom. The preparation of molecules for docking was performed in AutoDock Tools (MGLTools version 1.5.6). The molecular docking process was performed in AutoDock Vina 1.1.2.

7. LIST OF FIGURES AND TABLES

7.1. Figures

Figure 1. Influenza virus replication cycle and genetic reassortment	16
Figure 2. SARS-CoV-2 virus replication cycle	20
Figure 3. Structures of C5, C5-RIBOTAC and C5-Chem-CLIP compounds.....	33
Figure 4. Structure of D01 compound	34
Figure 5. Structures of Huperzine A and ivacaftor.....	35
Figure 6. Structure of merafloxin	35
Figure 7. Scheme of acting of the TO-PRO-1 fluorescent dye in FID assay with an example of an RNA structural motif and a small molecule	43
Figure 8. Structure of the fluorescent dye TO-PRO-1 Iodine.	44
Figure 9. Scheme of steps conducted in HTS.....	45
Figure 10. Structure of reference inhibitor	48
Figure 11. Graphic representation of the primary screening results of Lopac SMs with M1V motif.....	53
Figure 12. Graphic representation of the primary screening results for Lopac SMs with M4 motif.....	55
Figure 13 <i>IC₅₀ curves for selected SMs targeting RNA motifs.....</i>	65
Figure 14. Fluctuation of N1a simulated structure.....	70
Figure 15. Fluctuation of N1b simulated structure.....	71
Figure 16. Molecular docking of the specific Lopac SMs for M1V motif.	75
Figure 17. The binding affinity of specific Lopac SMs for the M1V motif measured in ΔG of the complex.	76
Figure 18. Molecular docking of the specific Lopac SMs for N1a motif.	77
Figure 19. The binding affinity of specific Lopac SMs to the N1a motif measured in ΔG of the complex.....	78
Figure 20. Molecular docking of the specific Lopac SMs for N1b motif.	79
Figure 21. The binding affinity of specific Lopac SMs and the N1b motif measured in ΔG of the complex.	80
Figure 22. Molecular docking of the specific Lopac SMs for U1 motif	81

Figure 23. The binding affinity of specific Lopac SMs for the U1 motif measured in ΔG of the complex.....	82
Figure 24. Molecular docking of the specific Enamine SMs for 3U motif.....	84
Figure 25. The binding affinity of specific Enamine SMs for the 3U motif measured in ΔG of the complex.	85
Figure 26. Molecular docking of the specific Enamine SMs for H-M2 motif	86
Figure 27. The binding affinity of specific Enamine SMs for the H-M2 motif measured in ΔG of the complex.	87
Figure 28. Molecular docking of the Enamine Z1318256185 to the H-N1 motif	88
Figure 29. The binding affinity of the Z1318256185 to the H-N1 motif measured in ΔG of the complex.	89
Figure 30. Molecular docking of the Z48626148 (black) to N1a and N1b motifs ...	89
Figure 31. The binding affinity of the Z48626148 to the N1a and N1b motifs measured in ΔG of the complex.	90
Figure 32. Molecular docking of the Z203972446 to the U2 motif	91
Figure 33. The binding affinity of the Z203972446 to the U2 motif measured in ΔG of the complex.	91
Figure 34. Molecular docking of the SM _{ref} to M1V motif	92
Figure 35. Molecular docking of the SM _{ref} to M1V motif was performed by the author of this dissertation.	93
Figure 36. Viability test results for the MDCK cells treated with Lopac small molecules in three different concentrations	96
Figure 37 Antiviral activity of selected Lopac SMs in the IFA test	98
Figure 38 Fluorescence microscopy images of MDCK cell cultures infected with influenza virus in the IFA assay.....	99
Figure 39. Inhibitory potential of SMs against strain A/California/04/2009 (H1N1) in MDCK cells	100
Figure 40. Viability test results for the MDCK cells treated with Enamine small molecules in three different concentrations	103
Figure 41. Antiviral activity of selected Enamine SMs in the IFA test.....	104

Figure 42 Fluorescence microscopy images of MDCK cell cultures infected with influenza virus in the IFA assay.....	105
Figure 43. Inhibitory potential of Enamine SMs against strain A/California/04/2009 (H1N1) in MDCK cells	106
Figure 44. Molecular docking of the SML1545 and SML2238 to the M1V motif..	113
Figure 45. Molecular docking of the Z215664726 to the H-N1 motif	114

7.2. Tables

Table 1. Structures of SMs with the highest inhibitory activity and low cytotoxicity	32
Table 2. Secondary structures of the selected IAV RNA motifs used in High Throughput Screening and Molecular Docking.	38
Table 3. Secondary structures of the selected SARS-CoV-2 RNA motifs used in High Throughput Screening and Molecular Docking.	40
Table 4. EC ₅₀ values for the RNA structural motifs tested in HTS.....	47
Table 5. Z' factor of HTS for IAV and SARS-CoV-2 RNA motifs.....	49
Table 6. SMs selected in Lopac Library HTS for IAV and SARS-CoV-2 RNA motifs.	51
Table 7. IC ₅₀ values for the selected SMs from the Lopac.	52
Table 8. IC ₅₀ curves for the most selective Lopac compounds for the M1V motif.	54
Table 9. IC ₅₀ curves for the most selective Lopac compounds for the M4 motif....	56
Table 10. IC ₅₀ curves for the most selective Lopac compounds for the N1 motif. .	56
Table 11. SMs selected in Enamine Library HTS for IAV and SARS-CoV-2 RNA motifs.	59
Table 12. IC ₅₀ values for Enamine hits.....	61
Table 13. Structures of N1a and N1b motifs.	68
Table 14. RMSD results for each production of MDS of selected structural motifs.	69
Table 15. Values of DBI, pSF, and frames for clustered motifs of simulated vRNA structures.	72
Table 16. Values of ΔG for H-M2 clusters complexed with ligands.	87

Table 17. Results of relative vRNA copy number reduction for the best LOPAC SMs in RT-qPCR analysis.....	101
Table 18. Oligonucleotides used in experiments performed for the purpose of this work.	118
Table 19. Na ⁺ , Cl ⁻ ions, number of water molecules, and box size used in MD for simulated RNA motifs.....	129
Table 20. Grid box sizes and centers for RNA motifs in molecular docking.	131

8. BIBLIOGRAPHY

- [1] S. Su, X. Fu, G. Li, F. Kerlin, and M. Veit, "Novel Influenza D virus: Epidemiology, pathology, evolution and biological characteristics," *Virulence*, vol. 8, no. 8, pp. 1580–1591, Nov. 2017, doi: 10.1080/21505594.2017.1365216.
- [2] J. Louten, "Influenza Viruses," in *Essential Human Virology*, Elsevier, 2016, pp. 171–191. doi: 10.1016/B978-0-12-800947-5.00010-7.
- [3] N. M. Bouvier and P. Palese, "The biology of influenza viruses," *Vaccine*, vol. 26, pp. D49–D53, Sep. 2008, doi: 10.1016/j.vaccine.2008.07.039.
- [4] K. Asha and B. Kumar, "Emerging Influenza D Virus Threat: What We Know so Far!," *J Clin Med*, vol. 8, no. 2, p. 192, Feb. 2019, doi: 10.3390/jcm8020192.
- [5] A. J. W. te Velhuis and E. Fodor, "Influenza virus RNA polymerase: insights into the mechanisms of viral RNA synthesis," *Nat Rev Microbiol*, vol. 14, no. 8, pp. 479–493, Aug. 2016, doi: 10.1038/nrmicro.2016.87.
- [6] M. I. Nelson and E. C. Holmes, "The evolution of epidemic influenza," *Nature Reviews Genetics*, vol. 8, no. 3, pp. 196–205, Mar. 2007. doi: 10.1038/nrg2053.
- [7] E. G. Brown, "Influenza virus genetics," *Biomedicine & Pharmacotherapy*, vol. 54, no. 4, pp. 196–209, May 2000, doi: 10.1016/S0753-3322(00)89026-5.
- [8] N. Lee, V. Le Sage, A. v. Nanni, D. J. Snyder, V. S. Cooper, and S. S. Lakdawala, "Genome-wide analysis of influenza viral RNA and nucleoprotein association," *Nucleic Acids Res*, vol. 45, no. 15, pp. 8968–8977, Sep. 2017, doi: 10.1093/nar/gkx584.
- [9] H. Ushirogawa *et al.*, "Re-emergence of H3N2 strains carrying potential neutralizing mutations at the N-linked glycosylation site at the hemagglutinin head, post the 2009 H1N1 pandemic," *BMC Infect Dis*, vol. 16, no. 1, p. 380, Dec. 2016, doi: 10.1186/s12879-016-1738-1.
- [10] W. Peng *et al.*, "Recent H3N2 Viruses Have Evolved Specificity for Extended, Branched Human-type Receptors, Conferring Potential for Increased Avidity," *Cell Host Microbe*, vol. 21, no. 1, pp. 23–34, Jan. 2017, doi: 10.1016/j.chom.2016.11.004.
- [11] Z.-Z. Huang, L. Yu, P. Huang, L.-J. Liang, and Q. Guo, "Charged amino acid variability related to N-glyco -sylation and epitopes in A/H3N2 influenza: Hem -agglutinin and neuraminidase," *PLoS One*, vol. 12, no. 7, p. e0178231, Jul. 2017, doi: 10.1371/journal.pone.0178231.

- [12] M. Knossow, R. S. Daniels, A. R. Douglas, J. J. Skehel, and D. C. Wiley, "Three-dimensional structure of an antigenic mutant of the influenza virus haemagglutinin," *Nature*, vol. 311, no. 5987, pp. 678–680, Oct. 1984, doi: 10.1038/311678a0.
- [13] Y. Kawaoka, S. Krauss, and R. G. Webster, "Avian-to-human transmission of the PB1 gene of influenza A viruses in the 1957 and 1968 pandemics," *J Virol*, vol. 63, no. 11, pp. 4603–4608, Nov. 1989, doi: 10.1128/jvi.63.11.4603-4608.1989.
- [14] R. J. Garten *et al.*, "Antigenic and Genetic Characteristics of Swine-Origin 2009 A(H1N1) Influenza Viruses Circulating in Humans," *Science (1979)*, vol. 325, no. 5937, pp. 197–201, Jul. 2009, doi: 10.1126/science.1176225.
- [15] J. Stevens *et al.*, "Glycan Microarray Analysis of the Hemagglutinins from Modern and Pandemic Influenza Viruses Reveals Different Receptor Specificities," *J Mol Biol*, vol. 355, no. 5, pp. 1143–1155, Feb. 2006, doi: 10.1016/j.jmb.2005.11.002.
- [16] G. N. Rogers and J. C. Paulson, "Receptor determinants of human and animal influenza virus isolates: Differences in receptor specificity of the H3 hemagglutinin based on species of origin," *Virology*, vol. 127, no. 2, pp. 361–373, Jun. 1983, doi: 10.1016/0042-6822(83)90150-2.
- [17] W. Zheng and Y. J. Tao, "Structure and assembly of the influenza A virus ribonucleoprotein complex," *FEBS Lett*, vol. 587, no. 8, pp. 1206–1214, Apr. 2013, doi: 10.1016/j.febslet.2013.02.048.
- [18] H. Zhang, B. Hale, K. Xu, and B. Sun, "Viral and Host Factors Required for Avian H5N1 Influenza A Virus Replication in Mammalian Cells," *Viruses*, vol. 5, no. 6, pp. 1431–1446, Jun. 2013, doi: 10.3390/v5061431.
- [19] B. Hu, H. Guo, P. Zhou, and Z.-L. Shi, "Characteristics of SARS-CoV-2 and COVID-19," *Nat Rev Microbiol*, vol. 19, no. 3, pp. 141–154, Mar. 2021, doi: 10.1038/s41579-020-00459-7.
- [20] P. Bonilauri and G. Rugna, "Animal Coronaviruses and SARS-COV-2 in Animals, What Do We Actually Know?," *Life*, vol. 11, no. 2, p. 123, Feb. 2021, doi: 10.3390/life11020123.
- [21] S. Payne, "Family Coronaviridae," in *Viruses*, Elsevier, 2017, pp. 149–158. doi: 10.1016/B978-0-12-803109-4.00017-9.
- [22] M. Pustake, I. Tambolkar, P. Giri, and C. Gandhi, "SARS, MERS and CoVID-19: An overview and comparison of clinical, laboratory and radiological features," *J Family Med Prim Care*, vol. 11, no. 1, p. 10, 2022, doi: 10.4103/jfmpc.jfmpc_839_21.

- [23] Y. Yang *et al.*, “The deadly coronaviruses: The 2003 SARS pandemic and the 2020 novel coronavirus epidemic in China,” *J Autoimmun*, vol. 109, p. 102434, May 2020, doi: 10.1016/j.jaut.2020.102434.
- [24] S. Ludwig and A. Zarbock, “Coronaviruses and SARS-CoV-2: A Brief Overview,” *Anesth Analg*, vol. 131, no. 1, pp. 93–96, Jul. 2020, doi: 10.1213/ANE.0000000000004845.
- [25] M. F. Boni *et al.*, “Evolutionary origins of the SARS-CoV-2 sarbecovirus lineage responsible for the COVID-19 pandemic,” *Nat Microbiol*, vol. 5, no. 11, pp. 1408–1417, Jul. 2020, doi: 10.1038/s41564-020-0771-4.
- [26] P. Antony and R. Vijayan, “Role of SARS-CoV-2 and ACE2 variations in COVID-19,” *Biomed J*, vol. 44, no. 3, pp. 235–244, Jun. 2021, doi: 10.1016/j.bj.2021.04.006.
- [27] R. Gorkhali, P. Koirala, S. Rijal, A. Mainali, A. Baral, and H. K. Bhattarai, “Structure and Function of Major SARS-CoV-2 and SARS-CoV Proteins,” *Bioinform Biol Insights*, vol. 15, p. 117793222110258, Jan. 2021, doi: 10.1177/11779322211025876.
- [28] T. C. T. Lan *et al.*, “Secondary structural ensembles of the SARS-CoV-2 RNA genome in infected cells,” *Nat Commun*, vol. 13, no. 1, p. 1128, Mar. 2022, doi: 10.1038/s41467-022-28603-2.
- [29] J. Piasecka, A. Jarmolowicz, and E. Kierzek, “Organization of the Influenza A Virus Genomic RNA in the Viral Replication Cycle—Structure, Interactions, and Implications for the Emergence of New Strains,” *Pathogens*, vol. 9, no. 11, p. 951, Nov. 2020, doi: 10.3390/pathogens9110951.
- [30] C. B. Jackson, M. Farzan, B. Chen, and H. Choe, “Mechanisms of SARS-CoV-2 entry into cells,” *Nature Reviews Molecular Cell Biology*, vol. 23, no. 1. Nature Research, pp. 3–20, Jan. 01, 2022. doi: 10.1038/s41580-021-00418-x.
- [31] R. Piyush, K. Rajarshi, A. Chatterjee, R. Khan, and S. Ray, “Nucleic acid-based therapy for coronavirus disease 2019,” *Heliyon*, vol. 6, no. 9, p. e05007, Sep. 2020, doi: 10.1016/j.heliyon.2020.e05007.
- [32] W. Y. Tarn, Y. Cheng, S. H. Ko, and L. M. Huang, “Antisense oligonucleotide-based therapy of viral infections,” *Pharmaceutics*, vol. 13, no. 12, Dec. 2021, doi: 10.3390/pharmaceutics13122015.
- [33] G. Kher, S. Trehan, and A. Misra, “Antisense Oligonucleotides and RNA Interference,” in *Challenges in Delivery of Therapeutic Genomics and Proteomics*, Elsevier, 2011, pp. 325–386. doi: 10.1016/B978-0-12-384964-9.00007-4.

- [34] A. Zerial, N. T. Thuong, and C. H el ene, "Selective inhibition of the cytopathic effect of type A influenza viruses by oligodeoxynucleotides covalently linked to an intercalating agent," *Nucleic Acids Res*, vol. 15, no. 23, pp. 9909–9919, 1987, doi: 10.1093/nar/15.23.9909.
- [35] P. Kumar, B. Kumar, R. Rajput, L. Saxena, A. C. Banerjea, and M. Khanna, "Cross-Protective Effect of Antisense Oligonucleotide Developed Against the Common 3' NCR of Influenza A Virus Genome," *Mol Biotechnol*, vol. 55, no. 3, pp. 203–211, Nov. 2013, doi: 10.1007/s12033-013-9670-8.
- [36] M. Duan, Z. Zhou, R.-X. Lin, J. Yang, X.-Z. Xia, and S.-Q. Wang, "In vitro and in vivo Protection against the Highly Pathogenic H5N1 Influenza virus by an Antisense Phosphorothioate Oligonucleotide," *Antivir Ther*, vol. 13, no. 1, pp. 109–114, Jan. 2008, doi: 10.1177/135965350801300112.
- [37] J. M. Leiter, S. Agrawal, P. Palese, and P. C. Zamecnik, "Inhibition of influenza virus replication by phosphorothioate oligodeoxynucleotides.," *Proceedings of the National Academy of Sciences*, vol. 87, no. 9, pp. 3430–3434, May 1990, doi: 10.1073/pnas.87.9.3430.
- [38] A. v. Kabanov *et al.*, "A new class of antivirals: antisense oligonucleotides combined with a hydrophobic substituent effectively inhibit influenza virus reproduction and synthesis of virus-specific proteins in MDCK cells," *FEBS Lett*, vol. 259, no. 2, pp. 327–330, Jan. 1990, doi: 10.1016/0014-5793(90)80039-L.
- [39] Y. Wu *et al.*, "Inhibition of highly pathogenic avian H5N1 influenza virus replication by RNA oligonucleotides targeting NS1 gene," *Biochem Biophys Res Commun*, vol. 365, no. 2, pp. 369–374, Jan. 2008, doi: 10.1016/j.bbrc.2007.10.196.
- [40] G. Gabriel, A. Nordmann, D. A. Stein, P. L. Iversen, and H.-D. Klenk, "Morpholino oligomers targeting the PB1 and NP genes enhance the survival of mice infected with highly pathogenic influenza A H7N7 virus," *Journal of General Virology*, vol. 89, no. 4, pp. 939–948, Apr. 2008, doi: 10.1099/vir.0.83449-0.
- [41] E. Lenartowicz, A. Nogales, E. Kierzek, R. Kierzek, L. Mart inez-Sobrido, and D. H. Turner, "Antisense Oligonucleotides Targeting Influenza A Segment 8 Genomic RNA Inhibit Viral Replication," *Nucleic Acid Ther*, vol. 26, no. 5, pp. 277–285, Oct. 2016, doi: 10.1089/nat.2016.0619.
- [42] M. Duan, Z. Zhou, R.-X. Lin, J. Yang, X.-Z. Xia, and S.-Q. Wang, "In vitro and in vivo protection against the highly pathogenic H5N1 influenza virus by an antisense phosphorothioate oligonucleotide.," *Antivir Ther*, vol. 13, no. 1, pp. 109–14, 2008.

- [43] S. Giannecchini, V. Clausi, D. Nosi, and A. Azzi, "Oligonucleotides derived from the packaging signal at the 5' end of the viral PB2 segment specifically inhibit influenza virus in vitro," *Arch Virol*, vol. 154, no. 5, pp. 821–832, May 2009, doi: 10.1007/s00705-009-0380-2.
- [44] P. Michalak *et al.*, "Secondary structure of the segment 5 genomic RNA of influenza A virus and its application for designing antisense oligonucleotides," *Sci Rep*, vol. 9, no. 1, p. 3801, Dec. 2019, doi: 10.1038/s41598-019-40443-7.
- [45] M. Soszynska-Jozwiak, P. Michalak, W. N. Moss, R. Kierzek, J. Keszy, and E. Kierzek, "Influenza virus segment 5 (+)RNA - secondary structure and new targets for antiviral strategies," *Sci Rep*, vol. 7, no. 1, p. 15041, Dec. 2017, doi: 10.1038/s41598-017-15317-5.
- [46] M. Soszynska-Jozwiak, P. Michalak, W. N. Moss, R. Kierzek, and E. Kierzek, "A Conserved Secondary Structural Element in the Coding Region of the Influenza A Virus Nucleoprotein (NP) mRNA Is Important for the Regulation of Viral Proliferation," *PLoS One*, vol. 10, no. 10, p. e0141132, Oct. 2015, doi: 10.1371/journal.pone.0141132.
- [47] R. J. Hagey *et al.*, "Programmable antivirals targeting critical conserved viral RNA secondary structures from influenza A virus and SARS-CoV-2," *Nat Med*, vol. 28, no. 9, pp. 1944–1955, Sep. 2022, doi: 10.1038/s41591-022-01908-x.
- [48] A. M. Quemener and M. D. Galibert, "Antisense oligonucleotide: A promising therapeutic option to beat COVID-19," *Wiley Interdiscip Rev RNA*, vol. 13, no. 4, Jul. 2022, doi: 10.1002/wrna.1703.
- [49] V. Lulla *et al.*, "Targeting the Conserved Stem Loop 2 Motif in the SARS-CoV-2 Genome," *J Virol*, vol. 95, no. 14, Jun. 2021, doi: 10.1128/JVI.00663-21.
- [50] A. Fire, S. Xu, M. K. Montgomery, S. A. Kostas, S. E. Driver, and C. C. Mello, "Potent and specific genetic interference by double-stranded RNA in *Caenorhabditis elegans*," *Nature*, vol. 391, no. 6669, pp. 806–811, Feb. 1998, doi: 10.1038/35888.
- [51] B. Nawrot and K. Sipa, "Chemical and Structural Diversity of siRNA Molecules," *Curr Top Med Chem*, vol. 6, no. 9, pp. 913–925, May 2006, doi: 10.2174/156802606777303658.
- [52] S. M. Elbashir, J. Harborth, W. Lendeckel, A. Yalcin, K. Weber, and T. Tuschl, "Duplexes of 21-nucleotide RNAs mediate RNA interference in cultured mammalian cells," *Nature*, vol. 411, no. 6836, pp. 494–498, May 2001, doi: 10.1038/35078107.

- [53] A. Dias *et al.*, “The cap-snatching endonuclease of influenza virus polymerase resides in the PA subunit,” *Nature*, vol. 458, no. 7240, pp. 914–918, Apr. 2009, doi: 10.1038/nature07745.
- [54] P. Yuan *et al.*, “Crystal structure of an avian influenza polymerase PAN reveals an endonuclease active site,” *Nature*, vol. 458, no. 7240, pp. 909–913, Apr. 2009, doi: 10.1038/nature07720.
- [55] Y. Wu *et al.*, “Inhibition of highly pathogenic avian H5N1 influenza virus replication by RNA oligonucleotides targeting NS1 gene,” *Biochem Biophys Res Commun*, vol. 365, no. 2, pp. 369–374, Jan. 2008, doi: 10.1016/j.bbrc.2007.10.196.
- [56] J. Piasecka, E. Lenartowicz, M. Soszynska-Jozwiak, B. Szutkowska, R. Kierzek, and E. Kierzek, “RNA Secondary Structure Motifs of the Influenza A Virus as Targets for siRNA-Mediated RNA Interference,” *Mol Ther Nucleic Acids*, vol. 19, pp. 627–642, Mar. 2020, doi: 10.1016/j.omtn.2019.12.018.
- [57] M. Jiang *et al.*, “Efficient Inhibition of Avian and Seasonal Influenza A Viruses by a Virus-Specific Dicer-Substrate Small Interfering RNA Swarm in Human Monocyte-Derived Macrophages and Dendritic Cells,” *J Virol*, vol. 93, no. 4, Feb. 2019, doi: 10.1128/JVI.01916-18.
- [58] S. Djebali *et al.*, “Landscape of transcription in human cells,” *Nature*, vol. 489, no. 7414, pp. 101–108, Sep. 2012, doi: 10.1038/nature11233.
- [59] N. M. Snead *et al.*, “Molecular basis for improved gene silencing by Dicer substrate interfering RNA compared with other siRNA variants,” *Nucleic Acids Res*, vol. 41, no. 12, pp. 6209–6221, Jul. 2013, doi: 10.1093/nar/gkt200.
- [60] I. Niktab, M. Haghparast, M.-H. Beigi, T. L. Megraw, A. Kiani, and K. Ghaedi, “Design of advanced siRNA therapeutics for the treatment of COVID-19,” *Meta Gene*, vol. 29, p. 100910, Sep. 2021, doi: 10.1016/j.mgene.2021.100910.
- [61] A. Idris *et al.*, “A SARS-CoV-2 targeted siRNA-nanoparticle therapy for COVID-19,” *Molecular Therapy*, vol. 29, no. 7, pp. 2219–2226, Jul. 2021, doi: 10.1016/j.ymthe.2021.05.004.
- [62] S. Siddiquee, “A Review of Peptide Nucleic Acid,” *Adv Tech Biol Med*, vol. 03, no. 02, 2015, doi: 10.4172/2379-1764.1000131.
- [63] E. Rozners, “Recent Advances in Chemical Modification of Peptide Nucleic Acids,” *J Nucleic Acids*, vol. 2012, pp. 1–8, 2012, doi: 10.1155/2012/518162.
- [64] D.-F. K. Toh *et al.*, “Incorporating a guanidine-modified cytosine base into triplex-forming PNAs for the recognition of a C-G pyrimidine–purine inversion

- site of an RNA duplex,” *Nucleic Acids Res*, p. gkw778, Sep. 2016, doi: 10.1093/nar/gkw778.
- [65] M. Szabat, E. Kierzek, and R. Kierzek, “Modified RNA triplexes: Thermodynamics, structure and biological potential,” *Sci Rep*, vol. 8, no. 1, Dec. 2018, doi: 10.1038/s41598-018-31387-5.
- [66] M. Li, T. Zengaya, and E. Rozners, “Short Peptide Nucleic Acids Bind Strongly to Homopurine Tract of Double Helical RNA at pH 5.5,” *J Am Chem Soc*, vol. 132, no. 25, pp. 8676–8681, Jun. 2010, doi: 10.1021/ja101384k.
- [67] T. Bentin, G. I. Hansen, and P. E. Nielsen, “Structural diversity of target-specific homopyrimidine peptide nucleic acid–dsDNA complexes,” *Nucleic Acids Res*, vol. 34, no. 20, pp. 5790–5799, Nov. 2006, doi: 10.1093/nar/gkl736.
- [68] A. Goldbech Olsen, O. Dahl, and P. E. Nielsen, “A Novel PNA-Monomer for Recognition of Thymine in Triple-Helix Structures,” *Nucleosides Nucleotides Nucleic Acids*, vol. 22, no. 5–8, pp. 1331–1333, Oct. 2003, doi: 10.1081/NCN-120022958.
- [69] M. Egholm *et al.*, “PNA hybridizes to complementary oligonucleotides obeying the Watson–Crick hydrogen-bonding rules,” *Nature*, vol. 365, no. 6446, pp. 566–568, Oct. 1993, doi: 10.1038/365566a0.
- [70] J. Kesý *et al.*, “A Short Chemically Modified dsRNA-Binding PNA (dbPNA) Inhibits Influenza Viral Replication by Targeting Viral RNA Panhandle Structure,” *Bioconjug Chem*, vol. 30, no. 3, pp. 931–943, Mar. 2019, doi: 10.1021/acs.bioconjchem.9b00039.
- [71] K. Rosenke *et al.*, “Inhibition of SARS-CoV-2 in Vero cell cultures by peptide-conjugated morpholino oligomers,” *Journal of Antimicrobial Chemotherapy*, vol. 76, no. 2, pp. 413–417, Jan. 2021, doi: 10.1093/jac/dkaa460.
- [72] C. Li *et al.*, “Automated Flow Synthesis of Peptide–PNA Conjugates,” *ACS Cent Sci*, vol. 8, no. 2, pp. 205–213, Feb. 2022, doi: 10.1021/acscentsci.1c01019.
- [73] C. A. Lipinski, “Drug-like properties and the causes of poor solubility and poor permeability,” *J Pharmacol Toxicol Methods*, vol. 44, no. 1, pp. 235–249, Jul. 2000, doi: 10.1016/S1056-8719(00)00107-6.
- [74] W. P. Walters and M. A. Murcko, “Prediction of ‘drug-likeness,’” *Adv Drug Deliv Rev*, vol. 54, no. 3, pp. 255–271, Mar. 2002, doi: 10.1016/S0169-409X(02)00003-0.
- [75] “70dc46dc-896a-42b7-8f63-4e906f59a228”.

- [76] J. Bolleddula *et al.*, “Absorption, Distribution, Metabolism, and Excretion of Therapeutic Proteins: Current Industry Practices and Future Perspectives,” *Drug Metabolism and Disposition*, vol. 50, no. 6, pp. 837–845, Jun. 2022, doi: 10.1124/dmd.121.000461.
- [77] P. B. Dervan, “Design of Sequence-Specific DNA-Binding Molecules,” *Science* (1979), vol. 232, no. 4749, pp. 464–471, Apr. 1986, doi: 10.1126/science.2421408.
- [78] O. Fedorova, G. E. Jagdmann, R. L. Adams, L. Yuan, M. C. van Zandt, and A. M. Pyle, “Small molecules that target group II introns are potent antifungal agents,” *Nat Chem Biol*, vol. 14, no. 12, pp. 1073–1078, Dec. 2018, doi: 10.1038/s41589-018-0142-0.
- [79] K. D. Warner, C. E. Hajdin, and K. M. Weeks, “Principles for targeting RNA with drug-like small molecules,” *Nat Rev Drug Discov*, vol. 17, no. 8, pp. 547–558, Aug. 2018, doi: 10.1038/nrd.2018.93.
- [80] A. E. Hargrove, “Small molecule–RNA targeting: starting with the fundamentals,” *Chemical Communications*, vol. 56, no. 94, pp. 14744–14756, 2020, doi: 10.1039/D0CC06796B.
- [81] A. Ursu *et al.*, “Design of small molecules targeting RNA structure from sequence,” *Chem Soc Rev*, vol. 49, no. 20, pp. 7252–7270, 2020, doi: 10.1039/D0CS00455C.
- [82] M.-K. Lee *et al.*, “A novel small-molecule binds to the influenza A virus RNA promoter and inhibits viral replication,” *Chem. Commun.*, vol. 50, no. 3, pp. 368–370, 2014, doi: 10.1039/C3CC46973E.
- [83] A. Bottini, S. K. De, B. Wu, C. Tang, G. Varani, and M. Pellecchia, “Targeting Influenza A Virus RNA Promoter,” *Chem Biol Drug Des*, vol. 86, no. 4, pp. 663–673, Oct. 2015, doi: 10.1111/cbdd.12534.
- [84] H. S. Haniff *et al.*, “Targeting the SARS-CoV-2 RNA Genome with Small Molecule Binders and Ribonuclease Targeting Chimera (RIBOTAC) Degradable,” *ACS Cent Sci*, vol. 6, no. 10, pp. 1713–1721, Oct. 2020, doi: 10.1021/acscentsci.0c00984.
- [85] S. Sreeramulu *et al.*, “Exploring the Druggability of Conserved RNA Regulatory Elements in the SARS-CoV-2 Genome,” *Angewandte Chemie International Edition*, vol. 60, no. 35, pp. 19191–19200, Aug. 2021, doi: 10.1002/anie.202103693.
- [86] X. Su *et al.*, “Efficient Inhibition of SARS-CoV-2 Using Chimeric Antisense Oligonucleotides through RNase L Activation**,” *Angewandte Chemie International Edition*, vol. 60, no. 40, pp. 21662–21667, Sep. 2021, doi: 10.1002/anie.202105942.

- [87] Y. Sun *et al.*, “Restriction of SARS-CoV-2 replication by targeting programmed –1 ribosomal frameshifting,” *Proceedings of the National Academy of Sciences*, vol. 118, no. 26, Jun. 2021, doi: 10.1073/pnas.2023051118.
- [88] E. Fodor, D. C. Pritlove, and G. G. Brownlee, “The influenza virus panhandle is involved in the initiation of transcription,” *J Virol*, vol. 68, no. 6, pp. 4092–4096, Jun. 1994, doi: 10.1128/jvi.68.6.4092-4096.1994.
- [89] B. Dadonaite *et al.*, “The structure of the influenza A virus genome,” *Nat Microbiol*, vol. 4, no. 11, pp. 1781–1789, Jul. 2019, doi: 10.1038/s41564-019-0513-7.
- [90] M.-K. Lee *et al.*, “A novel small-molecule binds to the influenza A virus RNA promoter and inhibits viral replication,” *Chem. Commun.*, vol. 50, no. 3, pp. 368–370, 2014, doi: 10.1039/C3CC46973E.
- [91] E. Lenartowicz *et al.*, “Self-Folding of Naked Segment 8 Genomic RNA of Influenza A Virus,” *PLoS One*, vol. 11, no. 2, p. e0148281, Feb. 2016, doi: 10.1371/journal.pone.0148281.
- [92] I. Manfredonia *et al.*, “Genome-wide mapping of SARS-CoV-2 RNA structures identifies therapeutically-relevant elements,” *Nucleic Acids Res*, vol. 48, no. 22, pp. 12436–12452, Dec. 2020, doi: 10.1093/nar/gkaa1053.
- [93] S.-C. Chen and R. C. L. Olsthoorn, “Group-specific structural features of the 5′-proximal sequences of coronavirus genomic RNAs,” *Virology*, vol. 401, no. 1, pp. 29–41, May 2010, doi: 10.1016/j.virol.2010.02.007.
- [94] N. J. Hardenbrook and P. Zhang, “A structural view of the SARS-CoV-2 virus and its assembly,” *Curr Opin Virol*, vol. 52, pp. 123–134, Feb. 2022, doi: 10.1016/j.coviro.2021.11.011.
- [95] D. Yang and J. L. Leibowitz, “The structure and functions of coronavirus genomic 3′ and 5′ ends,” *Virus Res*, vol. 206, pp. 120–133, Aug. 2015, doi: 10.1016/j.virusres.2015.02.025.
- [96] N. C. Huston, H. Wan, R. de Cesaris Araujo Tavares, C. Wilen, and A. M. Pyle, “Comprehensive in-vivo secondary structure of the SARS-CoV-2 genome reveals novel regulatory motifs and mechanisms,” *bioRxiv*, Jul. 2020, doi: 10.1101/2020.07.10.197079.
- [97] C. Cao *et al.*, “The architecture of the SARS-CoV-2 RNA genome inside virion,” *Nat Commun*, vol. 12, no. 1, p. 3917, Jun. 2021, doi: 10.1038/s41467-021-22785-x.

- [98] J. Zhao, J. Qiu, S. Aryal, J. Hackett, and J. Wang, "The RNA Architecture of the SARS-CoV-2 3'-Untranslated Region," *Viruses*, vol. 12, no. 12, p. 1473, Dec. 2020, doi: 10.3390/v12121473.
- [99] P. N. Asare-Okai and C. S. Chow, "A modified fluorescent intercalator displacement assay for RNA ligand discovery," *Anal Biochem*, vol. 408, no. 2, pp. 269–276, Jan. 2011, doi: 10.1016/j.ab.2010.09.020.
- [100] T. Tran and M. D. Disney, "Identifying the preferred RNA motifs and chemotypes that interact by probing millions of combinations," *Nat Commun*, vol. 3, no. 1, p. 1125, Jan. 2012, doi: 10.1038/ncomms2119.
- [101] J.-H. Zhang, T. D. Y. Chung, and K. R. Oldenburg, "A Simple Statistical Parameter for Use in Evaluation and Validation of High Throughput Screening Assays," *SLAS Discovery*, vol. 4, no. 2, pp. 67–73, Apr. 1999, doi: 10.1177/108705719900400206.
- [102] A. Birmingham *et al.*, "Statistical methods for analysis of high-throughput RNA interference screens," *Nat Methods*, vol. 6, no. 8, pp. 569–575, Aug. 2009, doi: 10.1038/nmeth.1351.
- [103] S. Goodwin, G. Shahtahmassebi, and Q. S. Hanley, "Statistical models for identifying frequent hitters in high throughput screening," *Sci Rep*, vol. 10, no. 1, p. 17200, Oct. 2020, doi: 10.1038/s41598-020-74139-0.
- [104] I. Kufareva and R. Abagyan, "Methods of Protein Structure Comparison," 2011, pp. 231–257. doi: 10.1007/978-1-61779-588-6_10.
- [105] A. Zemla, "LGA: a method for finding 3D similarities in protein structures," *Nucleic Acids Res*, vol. 31, no. 13, pp. 3370–3374, Jul. 2003, doi: 10.1093/nar/gkg571.
- [106] C. E. Hajdin, F. Ding, N. v. Dokholyan, and K. M. Weeks, "On the significance of an RNA tertiary structure prediction," *RNA*, vol. 16, no. 7, pp. 1340–1349, Jul. 2010, doi: 10.1261/rna.1837410.
- [107] W. Humphrey, A. Dalke, and K. Schulten, "VMD: Visual molecular dynamics," *J Mol Graph*, vol. 14, no. 1, pp. 33–38, Feb. 1996, doi: 10.1016/0263-7855(96)00018-5.
- [108] O. Keskin, R. L. Jernigan, and I. Bahar, "Proteins with Similar Architecture Exhibit Similar Large-Scale Dynamic Behavior," *Biophys J*, vol. 78, no. 4, pp. 2093–2106, Apr. 2000, doi: 10.1016/S0006-3495(00)76756-7.
- [109] S. Chang, D.-W. Zhang, L. Xu, H. Wan, T.-J. Hou, and R. Kong, "Exploring the molecular basis of RNA recognition by the dimeric RNA-binding protein via molecular simulation methods," *RNA Biol*, vol. 13, no. 11, pp. 1133–1143, Nov. 2016, doi: 10.1080/15476286.2016.1223007.

- [110] J. Peng, W. Wang, Y. Yu, H. Gu, and X. Huang, "Clustering algorithms to analyze molecular dynamics simulation trajectories for complex chemical and biological systems," *Chinese Journal of Chemical Physics*, vol. 31, no. 4, pp. 404–420, Aug. 2018, doi: 10.1063/1674-0068/31/cjcp1806147.
- [111] J. Shao, S. W. Tanner, N. Thompson, and T. E. Cheatham, "Clustering Molecular Dynamics Trajectories: 1. Characterizing the Performance of Different Clustering Algorithms," *J Chem Theory Comput*, vol. 3, no. 6, pp. 2312–2334, Nov. 2007, doi: 10.1021/ct700119m.
- [112] T. Caliński and J. Harabasz, "A dendrite method for cluster analysis," *Commun Stat*, vol. 3, pp. 1–27, 1974.
- [113] D. L. Davies and D. W. Bouldin, "A Cluster Separation Measure," *IEEE Trans Pattern Anal Mach Intell*, vol. PAMI-1, no. 2, pp. 224–227, Apr. 1979, doi: 10.1109/TPAMI.1979.4766909.
- [114] J. C. Rojas Thomas, M. S. Penas, and M. Mora, "New Version of Davies-Bouldin Index for Clustering Validation Based on Cylindrical Distance," in *2013 32nd International Conference of the Chilean Computer Science Society (SCCC)*, Nov. 2013, pp. 49–53. doi: 10.1109/SCCC.2013.29.
- [115] J. Shao, S. W. Tanner, N. Thompson, and T. E. Cheatham, "Clustering Molecular Dynamics Trajectories: 1. Characterizing the Performance of Different Clustering Algorithms," *J Chem Theory Comput*, vol. 3, no. 6, pp. 2312–2334, Nov. 2007, doi: 10.1021/ct700119m.
- [116] G. M. Morris *et al.*, "AutoDock4 and AutoDockTools4: Automated docking with selective receptor flexibility," *J Comput Chem*, vol. 30, no. 16, pp. 2785–2791, Dec. 2009, doi: 10.1002/jcc.21256.
- [117] O. Trott and A. J. Olson, "AutoDock Vina: Improving the speed and accuracy of docking with a new scoring function, efficient optimization, and multithreading," *J Comput Chem*, p. NA-NA, 2009, doi: 10.1002/jcc.21334.
- [118] J. Eberhardt, D. Santos-Martins, A. F. Tillack, and S. Forli, "AutoDock Vina 1.2.0: New Docking Methods, Expanded Force Field, and Python Bindings," *J Chem Inf Model*, vol. 61, no. 8, pp. 3891–3898, Aug. 2021, doi: 10.1021/acs.jcim.1c00203.
- [119] E. F. Pettersen *et al.*, "UCSF Chimera?A visualization system for exploratory research and analysis," *J Comput Chem*, vol. 25, no. 13, pp. 1605–1612, Oct. 2004, doi: 10.1002/jcc.20084.
- [120] "Schrodinger Release 2022-3: Maestro, Schrodinger, LLC, New York, NY, 2021," 2021.

- [121] E. Lenartowicz, A. Nogales, E. Kierzek, R. Kierzek, L. Martínez-Sobrido, and D. H. Turner, "Antisense Oligonucleotides Targeting Influenza A Segment 8 Genomic RNA Inhibit Viral Replication," *Nucleic Acid Ther*, vol. 26, no. 5, pp. 277–285, Oct. 2016, doi: 10.1089/nat.2016.0619.
- [122] S. Sreeramulu *et al.*, "Exploring the Druggability of Conserved RNA Regulatory Elements in the SARS-CoV-2 Genome," *Angewandte Chemie International Edition*, vol. 60, no. 35, pp. 19191–19200, Aug. 2021, doi: 10.1002/anie.202103693.
- [123] M. Zafferani *et al.*, "Amilorides inhibit SARS-CoV-2 replication in vitro by targeting RNA structures," *Sci Adv*, vol. 7, no. 48, Nov. 2021, doi: 10.1126/sciadv.abl6096.
- [124] B. Gaborit, R. Govers, A. Altié, J. M. Brunel, P. Morange, and F. Peiretti, "The aminosterol Claramine inhibits β -secretase 1-mediated insulin receptor cleavage," *Journal of Biological Chemistry*, vol. 297, no. 1, p. 100818, Jul. 2021, doi: 10.1016/j.jbc.2021.100818.
- [125] Z. Qin *et al.*, "Functional properties of Claramine: A novel PTP1B inhibitor and insulin-mimetic compound," *Biochem Biophys Res Commun*, vol. 458, no. 1, pp. 21–27, Feb. 2015, doi: 10.1016/j.bbrc.2015.01.040.
- [126] Y. Yamauchi, Y. Miura, and Y. Kanaho, "Machineries regulating the activity of the small GTPase Arf6 in cancer cells are potential targets for developing innovative anti-cancer drugs," *Adv Biol Regul*, vol. 63, pp. 115–121, Jan. 2017, doi: 10.1016/j.jbior.2016.10.004.
- [127] W. Zhu *et al.*, "Small GTPase ARF6 controls VEGFR2 trafficking and signaling in diabetic retinopathy," *Journal of Clinical Investigation*, vol. 127, no. 12, pp. 4569–4582, Oct. 2017, doi: 10.1172/JCI91770.
- [128] T. Gebremariam *et al.*, "Preserving Vascular Integrity Protects Mice Against Multidrug-Resistant Gram-Negative Bacterial Infection", doi: 10.1101/2020.02.18.955518.
- [129] A. ben David *et al.*, "Identification of SARS-CoV-2 Receptor Binding Inhibitors by In Vitro Screening of Drug Libraries," *Molecules*, vol. 26, no. 11, p. 3213, May 2021, doi: 10.3390/molecules26113213.
- [130] S. Choudhary, Y. S. Malik, and S. Tomar, "Identification of SARS-CoV-2 Cell Entry Inhibitors by Drug Repurposing Using in silico Structure-Based Virtual Screening Approach," *Front Immunol*, vol. 11, Jul. 2020, doi: 10.3389/fimmu.2020.01664.
- [131] P. D. Mosier *et al.*, "Broad Spectrum Anti-Influenza Agents by Inhibiting Self-Association of Matrix Protein 1," *Sci Rep*, vol. 6, no. 1, p. 32340, Aug. 2016, doi: 10.1038/srep32340.

- [132] R. Alexey *et al.*, "Structure-based virtual screening and biological evaluation of novel inhibitors of mycobacterium Z-ring formation," *J Cell Biochem*, vol. 123, no. 5, pp. 852–862, May 2022, doi: 10.1002/jcb.30232.
- [133] B. Xiong *et al.*, "Strategies for Structural Modification of Small Molecules to Improve Blood-Brain Barrier Penetration: A Recent Perspective," *Journal of Medicinal Chemistry*, vol. 64, no. 18. American Chemical Society, pp. 13152–13173, Sep. 23, 2021. doi: 10.1021/acs.jmedchem.1c00910.
- [134] P. Chomczynski and N. Sacchi, "Single-step method of RNA isolation by acid guanidinium thiocyanate-phenol-chloroform extraction," *Anal Biochem*, vol. 162, no. 1, pp. 156–159, Apr. 1987, doi: 10.1016/0003-2697(87)90021-2.